Dissertation

submitted to the

Faculty of Biosciences

of the Ruperto Carola University Heidelberg, Germany

for the degree of

Doctor of Natural Sciences (Dr. rer. nat.)

presented by

M.Sc. Neha Thakre

born in Nagpur, India

Oral examination on: 07.06.2019

Inferring Characteristics Of Malaria Infection Of Two *Plasmodium* Strains In Mice

Referees:

Prof. Ursula Kummer

Dr. Frederik Graw

Acknowledgments

My sincere gratitude towards supervisor Dr. Frederik Graw for believing in me, his constant support and understanding of the subject. Frederik was always available for discussions, all one had to do was to knock on his office door. There were times when he had to show me the light at the end of the tunnel where I couldn't see any. I cannot thank him enough for his motivation. Special thanks to Dr. Ann-Kristin Müller for supervising the experiments and mentoring my work through all these years. Wholehearted thanks to Priyanka Fernandes for her hard work in conducting the mice experiments and providing support to this project from the biological point of view. I am also grateful to Prof. Dr. Ursula Kummer and Prof. Dr. Thomas Höfer for their interest in my work and valuable inputs.

Michael Gabel and Peter Kumberger, two excellent colleagues and friends! Thank you both for all the discussions and brain storming. Michael for making me realize it is important to take breaks and relax and Pete (aka nega-pete) for telling things as they are while supporting or criticizing my work. Sam Wilks and Paola Carrillo-Bustamante for being there and ready to discuss every topic under the sun. Paolo for her encouragement and patient ear, especially during the time of my pregnancy. Sarah Kasper, Verena Körber and Priyata Kalra for their frequent visits to the office and coffee break conversations. Thank you Annika Schneider and Sophia Eijkman for their contributions to data analysis. I want to thank all the people, who were around during my thesis, namely Arne Schoch, Martin Zauser, Jana Fehr and others. Lastly to all the people who reviewed this thesis and supported me in improving it.

Rahul, my husband, friend and guide of sorts, who always insisted in having an

Abstract

Cerebral Malaria is a complex neurological condition that results from interaction between the host and *Plasmodium* parasite through the different phases of parasite's life-cycle. This interaction ranges from infection to the immune response triggered in the host system. Various strains of the *Plasmodium* parasites are found to have differences in the severity of disease after infection. However, the precise factors defining the infectivity of Plasmodium parasites and the resulting disease outcome have not been completely identified so far. In this thesis, the *Plasmodium berghei* mouse model for Malaria is used to characterize the infection dynamics of *Plasmodium berghei* ANKA (wild-type or WT) and a mutant strain that lacks a *Plasmodium* antigen *Pb*maLS_05. It was found that the mutant infection leads to lower parasitemia in red blood cells and less severe disease outcome in contrast to mice infected with the wild-type strain. Moreover, the mice infected by injecting *Pb*maLS_05(-) KO-infected red blood cells show reduced immune response in contrast to infection with *Pb*maLS_05(-) knockout (KO) -sporozoites. By developing mathematical models describing various mechanisms of the infection and fitting them to experimental data; I find factors that influence the difference in disease progression seen between the two strains. Most strikingly, the KO strain show a decreased ability to infect immature red blood cells that are usually a preferred target of the parasite. This altered property of infection limits parasite burden and affects disease progression. In addition to this, I performed a statistical analysis of immune activation and immune response data from the KO or WT infected mice, which resulted in selecting major indicators of cerebral Malaria. The analysis showed that the number of $CD8^+$ T cells accumulated in the

brain, the reduced proportion of CD8$^+$ T cells to lymphocytes in the spleen, the increased presence of Malaria specific CD8$^+$ IFN-γ^+ T cells and the secondary activation of CD8$^+$ T cells due to the antigens cross-presented by infected red blood cells sequestered in the brain are the prominent distinguishing factors between the ECM causing *Pb*ANKA and non-ECM causing *PbmaLS_05*(-) infections. An exploratory analysis of the liver-stage of infection and immune response highlighted that *Pb*maLS_05 may not have an important role to play in the triggered immune response during the liver-stage of Malaria. However, its absence may lead to a small decrease in number of productive infections during the liver-stage, which must be further investigated. The antigen *Pb*maLS_05 can potentially aid in discovering the factors that influence the activation of immune responses and that might contribute to vaccine development and efficient parasite control.

Zusammenfassung

Zerebrale Malaria ist eine komplexe neurologische Erkrankung, die durch die Interaktion zwischen dem Wirt und den verschiedenen Phasen im Lebenszyklus des *Plasmodium* Parasiten ausgelöst wird. Diese Interaktion umfasst alles, von der Infektion bis hin zur ausgelösten Immunantwort des Wirtssystems. Es wurde festgestellt, dass verschiedene *Plasmodium* stämme sich in der Schwere der Krankheit unterscheiden. Allerdings sind die genauen Faktoren, die die Infektivität des Plasmodiumparasiten und den Krankheitsverlauf bestimmen, bis jetzt noch nicht komplett identifiziert. In dieser Arbeit wird ein *Plasmodium berghei* Mausmodell benutzt, um die Infektivität von *Plasmodium berghei* ANKA (Wildtyp) und eines mutierten Stammes, welchem ein *Plasmodium* antigen *Pb*malS_05 fehlt, zu charakterisieren. Die Mutanteninfektion führt zu einer niedrigeren Parasitemie in den roten Blutkörperchen und zu einem weniger schweren Krankheitsverlauf im Vergleich zu Mäusen, die mit dem Wildtypstamm infiziert wurden. Außerdem zeigen die Mäuse, denen *Pb*maLS_05(-) KO-infizierte rote Blutkörperchen injiziert wurden, eine reduzierte Immunantwort im Vergleich zu einer Infektion mit *Pb*maLS_05(-) KO-Sporozoiten. Durch das Entwickeln mathematischer Modelle, die verschiedene Mechanismen der Infektion beschreiben, und das Fitten an experimentelle Daten, finde ich Faktoren, die den Unterschied im Krankheitsverlauf der beiden Stämme, beeinflussen. Am auffälligsten ist, dass der KO Stamm eine verminderte Fähigkeit aufweist, rote Blutkörperchen zu infizieren, welche normalerweise das bevorzugte Ziel des Parasiten sind. Diese veränderte Eigenschaft der Infektion limitiert die Parasitenlast und beeinflusst den Krankheitsverlauf. Des Weiteren wurde eine statistische Analyse der Immunaktivierung und Immunant-

wort von KO oder WT infizierten Mäusen durchgeführt, die es möglich machte, Hauptindikatoren für zerebrale Malaria auszuwählen. Die Analyse zeigte, dass die Anzahl der im Gehirn akkumulierten CD8$^+$ T Zellen, der reduzierte Anteil von CD8$^+$ T Zellen im Vergleich zu Lymphozyten in der Milz, die gesteigerte Präsenz der malariaspezifischen CD8$^+$ IFN-γ^+ T Zellen und die sekundäre Aktivierung von CD8$^+$ T Zellen durch Antigenpräsentation von infizierten roten Blutkörperchen, die sich im Gehirn ansammeln, wichtige Unterscheidungsfaktoren zwischen ECM-verursachenden *Pb*ANKA und nicht-ECM-verursachenden *Pb*maLS_05(-) Infektionen sind. Eine explorative Analyse des Leberstadiums der Infektion und Immunantwort zeigte, dass *Pb*maLS_05 möglicherweise keine wichtige Rolle in der ausgelösten Immunantwort während des Malaria Leberstadiums spielt. Allerdings könnte die Abwesenheit zu einem kleinen Abfall der Anzahl von produktiven Infektionen während des Leberstadiums führen; dies muss noch weiter erforscht werden. Das *Pb*maLS_05-Antigen kann potenziell helfen, die Faktoren, die die Aktivierung der Immunantwort beeinflussen und die zu Vakzinentwicklung und effizienter Parasitenkontrolle führen, zu identifzieren.

Contents

List of Figures

List of Tables

CHAPTER 1

General Introduction

Malaria is among the most serious tropical diseases affecting millions of lives across the globe. A total of 93 countries in the African, Asian and Americas regions are currently Malaria-endemic [1]. The incidence of Malaria is most frequent among the poor who live in rural areas with little or no facilities for barriers against Malaria. Therefore, Malaria is also called the epidemic of the poor. In 2016 alone, Malaria was responsible for 216 million clinical cases and an estimated number of 445,000 deaths worldwide [1]. These huge numbers may well be an underestimate owing to missing facilities for adequate reporting in the endemic regions. Malaria is a mosquito-borne disease and is caused by the protozoan parasite *Plasmodium*. It is characterized by acute anemia which in severe cases results in respiratory disorders or permanent brain damage. Too late interventions may also cause death. Cerebral Malaria, a leading cause for mortality in Malaria, is characterized by coma and long-term neuro cognitive impairments in the surviving patients [2]. It is caused by *Plasmodium falciparum*, the most prevalent and lethal Malaria parasite affecting humans.

There have been several efforts towards Malaria control since the last century. To name a few, the emergence of special insecticides in the 1930s and the discovery of the first anti-Malarial drug Chloroquine in the 1940s. More recent work has been in advancement of insecticide-treated bed nets, reduction of mosquito populations by biological control and creations of vaccines. Of the vaccines currently under consideration, the RTS,S is the most developed but suffers from poor efficacy [3]. Other vaccines that are still in the early phases of development include the genetically attenuated parasite (GAP) malaria vaccine [4] and the transmission

blocking vaccines (TBV) targeting the transmission of parasites from mosquito to humans [5]. In-spite of remarkable progress in fighting Malaria, the emergence of multi-drug resistant strains in recent years has marred the various programs towards Malaria eradication [6]. Therefore, more efforts in the formulation of treatment strategies that instead of targeting the parasite, aim at weakening underlying disease mechanisms are required for effective Malaria control. For designing such strategies, a complete understanding of Malaria pathogenesis is desirable, many aspects of which are still unknown. For example, it has been observed across various *Plasmodium* strains that some strains cause only less severe symptoms and are treatable, whereas others trigger serious health impacts [7]. Identifying the factors that shape the extent of harm caused by a strain can be potentially explored to develop newer drugs and searching vaccine targets [7]. Such factors that eventually decide the fate of disease can be related to any stage of the parasite cycle. In the following sections, the life-cycle of *Plasmodium* is described. This is followed by the discussion on observed varying levels of severity of disease caused by different *Plasmodium* strains. Next, the experimental observations that motivated this thesis are introduced. Towards the end, the implications of these observations and why they lead to the investigation of various stages of the disease are elaborated.

1.1 Life-cycle of the Malaria parasite

Plasmodium lives inside multiple hosts along-with different within-host stages during its lifetime. Its complex life cycle can be broken down into two events: the parasite takes a motile form to go from one location to the other (from one host to the other or one organ to the other inside a host), and once inside the desired location, transforms into a replicative, growing form. This sub-cycle repeats three times over the life cycle the malaria parasite [8]. When an infected mosquito bites a vertebrate host, parasites in the form of sporozoites are released from the mosquito's salivary gland into the host, after which the sporozoites travel to the liver. Inside the liver, the parasite replicates by infecting hepatocytes, that burst to release tens of thousands of merozoites marking the end of the liver stage. These merozoites are released into the bloodstream where they infect red blood cells (RBCs). Inside an iRBC, the parasite undergoes asexual reproduction to release
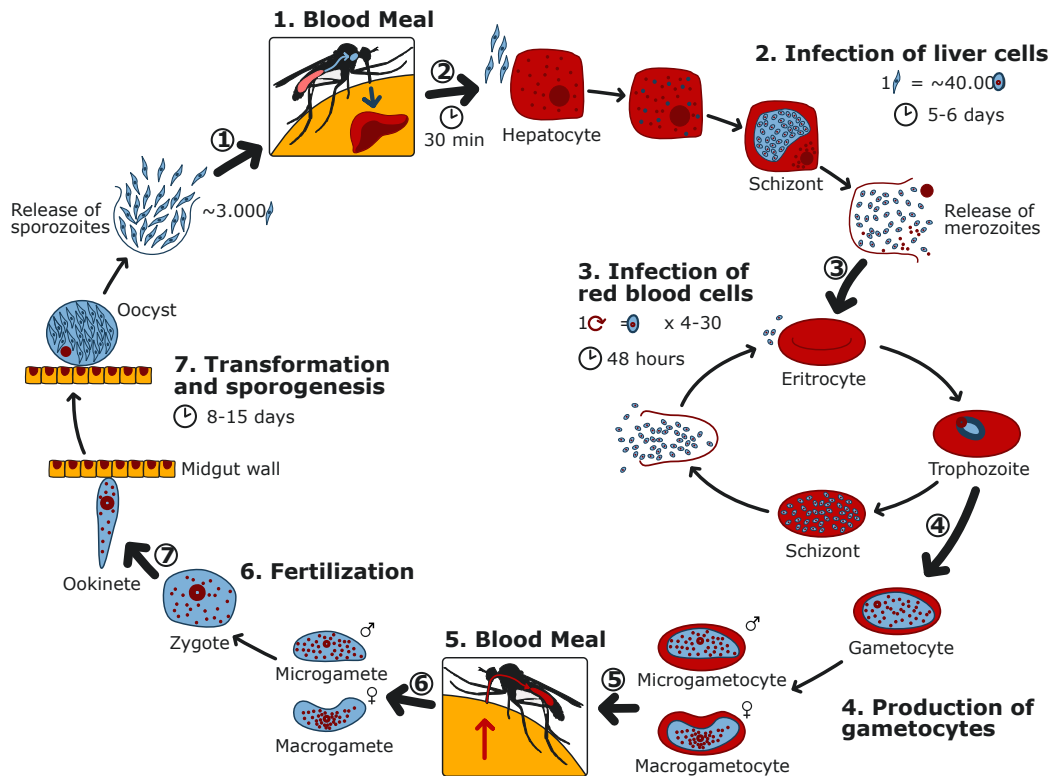
FIGURE 1.1 The life cycle of *Plasmodium*

Mosquitoes transmit sporozoites to the host. These sporozoites infect liver cells, where they mature to form schizonts. The infected liver cells burst to release merozoites that infect the red blood cells. In the blood, the parasite reproduces asexually to produce more merozoites that further infect other red blood cells. Some of the merozoites develop to form male or female gametocytes that are taken up by mosquito during a blood meal. The gametocytes reproduce sexually inside the mosquito to produce sporozoites. This figure has been reproduced and modified with permission from Bbkkk [CC BY-SA 4.0 (https://creativecommons.org/licenses/by-sa/4.0)]

more merozoites that infect other uninfected RBCs finally causing anemia in the host. A proportion of the blood-stage parasites differentiate into male and female gametocytes. These gametocytes reach the mosquito that takes a blood meal on the infected host. The gametocytes develop into gametes that fuse in the mosquito's gut to produce a zygote, that in turn develops into oocyst, inside which thousands of sporozoites are produced that migrate to the salivary glands, thereby continuing the cycle again [9].

1.2 Malaria parasites show heterogeneity in disease outcomes

It has been found that the *Plasmodium* parasite strains exhibit a broad variation in the extent to which they harm their hosts and the way in which they do it. *Plasmodium vivax* is known to cause Malaria in humans that is relatively benign and rarely results in life threatening consequences. Whereas, *Plasmodium falciparum* infections in humans are often of the severe kind, for example, cerebral Malaria or pregnancy related Malaria in which both the mother and fetus are in danger. Mouse models are often used to mimic Malaria infection in humans, in order to answer questions that cannot be answered by observing an infected human [10]. Most common mouse models include infection by a parasite called *Plasmodium berghei*. Of these, *P. berghei*ANKA causes experimental cerebral Malaria or ECM and leads to death in mice, whereas *P. berghei*NK65 causes liver injury and is also lethal [11]. Investigating such contrasting infections has proven useful in outlining various factors that contribute to severity of disease [12–14].

1.3 Deletion of a specific gene abrogates the development of experimental cerebral Malaria in mice

PbmaLS_05 is a *Plasmodium* gene that has been conserved through evolution. It is present in all of the human and rodent *Plasmodium* strains. This gene localizes

to the apicoplast, an organelle that is an endosymbiotic relict of the parasite. The researchers at the Centre for Infectious Diseases, Parasitology Unit, University Hospital Heidelberg deleted this gene and investigated the *PbmaLS_05* (-) (KO) strain in comparison with the *Pb*ANKA (WT) strain [13]. It was observed that deleting the *PbmaLS_05* had hardly any impact on the life-cycle, but it altered the expected severe disease outcome. The mice infected with the developed KO did not develop ECM. These results were unchanged when the mice were infected through two different modes of infection, namely via sporozoites or infected red blood cell (iRBC). The precise reasons for the altered pathogenic outcome of *PbmaLS_05* (-) KO parasites could not be deduced from the experimental data alone. It requires testing of various biologically plausible hypotheses that can explain the observations. The complex parasite life-cycle tells us that there are many possible events in the progression of the infection where this growth defect may result in less severe disease outcomes. In the following sections, such hypotheses are discussed.

1.4 Varying *Plasmodium* strains posses a wide range of infectivity during the blood-stage

The blood-stage of the *Plasmodium* parasite is responsible for the clinical manifestations of Malaria. Thus, most of the variations in disease outcomes among various strains arise from differences in blood-stage infection characteristics [12, 15–19]. In humans, *Plasmodium vivax* restricts invasion only to young red blood cells [20]. *Plasmodium berghei* in mice prefers to infect young RBCs, whereas for others it is equally likely to infect cells of different age groups. In addition to RBC age, the parasite strains may also differ in other blood-stage infection properties including rate of infection, the time taken for an infected RBC to mature or production rate of merozoites from a mature infected RBC. All of these above characteristics must be shaped by the benefit that the parasite gains from them. For example, it has been proposed that restricted infection of younger RBCs is advantageous to the parasite to self-regulate and not cause excessive harm to the host, thereby increasing its chances of transmission [21]. However, this also

means, that against such infections, temporary reduction of RBC production may help the host to recover [14, 22]. On the other hand, an increased preference for young red blood cells or reticulocytes has been related to highest parasite densities, producing severe anemia [22]. Thus, restriction or preference of particular RBC age appears to be a strong contributor to decide fate of the disease. This leads to the hypothesis that *PbmaLS_05* (−) KO parasites fail to cause ECM because of altered infection characteristics, particularly in relation to RBC age during the blood-stage. Comprehending which of the infection characteristics are altered and quantifying their impact on resulting infection is a major part of this thesis.

1.5 Liver-stage development is strongly linked to nutrient availability

Availability of a conducive environment and adaptability of *Plasmodium* to it are the key factors governing overall fitness of the parasite during the life-cycle through multiple hosts and multiple organs within the host [8]. Once the motile form of the parasite, the sporozoite, reaches the host liver and enters a hepatocyte, it changes into a reproductive form called the liver-schizont, that undergoes multiple divisions. This division rate is one of the fastest growth rates among eukaryotic cells [8]. During such extreme activity, in spite of having its own metabolism, the parasite additionally scavenges a variety of nutrients and metabolites from the host cell [23, 24]. In fact, genetically obese (fa/fa) Zucker rats were observed to have four fold higher number of parasitized hepatocytes than the lean Fa/fa control rats [25]. *In vivo* murine experiments that studied the effect of host-starvation on *Plasmodium* liver-stage development found that the starved mice showed more than 10-fold increase in parasite load on infection than the normal-fed and infected mice. The parasites in the starved case, showed both an increased size and increased survival rate [26]. Under starvation, a proportion of cells undergo canonical autophagy, that is nothing but self-digestion of parts of the cytoplasm, thereby releasing amino acids and sugars into the environment. Prado *et al.* hypothesize that as a result of the triggered canonical autophagy in the livers of starved hosts, the intra-hepatic parasite experience a nutrient abundant envi-

ronment, thus increasing in size and surviving better due to reduced competition for nutrients [26]. In another study, mice deficient in a key autophagy promoting protein, ATG5, were found to produce significantly smaller parasites when infected with *Plasmodium yoelli* 17X, hypothesizing that growing parasites utilize the autophagic pathway as a source of nutrients [27]. This strongly supports the correlation between parasite development in the intra-hepatic stage and nutrient availability.

In the *PbmaLS_05* gene experiment, number and size of the parasite in its liver-stage form were quantified *in vitro* [13]. The data suggests that absence of *PbmaLS_05* has no effect on the number or developmental size of intra-hepatic parasites, *in vitro*. However, a slight developmental delay was observed for KO parasites during the early time points of hepatic infection. It is probable, that this difference observed *in vitro* is pessimistic, and the KO parasite growth is additionally retarded *in vivo*. The apicoplast is known to play an important role in fatty acid synthesis as well as scavenging from degraded host cell material [28,29]. The fact that *PbmaLS_05* localizes to the apicoplast [13] makes it highly probable that *PbmaLS_05* contributes in parasite nutrition synthesis. Thus, a possible reason for the observed developmental delay could be that *PbmaLS_05* gene plays a role in secondary nutrition pathways, the scavenging of nutrients as well as metabolites from the host cell cytoplasm. As this is not explicitly required for the development of the parasite, the KO parasite successfully completes the life-cycle, but remains smaller sized and lesser in number than the WT parasite.

1.6 Cerebral Malaria and its yet unknown pathogenesis

Of the total Malaria cases that culminated in death in the year 2016 [1], $\sim 13\%$ were due to cerebral Malaria (CM) [30]. Cerebral Malaria, caused by *Plasmodium falciparum* in humans, is the most severe outcome of Malaria. It is a neurological complication, characterized by coma with high mortality rate, and long-term neuro-cognitive impairments in the surviving patients [2]. Available treatment on cerebral Malaria still suffers from low efficacy [31] and drug resistance [32].
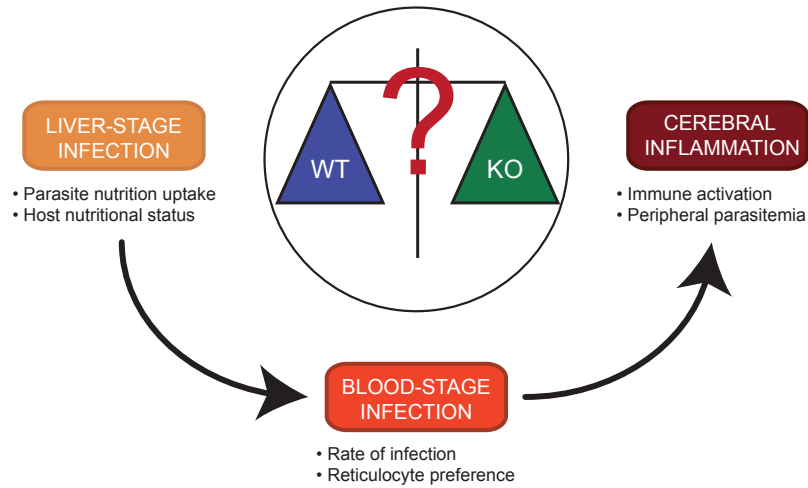
FIGURE 1.2 Overview of the thesis

Different stages of Malaria and the specific characteristics that are the focus of the thesis. These characteristics are used to compare the two murine strains *Pb*ANKA WT and *PbmaLS_05*(-) KO during the various within-host stages of Malaria.

New treatment strategies can be developed by understanding the not yet precisely known pathogenesis of cerebral Malaria. So far it has been established that imbalance of pro- and anti-inflammatory immune response to Malarial infection is the primary cause of cerebral pathology, however, the exact processes in the infection dynamics that cause this imbalance and their complex interactions are largely unknown [33]. *Plasmodium berghei* ANKA infection in C57BL/6 mice is a mouse model often used for experimental cerebral Malaria (ECM) [34]. The observations from the *PbmaLS_05* (-) (KO) parasite show that although the KO-infected mice do not develop ECM, there is a difference in the immune activation and migration of immune cells to the brain between the KO-iRBC-infected mice and KO-sporozoite-infected mice. Whereas, the *Pb*ANKA WT-infected mice consistently showed similar levels of immune activation and migration irrespective of the route of infection. The experimentally measured number of various immune cell types and their proportions in spleens and brains from these differently infected groups of mice can be effectively used to understand, which of these cell-types play a key-role in the development of ECM.

1.7 Mathematical models for within-host Malaria infection dynamics

It is essential to establish factors that are involved in a disease, however, this alone is not enough. Quantification of the extent of a factor shaping the outcome of a disease is important as well [35]. This belief drove Ronald Ross to develop a mathematical model, known as the 'Ross model'. This was an epidemiological model that demonstrated the relationship between the number of mosquitoes and the incidence of Malaria in humans [36]. For many years, model-based testing of mechanistic hypotheses, has been used to study infectious diseases. In Malaria too, several mathematical models exist that model the within-host parasite and its interaction with the host. These models are instrumental in explaining the experimental observations by assuming a plausible hypothesis, for example, preferred specific targets by particular parasite strains [7, 12, 19], effect of treatment [37, 38], elicited immune response [39, 40]. As parasitemia in Malaria is associated with its blood-stage within the host, the blood-stage remains the most modeled stage in the field. These models are designed to track the parasite replication in red blood cells, the red blood cell turnover and the resulting parasitemia. Depending on the kind of theoretical hypothesis being tested against experimental observations, these models may range from the more basic, as a system of ODE equations of standard viral replication [41] to more recent, powerful and complex partial differential equations in applications where the effect of red blood cell age on infection dynamics is being explored [12, 19, 22, 42]. Some models are further extended to include response to drug [43] or immune responses triggered during the blood-stage [44]. On the other hand, the number of mathematical models for the liver-stage is very limited. Other than some models, that consider the interaction between transmission and liver-stage [45] or liver-stage and blood-stage [46, 47], this area is highly unexplored, possibly due to the limitations in gathering data during the liver-stage [48]. No model that incorporates the role of available nutrients and host-autophagy on intra-hepatic development of *Plasmodium* was found. As the information on pathogenesis of cerebral Malaria is still limited, the use of mathematical models or advanced statistical methods to acquire a theoretical un-

derstanding of this immune response related severe disease outcome is missing. There are some studies that quantify the sequestered RBC population during the blood-stage of Malaria that can be considered pre-cursors to the onset of cerebral Malaria [49], but more recent studies that tackle this problem with a mathematical model are unavailable. Machine learning is another effective tool for statistical inference in problems where instead of modelling a hypothesis, the computer is made to infer a relationship between variables in a dataset [50]. In Malaria, the use of machine learning is restricted to mostly image analysis in Malaria diagnosis [51–53] and rarely to other applications, for example, discovering drug combination therapies using large clinical datasets [54]. But this technique hasn't been explored to decipher Malaria pathogenesis, mainly due to the lack of large datasets from lab experiments.

1.8 Outline of the thesis

My thesis aims at modeling the infection dynamics of two *Plasmodium* strains on the basis of experimental data at various stages of the disease. The first strain is the wild-type *Plasmodium berghei* ANKA, which when used to infect C57BL/6 is a mouse model for experimental cerebral Malaria. The other is the knock-out *PbmaLS_05(-)* that was observed to not cause cerebral symptoms in mice [13]. The available data itself, are not sufficient to determine which factor exactly shapes the disease outcome and to what extent. This limitation is overcome by using mathematical modeling to test various plausible hypotheses. By understanding the differences in the disease dynamics between the two strains using various models, further conclusions can be drawn towards the pathogenesis of Malaria. With this goal, the thesis is structured into the following chapters.

In Chapter 2, the experiments and the observed data are described in detail. The common technical methods related to modeling throughout the chapters are explained.

Chapter 3 describes the blood-stage infection dynamics model that is based on the red blood cell turnover model [55] and infection model from [12]. In this chapter, I discuss how the combined model is insufficient in describing the intended data, and modifications to RBC turnover due to the onset of Malaria are required

11

to fully explain the observations. In addition, distinct infection parameters for the two strains are estimated and compared to reveal which of the two strains has a higher preference for young red blood cells or reticulocytes.

The scope of Chapter 4 is similar to Chapter 3, however the data to be modeled here is from the mice that were treated with phenylhydrazine and then infected with the respective strains. Phenylhydrazine is a drug used to induce artificial anemia in lab animals. Therefore, in this Chapter, the changes to the erythropoietic system because of the treatment is modeled. With this treatment model, and the infection parameters from Chapter 3, the resulting infection dynamics in treated animals is predicted and discussed.

Chapter 5 is a proof of concept study that investigates the potential role of nutrition availability during the liver-stage parasite development via a liver-stage mathematical model for parasite dynamics in the liver-stage. For such an investigation, an extreme example of parasite development under nutrition abundant conditions was needed, therefore the experimental data from [26] were used to design the model. This Chapter highlights the correlation between parasite replication and environmental nutritional status and the fact that minor differences in the number of parasites seen between the WT and KO during the liver-stage could potentially lead to major differences in the parasites that egress to blood-stage.

Chapter 6 focuses on a novel application of a simple machine learning algorithm to highlight the distinct levels of immune activation and immune sequestration in mice infected by one of the two strains. The model is based on the observed immune response activated in the spleen and sequestered immune cells in the brain on day 6 post initiation of the blood-stage. This Chapter sheds light on the underlying immune mechanisms and motivates protocols for future experiments.

Chapter 7 summarizes the findings of the thesis and puts everything into context of the fundamental question, what potentially changed in the KO infection dynamics, that it failed to cause cerebral Malaria in mice (see Fig. 1.2 for an overview).

Some sentences of the introductory paragraph of this chapter are reproduced from [56], which were written together with Dr. Frederik Graw, Dr. Ann-Kristin Müller, Priyanka Fernandes and me.

CHAPTER 2

Materials and Methods

2.1 Introduction

In this chapter, I describe the experimental protocols, the observed data and techniques used for model fitting and parameter estimation. As the thesis involves modeling disease dynamics during various within -host stages of Malaria, the chapter has been sectioned on the basis of stages of Malaria, I present the materials and methods in the following order:

1) Blood-stage infection
2) Liver-stage infection
3) Cerebral inflammation

2.2 Experimental data

2.2.1 Blood-stage infection

2.2.1.1 Experiment on untreated mice

In this experiment, two groups of C57BL/6 inbred mice were infected with 10^6 infected red blood cells (iRBCs) intravenously on day 0 (start of the experiment). The iRBCs used were obtained from mice infected with wild-type PbGFP Luc$_{con}$ ($P.berghei$ line 676m1c11) (WT), a GFP-luciferase transgenic derivative of

---

The material in this chapter was presented in part in [56].
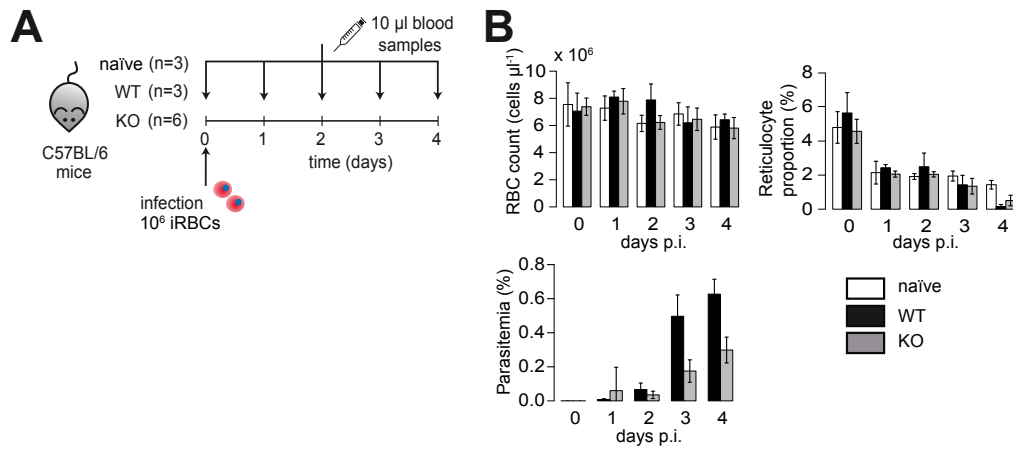
FIGURE 2.1 Experiment on untreated mice

(A). C57BL/6 mice were infected with 10^6 iRBC of *Pb*ANKA (WT), *PbmaLS_05* (-) (KO) or left uninfected. Samples of 10 μl blood were drawn daily to measure the concentration of RBC (cells/μl), reticulocyte proportion (in % of RBC) and parasitemia (in % of RBC). **(B)**. Measured concentration of RBC (cells/μl), reticulocyte proportion (in % of RBC) and parasitemia (in % of RBC) for each of the three groups.

P. berghei ANKA [57], or the mutant *PbmaLS_05* (-) parasites (KO) generated in the wild-type *Pb*GFP Luc$_{con}$ strain [13]. A group of naïve control mice consisted of uninfected mice that were of similar age ranges as the two infected groups. 10 μl of blood samples were taken daily from all the mice from day 0 until day 4 post infection (p. i.). The total red blood cell count, reticulocyte proportion in every 100 red blood cells and parasitemia defined as proportion infected red blood cells in every 100 red blood cells were measured from the daily blood samples. The RBC count was measured using a Coulter counter and reticulocyte proportion were measured via FACS analysis of CD71 CD71-PE, eBioscience, Clone R17217) labeled reticulocytes. FACS analysis was used to determine GFP positive infected red blood cells to quantify parasitemia. A sketch of the experimental protocol is shown in Fig. 2.1 Mice were sacrificed at day 5 p.i., when mice infected with WT parasites showed first symptoms of severe experimental cerebral Malaria.
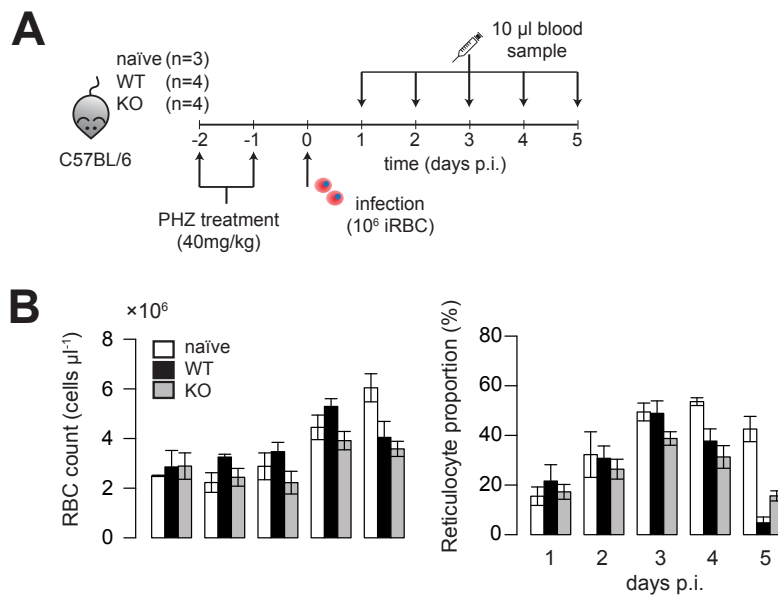
FIGURE 2.2 Experiment on Phenylhydrazine (PHZ) treated mice
(A). Mice were pre-treated with one dose of 40 mg/kg PHZ on each of two days before infection. The mice were then infected with with 10^6 iRBC of WT or KO parasites on the following day. One group (n=3) was left uninfected. 10 μl blood samples were taken daily and analyzed. **(B)**. Measured concentration of RBC (cells/μl) and reticulocyte proportion (% of RBC) for each of the three groups.

2.2.1.2 Experiment on Phenylhydrazine (PHZ) treated mice

As an extension to the experiment described in Subsection 2.2.1.1, three groups of mice were treated with two doses of phenylhydrazine (PHZ, 40 mg/kg), on two consecutive days. Two of these three groups were infected with 10^6 iRBC obtained in the same way as described in Subsection 2.2.1.1, whereas the third group were kept uninfected as PHZ treated control. 10 μl samples of blood taken from each mouse, everyday, from day of infection to day 5 p.i. were analysed for total RBC count, reticulocyte proportion and parasitemia using methods explained in Subsection 2.2.1.1. A sketch of the experimental protocol is shown in Fig. 2.2. The mice were sacrificed on day 6 p.i..

2.2.2 Assessment of the effect of nutrition availability on parasite liver-stage development
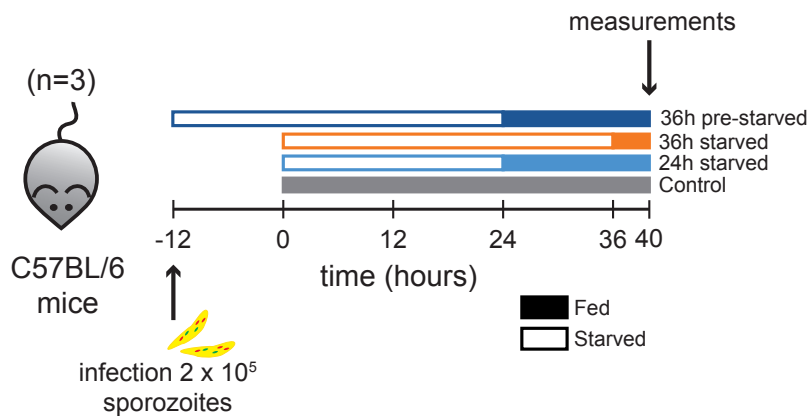
FIGURE 2.3 Experimental protocol for the liver stage
C57BL/6 mice in four groups of 3 mice each were infected with 2×10^5 sporozoites. Each of the groups of mice were starved for 24h or 36h or 12h prior to infection and 24h post infection or were fed normally (control) [26]. The size and number of parasites in the liver were measured by removing the livers at 40h post infection and analyzing their histology.

The data used for this part of the thesis is completely based on the experiments done by Prado et al [26]. In this experiment, C57BL/6 mice were infected with 2×10^5 sporozoites of PbmCherry$_{hsp70}$+Luc$_{eef1\alpha}$ *P. berghei*-ANKA. The mice were divided into 3 groups with different starvation regimes: a control group feeding ad libidum, fasted for 24 h or 36 h or 12 h prior to infection and 24 h post infection via sporozoites (termed as 36h pre-starved). At 40 hpi livers of all the mice were removed and their histology analyzed by staining sections of the liver with hematoxylin and eosin (H&E) to measure parasite numbers and parasite size using bioluminescence imaging. In detail explanation of the methods can be found in [26]. The experimental protocol is represented in Fig. 2.3.

2.2.3 Cerebral inflammation

Two groups of 5 C57BL/6 mice each were infected with *P.berghei* ANKA WT or *PbmaLS_05* (-) strains via sporozoite injections. Another group of 5 mice was
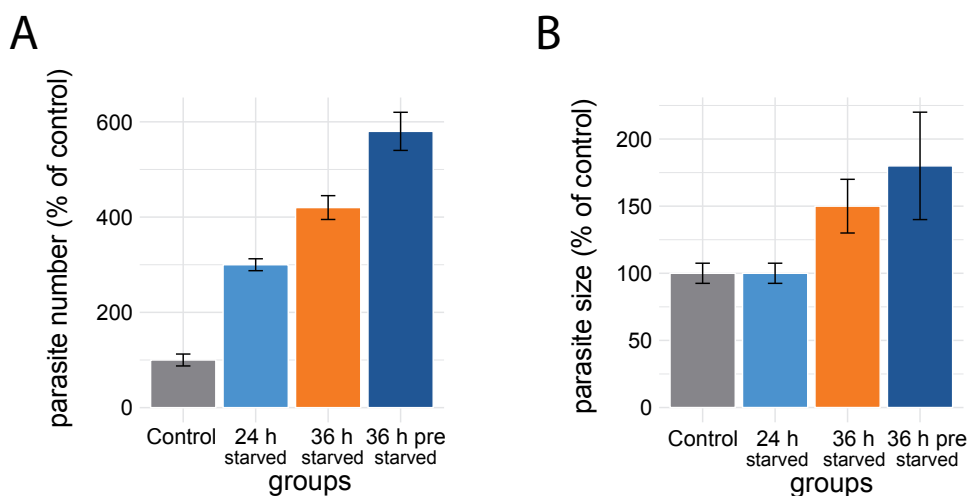
FIGURE 2.4 Experimental data for the liver stage
C57BL/6 mice in four groups of 3 mice each were infected with 2×10^5 sporozoites. Each of the groups of mice were starved for 24h or 36h or 12h prior to infection and 24h post infection or were fed normally (control). The number **(A)**. and size **(B)**. of parasites in the liver were measured by removing the livers at 40h post infection and analyzing their histology. Experiments were repeated 3 to 5 times (error bars show SD) [26].

kept uninfected as a control group. All the mice were sacrificed on day 8 p.i.. The brains and spleens of these mice were harvested and the lymphocytes were isolated. A part of the lymphocytes were also stimulated *ex vivo* with parasite-derived Pb1 of GAP50 (SQLLNAKYL) epitope [58]. All the cells were stained for CD8$^+$, CD4$^+$ and IFN-γ. Quantification and phenotypic analysis of T cells was done by flow cytometry.

In a separate set of experiments, two groups of 5 C57BL/6 mice each were infected with *P.berghei* ANKA WT or *PbmaLS_05* (-) strains via infected red blood cells (obtained as stated in Subsection 2.2.1.1) injections, and a group of 5 mice was kept uninfected as a control group. All the mice were sacrificed on day 5 p.i.. The spleens and brains of these mice were harvested and CD8$^+$, CD4$^+$ and IFN-γ numbers and proportions were recorded as in the experiment with sporozoite infection mentioned earlier in this Subsection. For more details on the methods used refer [13].

2.3 Mathematical Models and Parameter Fitting

The implementation of mathematical models and there analyses was done in the R language of statistical computing [59]. The age-structured model of RBC aging and anemia dynamics was compartmentalized to form a tractable system of ordinary differential equations with gamma-distributed lifetimes for RBC and maturation times for infected RBC [12]. A compartment length of 4h was used in these models. The deSolve R package was used to solve differential equations [60]. The models were fitted to the data using 'optim' fitting function in R. In places where the fitting algorithms failed to converge due to a strong correlation between the parameters, a parameter sweep was performed to find sets of parameters that fit the data. All proportion data (parasitemia levels and proportion of reticulocytes) were logit- transformed to allow residuals that are normally distributed residuals. Data from the infected groups were scaled relative to the control data. The residual sum of squares scaled by the number of data points, also known as the average Residual Sum of Squares (aRSS) was calculated to evaluate model performances. The 95%-confidence intervals were assessed by profile likelihood analysis.

2.4 Classification with logistic regression

In Chapter 6 I will use logistic regression to determine the most significant variables in deciding a categorical outcome. Here the theory of logistic regression is explained.

Consider a set of n observations $\mathbb{D}$ such that $\mathbb{D} = \{d_1, d_2, \ldots, d_n\}$. Each d_i consists of two parts $d_i = \{x_i, y_i\}$. x_i is a vector of m covariates or features and y_i is a categorical outcome vector with Y possible outcomes that are dependant on x_i. When the classification is for binary class levels, Y can take the value 0 (negative class) or 1 (positive class). A future x with unknown corresponding y is classified as 0 or 1 by a prediction rule built by learning $\mathbb{D}$. Here, the prediction rule is modelled using logistic regression.

$$p(y = 1|x_i) = \frac{e^{\beta_0 + \sum_{j=1}^{m} \beta_j x_{ij}}}{1 + e^{\beta_0 + \sum_{j=1}^{m} \beta_j x_{ij}}} \tag{2.1}$$

$$= \frac{e^z}{1 + e^z}; \text{ where } z = \beta_0 + \sum_{j=1}^{m} \beta_j x_{ij} \tag{2.2}$$

The logistic regression model takes the form of Eq. 2.2 [61], where $x_i = (x_{i1}, x_{i2}, \ldots, x_{im})$ is the feature matrix, with a feature size of m and $\beta_0, \beta_1, \ldots, \beta_m$ are the $(1 + m)$ weight coefficients for the intercept and the m features. The probability $p(y = 1|x_i)$ represents the probability that the ith sample is from class 1. The default decision threshold is at 0.5.

$$\hat{y}_i = \begin{cases} 1; & \text{for } p(y = 1|x_i) \geq 0.5 \\ 0; & \text{for } p(y = 1|x_i) < 0.5 \end{cases} \tag{2.3}$$

One concern in fitting such models to data is selecting a subset of predictors that are just enough to explain the dependant variable. Also, in datasets with many correlated variables, the weights are poorly determined and the model exhibits high variance. A very large positive coefficient or weight on one variable can be cancelled by an equally large negative coefficient on the other correlated variable. In such cases, Lasso regularization (see Eq. 2.4) can be used that constrains the size of coefficients during the fit and ensures that over-fitting is avoided thereby making the resulting model easy to interpret. In Eq. 2.4, λ is the regularization term, a hyper-parameter of the logistic regression fit.

$$\hat{\beta}^{lasso} = \arg\min_{\beta} \left\{ \frac{1}{2} \sum_{i=1}^{N} (y_i - \beta_0 - \sum_{j=1}^{m} x_{ij}\beta_j)^2 + \lambda \sum_{j=1}^{m} |\beta_j| \right\} \tag{2.4}$$

2.5 Classifier Performance Metrics

The performance of this logistic regression based classifier is quantified using a 2 x 2 confusion matrix as shown in Table 2.1 [62].

The numbers along the major diagonal represent the number of observations correctly classified (given a threshold τ), and the numbers off this diagonal represent the errors. True positive (TP) is the number of positive observations classified as positives, whereas true negative (TN) is the number of negative observations classified as negatives. Additionally, false positive (FP) is the number of obser-

TABLE 2.1 A 2 x 2 confusion matrix for a given threshold τ

Predicted

		1	0
	1	TP	FN
Actual	0	FP	TN

vations that are incorrectly classified as positive and false negative (FN) is the number of observations that are incorrectly classified as negative. Accuracy of the classifier for a total of N number of observations defined as:

$$ACC = \frac{TP + TN}{N} \tag{2.5}$$

Other performance indicators are sensitivity (SEN) that measures the proportion of positives that are correctly classified while specificity ($SPEC$) measures the proportion of negatives that are correctly identified. As the decision threshold τ increases, the sensitivity increases and the specificity decreases.

$$SEN = \frac{TP}{TP + FP} \tag{2.6}$$

$$SPEC = \frac{TN}{TN + FN} \tag{2.7}$$

2.6 Receiver operating characteristic (ROC) curve

The ROC curve is a two-dimensional curve in which true positive rate or sensitivity is plotted against false positive rate or 1-sensitivity. Such a graph represents the tradeoffs between benefits (true positive) and costs (false positive). The ROC curve is therefore a tool to set classifier thresholds depending upon the goal of setting up the classifier in the first place. Some applications may demand a higher sensitivity with negotiable specificity whereas some may aim for a higher specificity with negotiable sensitivity. The area under the ROC curve (AUC) ranges between 0 and 1 and a higher AUC denotes a better performing classifier [62,63].

CHAPTER 3

Blood-stage infection dynamics in mice

3.1 Introduction

Within the host, *Plasmodium* parasites follow a complex life cycle involving parasite replication and differentiation in liver and blood [64]. Pathogenesis of malarial disease is mainly associated with the blood-stage of the parasite life-cycle [65] as parasite infection and lysis of infected RBCs causes anemia, the main symptom characterizing a malarial infection [66]. It has been suggested in many studies that different parasite strains show varying RBC age-specific target preference [12, 15, 16, 19, 22]. Infact, the preference for anemia -induced, newly produced reticulocytes demonstrated by some parasite strains has been implicated in elevated parasite density and severe disease outcomes [67]. In this chapter, I use a combination of experimental data and mathematical models to investigate parasite blood-stage infection dynamics. The model accounts for rate of erythropoiesis and its dependence on the changing peripheral RBC concentration, the reduction in erythropoiesis following a malarial infection and the replication and multiplication of the parasite in the RBC pool. Using this approach, I determine if specific target preference during the blood-stage could be a possible factor in contributing to different disease outcomes between the *Pb*ANKA (WT) and *PbmaLS_05* (-)

Some sentences and most of the figures of this chapter are reproduced from [56], which were written together by Dr. Frederik Graw, Dr. Ann-Kristin Müller, Priyanka Fernandes and me.

KO strains.

3.2 Mathematical Model

3.2.1 Mathematical model for erythropoiesis

To design a mathematical model of the blood-stage infection dynamics for Malaria that accounts for RBC age, I take a bottom up approach. Here, I begin with establishing a model for erythropoiesis on the lines of the model proposed in [68]. In this age-structured model, a system of coupled ordinary differential equations tracks population density of RBCs of age τ at time t. The model divides the lifespan of an RBC, τ_{RBC} into n equal segments or compartments, each of duration h, such that $n = \tau_{RBC}/h$. The density of RBC in total blood volume for the ith compartment is represented by $x_i(t)$ (where, $i = 1, \ldots, n$). The production of RBCs takes place at the bone marrow constantly and senile RBCs are removed from circulation, and thus a level of optimal RBC concentration is maintained in the blood. Apart from this, RBCs are lost by a loss-rate of $1/\tau_{RBC}$ from each compartment, such that almost 85% of RBCs are lost until they reach the maximal lifespan τ_{RBC}. A Hill function governs the feedback between RBC concentration at circulation at a time t, given by $X(t)$ and the production new RBCs that enter circulation at time $t + T$, where T is the total feedback delay. The Hill function is parameterized by the maximal production rate of RBCs in the bone marrow, F_0, the concentration of peripheral RBC concentration θ_0 at which the production of RBCs is at half the maximal limit, the Hill coefficient k. The Equations (3.1) …(3.3) simulate the process of erythropoiesis. These equations represent a mean-field approximation of the originally developed system relying on partial differential equations, thereby transforming assumed fixed, constant lifespans of RBC into gamma-distributed lifetimes [68], [12].

$$\frac{dx_1}{dt} = F_0 \frac{\theta^k}{\theta^k + (X(t-T))^k} - \frac{1}{h}x_1(t) - \frac{1}{\tau_{RBC}}x_1(t) \qquad (3.1)$$

$$\frac{dx_i}{dt} = \frac{1}{h}\Big(x_{i-1}(t) - x_i(t)\Big) - \frac{1}{\tau_{RBC}}x_i(t), i = 2, \ldots, n \qquad (3.2)$$
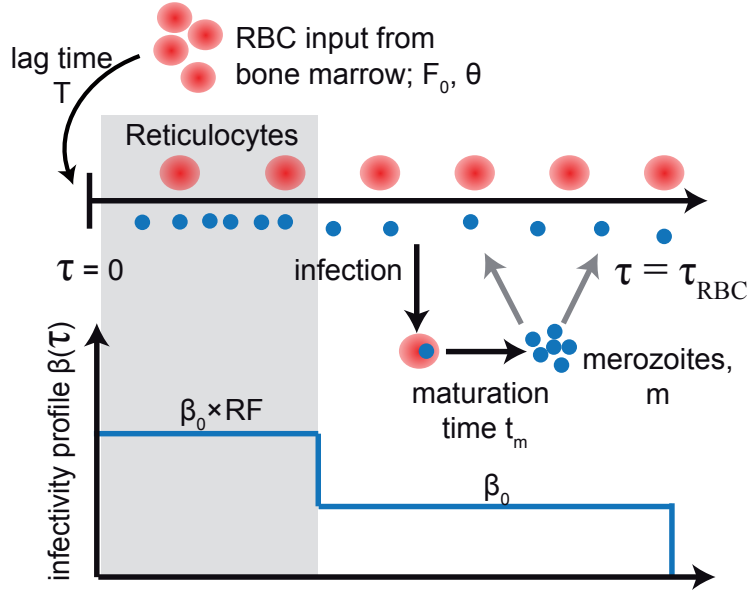
FIGURE 3.1 Model sketch: infection dynamics at the blood-stage
The young RBCs (reticulocytes) are produced in thebone marrow and released to circulate in the body. While circulating, the RBCs (denoted in red circles) age upto τ_{RBC} after which they perish. An infectivity profile $\beta(\tau)$ denoting the different rates of infection specific to reticulocytes and normocytes is shown by the blue curve. It is assumed that the strain infects reticulocytes with an infection rate $(\beta_0 \times RF)$ that is higher than the normal infection rate of β_0 by a factor RF. When infected, an RBC undergoes maturation and bursts to release many merozoites. These merozoites then infect other uninfected RBCs.

$$X(t) = \sum_{i=1}^{n} x_i(t) \tag{3.3}$$

3.2.2 Mathematical model of blood-stage infection dynamics

The erythropoiesis model is extended to include blood-stage Malaria infection on the basis of the work done previously in [22] and [12]. The circulating uninfected RBCs are infected at an age dependant infection rate β_i by potent merozoites at time t, $z(t)$. On infection, the RBC houses the multiplying merozoite to eventually burst after time t_m releasing m free merozoites that each finds an uninfected

RBC to attack and continue the infection cycle. The merozoites last an average time duration of $1/d_m$, after which they perish without leading to a successful infection. The infected RBC concentration per blood volume, $Y(t)$ is also sectioned into g compartments by age such that $g = t_m/h$ yielding $y_i(t)$, $i = 1 \ldots g$. Such a compartmentalization leads to a gamma distributed iRBC maturation time as in the case of uninfected RBCs, but with a mean t_m. The infection rate β_i is defined with respect to RBC age. For reticulocytes, the infection rate increases by a factor RF called the reticulocyte factor, whereas for normocytes, the infection rate is solely defined by β_0 (see [19] and Eq.(3.9), where τ_{Reti} denotes the age at which a reticulocyte matures into a normocyte). The Equations (3.4) …(3.8) mathematically represent the assumed dynamics of malaria infection accounting for RBC turnover.

$$\frac{dx_1}{dt} = F_0\frac{\theta^k}{\theta^k + (X(t-T))^k} - \frac{1}{h}x_1(t) - \frac{1}{\tau_{RBC}}x_1(t) - \beta_1 z(t)x_1(t) \qquad (3.4)$$

$$\frac{dx_i}{dt} = \frac{1}{h}\Big(x_{i-1}(t) - x_i(t)\Big) - \frac{1}{\tau_{RBC}}x_i(t) - \beta_i z(t)x_i(t), \quad i = 2,\ldots,n \quad (3.5)$$

$$\frac{dy_1}{dt} = \sum_{i=1}^{n} \beta_i(t)z(t)x_i(t) - \frac{1}{h}y_1(t) \qquad (3.6)$$

$$\frac{dy_i}{dt} = \frac{1}{h}\Big(y_{i-1}(t) - y_i(t)\Big), \quad i = 2,\ldots,g \qquad (3.7)$$

$$\frac{dz}{dt} = \frac{m}{h}y_g(t) - \sum_{i=1}^{n} \beta_i(t)z(t)x_i(t) - d_m z(t) \qquad (3.8)$$

$$\beta_i = \begin{cases} \beta_0 RF & i \leq \tau_{Reti}/h \\ \beta_0 & i > \tau_{Reti}/h \end{cases} \qquad (3.9)$$

$$(3.10)$$

3.2.3 Average infectivity and reticulocyte preference

Here, I define another term called average infectivity β, which is the infection rate of a merozoite during blood-stage infection. The average proportion of reticulocytes in total RBC population at steady state in mice is 5.8 %. Hence, the average infectivity accounting for the proportion of target cells that have a higher rate of getting infected by a factor RF, is given by $\beta = \beta_0(0.058RF + 0.942)$.

In order to quantify age-specific target preference of a given parasite strain, we formulate reticulocyte preference RP which is a ratio of infected reticulocytes per 100 reticulocytes to infected normocytes per 100 normocytes. Thus, if R and I_R define the concentration of reticulocytes and infected reticulocytes, respectively, and N and I_N the corresponding concentrations for normocytes, the reticulocyte preference is calculated by $RP = (I_R/R)/(I_N/N)$. The reticulocyte factor is a unit in the mathematical system to specify infection dynamics, whereas the reticulocyte preference can be obtained from experimental observations.

3.3 Results

3.3.1 Characterizing the dynamics of erythropoiesis and determining reticulocyte maturation times in the blood

The model presented in Equations (3.1)-(3.3), [55], [68] is fitted to the observed dynamics of RBC concentration in uninfected mice by sampling 10 μl blood every day for five days (Fig. 2.1). Bleeding leads to a decrease in RBC concentration which in turn leads to increased production of fresh RBCs in the bone marrow to counter the loss. This feedback is delayed by time T. The feedback thus triggered is a direct consequence of anemia and its extent depends on the severity of anemia, here modelled with a Hill function [68]. Setting the maximal lifespan for RBC τ_{RBC} at 40 days [69] and Hill coefficient of k at 7.6 [68], other parameters in the model are estimated. The resulting estimates of maximal RBC production rate $F_0 = 5.95 \times 10^4$ cells $\mu l^{-1} h^{-1}$ [4.02, 6.82] and the RBC concentration at which the production rate is half the maximal $\theta_0 = 6.65 \times 10^6$ cells μl^{-1}[5.28, 6.84], approximately 95 % of the RBC concentration at steady state. After testing possible feedback delays of $T = 0, 1, 2,$ and 2.5 days, it was estimated that novel RBCs from the bone marrow enter circulating blood after a lag of $T = 2$ days. All the estimates are in agreement to previously determined parameters for erythropoiesis in mice [55], [68] (see Figure 3.2 and Table 3.1). As the focus of this study is understanding the dissimilarity between reticulocyte dynamics and normocyte dynamics, establishing the parameter τ_{Reti}, the maturation time of a reticulocyte when it ceases to be one and matures into a normocyte is imperative. The model
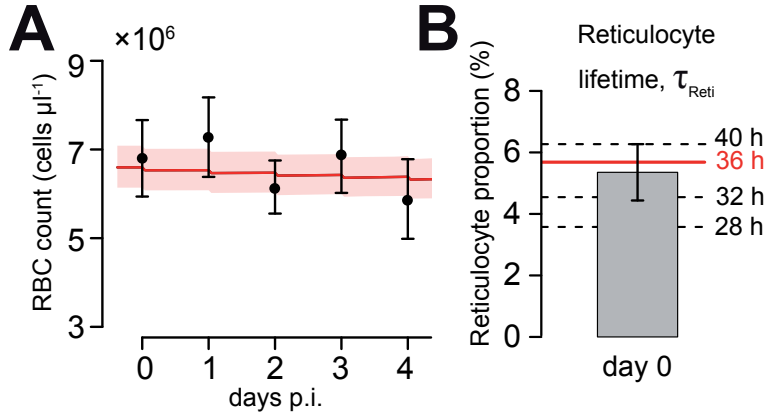
FIGURE 3.2 Change in RBC concentration as estimated by erythropoiesis model and estimation of reticulocyte age

(**A**) The plot shows the measured concentration of red blood cells for naïve mice (mean $\pm$ SD, n = 3), as well as the dynamics predicted by our model (best fitted solid line, 95%-confidence interval- shaded area) using parameter estimates for RBC turnover and reticulocyte production as given in Table 3.1. (**B**) Based on model predictions and the measured proportion of reticulocytes on day 0, we consider a maturation time for reticulocytes of $\tau_{Reti} = 36$ h

predictions for different RBC age compartments were compared to the observed mean proportion of reticulocyte in the experiment (Figure 3.2 B) and τ_{Reti} was estimated to be 36 h or 1.5 days which is in accord with estimates between 1 and 3 days found in [70], [71], [72].

3.3.2 Parasite-induced cell death cannot explain the observed loss in reticulocyte proportion

On examining the experimental data from *P.berghei* ANKA (WT) or *Pb-maLS_05* (-) (KO) infected mice, it is clear that there is a considerable decline in the proportion of reticulocytes around day 3 post infection. This decline is accompanied by an increase in parasitemia (Figure 2.1). The difference in parasitemia is also visible between the two strains as infection progresses, reaching its peak when WT mice show the first signs of ECM (around day 4 p.i.) with the KO only
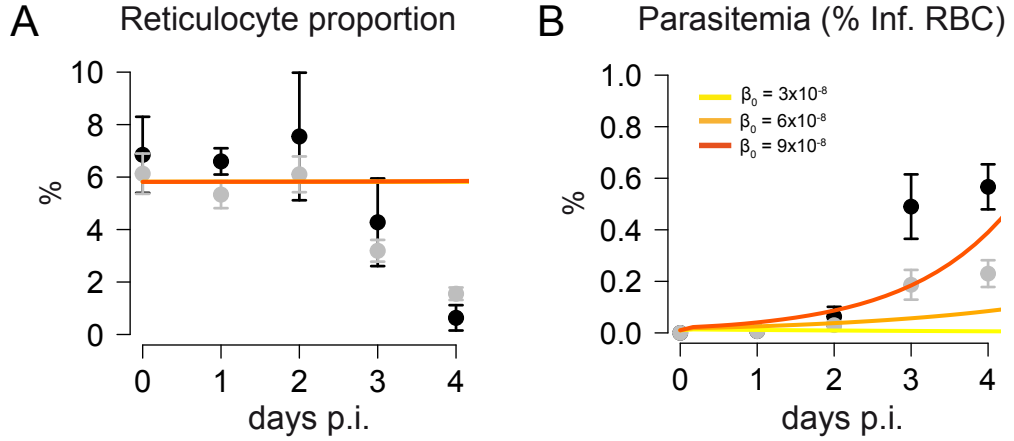
FIGURE 3.3 Homeostatic erythropoiesis does not explain the observed dynamics
The observed dynamics of the proportion of reticulocytes **(A)** and parasitemia **(B)**
for WT (black) and KO (grey) parasites are shown. Colored lines indicate the
predictions by the mathematical model assuming normal erythropoietic feedback
conditions as described by Eqs. (3.1)-(3.8) with different values for the infection
rate β_0 (mz$^{-1}\mu$l^{-1} h^{-1}). Such a model is not able to explain the simultaneous
decrease in the reticulocyte proportion and increase in parasitemia around day 3
post infection.

eliciting half the parasitemia as compared to the WT (0.29 ± 0.03 % KO com-
pared to 0.63 ± 0.05 % WT) (Figure 2.1). The erythropoiesis model is augmented
to incorporate infection dynamics (see Equations (3.4)-(3.9)). The model assumes
that the average lifespan of a merozoite of $1/d_m = 30$ min [73], a maturation time
of an iRBC of $t_m = 24$ h [74, 75] and that an infected RBC releases on average
$m = 9$ merozoites after bursting [74–76]. With these assumptions, on simulating
the model outputs for various β_0 and RF combinations, it is found that the plung-
ing reticulocyte proportion around day 3 p.i. cannot be explained by the increased
parasitemia using the estimated erythropoiesis parameters in Table 3.1. This ob-
servation holds even when assuming a disproportionately high infection rate β_0
or extremely high reticulocyte factor RF (see Fig 3.3). In summary, the decrease
in reticulocyte proportion cannot be accounted for by a preferential reticulocyte
parasitizaion over that of the normocytes.

It is known that malaria not only causes loss of erythrocytes to parasitization,

TABLE 3.1 Estimated parameters for erythropoiesis, disease induced feedback modulation and fixed parameters for parasite infection

Estimated parameter values describing erythropoiesis in mice based on the model as described in Equations (3.1)- (3.9)

Parameter	Description	Unit	Value	References
ERYTHROPOIESIS				
F_0	RBC production rate in Bone marrow	$(\times 10^4)$ cells μl^{-1}h^{-1}	5.95 $(4.02, 6.82)$	[68]
θ	RBC concentration at which half of max. RBC production is reached	$(\times 10^6)$ cells μl^{-1}	6.65 $(5.28, 6.84)$	[68]
T	Delay in RBC production feedback	days	2	[68]
τ_{Reti}	Maturation time of reticulocytes in the blood	hours	36	[71, 72]
τ_{RBC}	Lifetime of RBC	days	40	[69]
k	Hill-coefficient for RBC feedback		7.6	[68]
DISEASE-INDUCED FEEDBACK MODULATION				
λ	Loss-rate of gene-expression	day^{-1}	2.22 $(1.31, 3.05)$	
t_0	Time at which half of the max. gene expression is reached	days	3.70 $(3.28, 4.23)$	
PARASITE INFECTION				
t_m	Maturation time of iRBC	days	1	[74, 75]
m	Average number of merozoites released per burst		9	[74, 75]
d_m	Clearance rate of merozoites	day^{-1}	48	[73]

TABLE 3.2 Parameter estimates for parasite infectivity comparing PbANKA (WT) and *PbmaLS_05*(-) (KO).

Only the ranges of parameters are added to the table, as for *Pb*ANKA (WT) only combinations of β_0 and RF could be determined (structural non-identifiability). For *PbmaLS_05*(-) (KO), it was found that there is no reticulocyte preference, i.e., $RF = 1$. Numbers in brackets represent 95%-confidence intervals of estimates obtained by the profile likelihood method if boundaries could be determined.

Parameter	Unit	*Pb*ANKA (WT)	*PbmaLS_05* (-) (KO)
Infection rate, β_0	$\times 10^{-8}$ mz$^{-1}\mu$l^{-1} h^{-1}	$(0, 4.84]$	$7.82\,(7.36, 8.31)$
Reticulocyte Factor, RF	-	$[22.5, \infty)$	1
Average Infectivity, β	$\times 10^{-7}$ mz$^{-1}\mu$l^{-1} h^{-1}	$1.13\,(1.08, 1.16)$	$0.78\,(0.74, 0.83)$

but quite early into the infection also inhibits erythropoiesis [77–79]. A previous study [78] that investigated this by observing expression levels of various genes that are associated with erythropoiesis. Of relevance from this work is the finding that genes known to show a strong association with erythropoiesis, namely $\alpha-$ globin, $\beta-$ globin major and $\beta - 1-$ globin indeed show a change in their expression levels following malarial infection. This change with time can be modelled using a logistic-loss function as represented in Eq. (3.11).

$$F(t) = \frac{1 + e^{-\lambda t_0}}{1 + e^{-\lambda(t_0 - t)}} \tag{3.11}$$

Here, λ defines the loss-rate of gene-expression or the loss of RBC production and t_0 the time point at which half of the maximal gene expression is reached. On fitting such a model to the data from [78], we estimate $\lambda = 2.22$ d^{-1} (95% - CI $[1.31, 3.05]$) and $t_0 = 3.70$ d $[3.28, 4.23]$ (see Table 3.2 and Figure 3.4). The infection dynamics model is extended to include this malaria-induced erythropoietic modulation hypothesis (i.e.. F_0 in Eq. (3.4) is replaced by $F_0 F(t)$) and the mentioned parameterization is used during all further analyses.
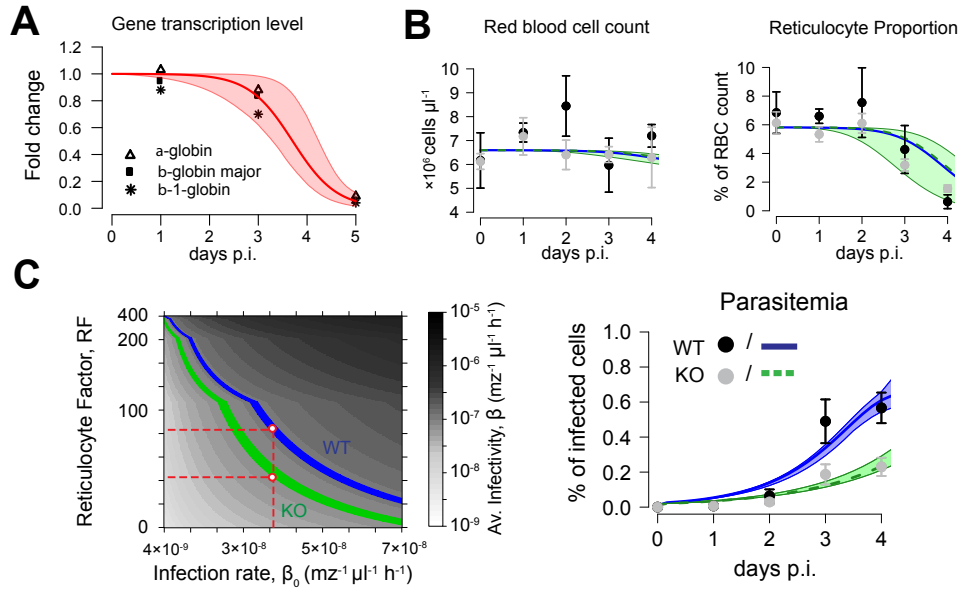
FIGURE 3.4 A panel with results from the infection dynamics model that accounts for disease-induced changes to erythropoiesis

(A). Fold change in expression levels of genes associated with erythropoiesis during malaria infection. Symbols represent gene-expression levels of various genes. Red solid line indicates best fit with parameter values described in Table 3.1 based on 10^4 bootstrap replicates simulated from the distribution given by the gene expression levels at each time point (shaded area – 95% confidence interval). **(B)**. Dynamics of red blood cell concentration, reticulocyte proportion and parasitemia for mice infected by either WT, n = 3 or KO, n = 6. The mean and standard deviation for each group are shown. Model results simultaneously predicting the dynamics of all 3 measurements indicate a lower average infectivity for the WT compared to KO. Shaded areas indicate 95%-confidence intervals. Corresponding parameter estimates are shown in 3.2 **(C)**. Obtained parameter combinations for reticulocyte factor RF and infection rate β_0 indicate a lower average infectivity β per merozoite per hour for the KO parasite compared to the WT. KO parasites have lower reticulocyte factors than the WT if similar infection rates β_0 for both parasites are assumed (red dashed lines).

3.3.3 *PbmaLS_05* (–) merozoites express a reduced infectivity compared to PbANKA WT

The final infection model (see Equations (3.4)-(3.9)) encompasses the basic erythropoiesis parameterization (see Table 3.1) and the extension that accounts for erythropoietic modulation (see Eq. (3.11)). This final infection model is fitted to the experimental data on total RBC count, reticulocyte proportion and parasitemia. Extending the model to account for modulation of RBC production due to infection improves the prediction for the observed dynamics of reticulocyte proportion thereby improving the overall model predictions for RBC count and parasitemia too (Figure 3.4). The estimates of infectivity characterized by infection rate β_0 and reticulocyte factor RF for each of the two parasite strains indicate that the WT strain with an $RF > 22$ shows a more than 22-fold higher preference for reticulocytes than normocytes (see Figure 3.4 and Table 3.2). In contrast to the KO with $RF = 1$, meaning the KO prefers infecting reticulocytes and normocytes equally as the model performs comparable to the model that assumes a preference for reticulocytes ($RF \neq 1$) (AIC 40.7 vs. AIC 42.7). Despite that, the time courses of the experiment are too short to identify definite reticulocyte preference for the two parasite strains. A small value of RF is compensated by a high infection rate β_0 and vice versa, because of which many combinations of β_0 and RF can fit the data equally well (Figure 3.4). Based on the estimates of combinations of β_0 and RF, the average infectivity, defined as the infection rate of a merozoite in the erythropoietic system at the start of infection (see Section 3.2.3), is calculated for both the strains. Interestingly, the KO parasites have a lower average infectivity as compared to WT parasites, thereby producing less potent infections ($\beta = 0.78[0.74, 0.83] \times 10^{-7}\,\mathrm{mz}^{-1}\mu\mathrm{l}^{-1}\,\mathrm{h}^{-1}$ for KO and $\beta = 1.13[1.08, 1.16] \times 10^{-7}$ $\mathrm{mz}^{-1}\mu\mathrm{l}^{-1}\,\mathrm{h}^{-1}$ for WT, numbers in brackets represent 95 %-confidence intervals; Table 3.2). The slower increase in parasitemia for the KO strain (see Fig. 3.4) can be attributed to a less infective KO strain, with its lower average infectivity. If one assumes that infection rate β_0 is unchanged between the two strains, the resulting estimate for RF is consistently lower for KO than that for WT across a wide range of β_0 (Figure 3.4). Thus, our analysis concludes that KO parasites may be less competent than WT parasites in productively infecting reticulocytes

during the early erythrocytic stage of infection.

3.3.4 Testing other hypotheses

Though the central idea of this study is characterizing the KO strain with respect to its infectivity and reticulocyte proportion, in this section it is examined if differences in other infection parameters can justify the low parasitemia observed during KO infection. It is well known that depending on the strain an infected iRBC takes $\sim$ 24-72 h to complete, and between 8 and 32 merozoites are released from every rupturing iRBC [74, 75, 80]. Therefore here it is assessed if maturation time of an iRBC (t_m) or number of merozoites released per iRBC burst (m) for the KO strain are selected distinct to that of the WT strain can explain the diminished parasite-load during early-stage KO infection in the blood. With the infection model that accounts for reduced erythropoiesis, various values for $t_m \in (10, 60)$ h and $m \in (8, 36)$ were tested and the model estimates for parasitemia were compared to the data. The results show that if β_0 and RF that are identical for both WT and KO strains are assumed, the KO strain-iRBCs may take a longer time to burst and produce merozoites as compared to the WT ($t_m = 36$ h (KO) vs $t_m = 24$ h (WT)). Such a delayed maturation of iRBCs would ensure a slowly increasing parasitemia, eventually producing a lower parasite burden on day 4 p.i. than the WT. On the other hand, any $m \neq 9$ for the KO, keeping rest of the infection parameters equal to the WT, could not lead to better parasitemia estimates for the KO.

3.4 Discussion

In Malaria, the disease symptoms occur during the blood-stage of the *Plasmodium* life cycle and this stage is a determinant of the resulting severity of disease. Thus parasite replication and invasion of host target cells during the blood-stage are crucial for designing novel therapeutics and malaria vaccines [67]. Within-host mathematical models have been widely used to understand the *Plasmodium* life-cycle and the host-parasite interaction at various scales for the same system [12, 19, 21, 81, 82]. Here, an age-structured model comprising a system of par-
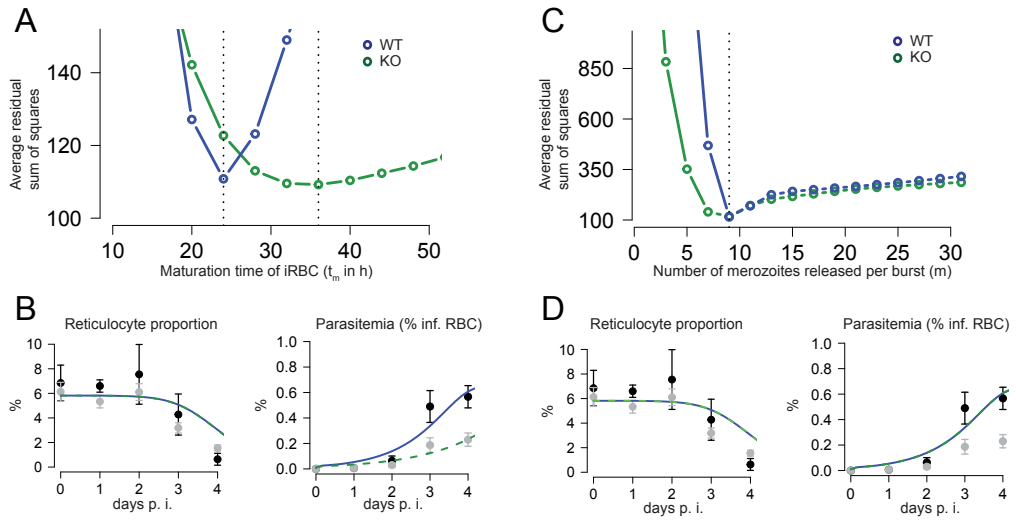
FIGURE 3.5 Testing other hypotheses
(**A**). A longer iRBC maturation of $t_m = 36$h for the KO as compared to $t_m = 24$h for the WT captures the dynamics of (**B**). reticulocyte proportion and parasitemia. (**C**). No other value of merozoites produced from a single iRBC, m, can justify the (**D**). observed difference in infection dynamics between the two strains.

tial differential equations similar to earlier models [12] is deployed to particularly contradict target age-preferences displayed by two parasite strains, the *Pb*ANKA (WT) and *PbmaLS_05* (-) (KO). The age-preference was studied by comparing preference to reticulocytes over normocytes during the early erythrocytic stage of the parasite (upto 4 days p.i.) after infection via iRBCs. From this analysis I found that Malaria hampers erythropoiesis and this phenomenon already contributes to anemia during the early phase of blood-stage infection. The observed tremendous decrease in reticulocyte proportion cannot be explained by a concurrent and very slightly increasing parasitemia (see Figure 3.3). A reduction in erythropoiesis is also reported for *Plasmodium berghei* at later erythrocytic stages in [19]. Other factors including malaria-induced bystander deaths of uninfected RBCs [19,83,84] may explain the loss of reticulocytes, but the phenomenon of bystander death cannot explain the constant level of total RBC count (Figure 2.1) which hints at an age-specific deterioration in the reticulocyte population. Therefore I extended the mathematical model by [12] to account for altered erythropoietic dynamics during malaria infection [78, 79]. This model was fit to the experimental data and I

modelled the reduction in RBCsas a result of reduced production due to changed erythropoietic conditions and loss of RBCs in an age-specific manner to infection. The model confirmed that akin to previously observed [12,15–17,19] property of some *Plasmodium* strains, the *Pb*ANKA strain preferentially infects reticulocytes. A minimum 22-fold higher preference for reticulocytes compared to normocytes in *Pb*ANKA parasites was estimated while considering the early blood-stage of the parasite (Table 3.2). A maximal limit for the reticulocyte factor could not be obtained (Table 3.2) as only combinations of RF and β_0 could be ascertained that lead to similar dynamics of parasitemia and reticulocyte proportion owing to the structurally non-identifiable [85] parameters (Figure 3.4). Cromer *et al.* estimated a value of RF ~ 150 based on data from later stages of infection with *Plasmodium berghei* [19]. If an RF is set to 150 (the estimate from [19]) in our model, the model predicts that 65 % of parasitemia is contributed by reticulocytes on day 4 p.i. (Figure 3.6). This value is larger than the proportion of reticulocytes in the total parasitemia observed on day 4 p.i. in rats infected with *Plasmodium* berghei [18] ($\sim 50\%$). However such a high value of reticulocyte factor is within the range of RF estimated by our model. I also infer that different combinations of β_0 and RF can produce the same output for reticulocyte proportion and parasitemia, thereby pressing the idea that combinations of β_0 and RF should be considered while comparing infection characteristics of two strains. Thus I calculate average infectivity (β) and deduce that *Pb*ANKA parasites are more infectious as they have a approximately 1.5-fold higher average infectivity than the parasites devoid of the *PbmaLS_05* gene (see Figure 3.4). I propose that it is for this reason that infection due to KO strain develops poorly and leads to a lower peripheral parasite load of KO than WT on day 4 p.i.. When I tested other hypotheses than target preference, it was clear that a roughly 2-fold longer maturation time for iRBC infected by the KO could provide an alternative explanation for the observed differing dynamics. This supports the conclusion that deletion of *PbmaLS_05* particularly leads to impaired parasite development and less successful infections in reticulocytes during the initial blood-stage phase. Moreover, the small difference of 1.5-fold elevated RF for the WT, though enough to explain the different dynamics of infection for the two strains, is pessimistic, and the actual difference could even be larger than what is estimated here. Since the mice were sacrificed on the day when WT in-
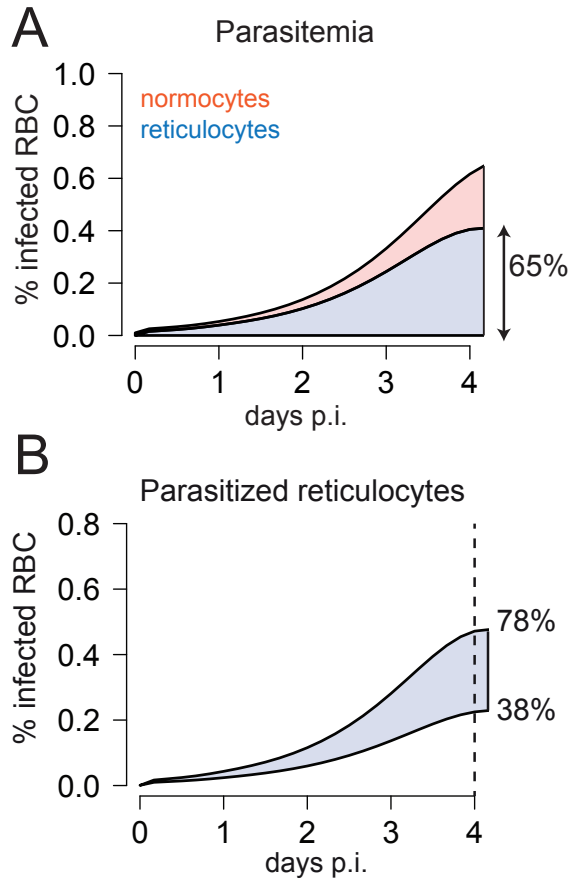
FIGURE 3.6 Comparison of the estimated infection parameters to results from another study

(A) Development of infected normocytes and reticulocytes during infection with WT parasites as predicted by the model using a reticulocyte factor of $RF = 150$ as estimated by [19]. The model predicts that 4 days after infection around 65% of the infected red blood cells are reticulocytes. **(B)** Using the estimated parameter combinations of the infection rate β_0 and RF for *Pb*ANKA (Table 3.2), the model predicts that 4 days after infection in between 38 and 78% of the infected red blood cells are reticulocytes.
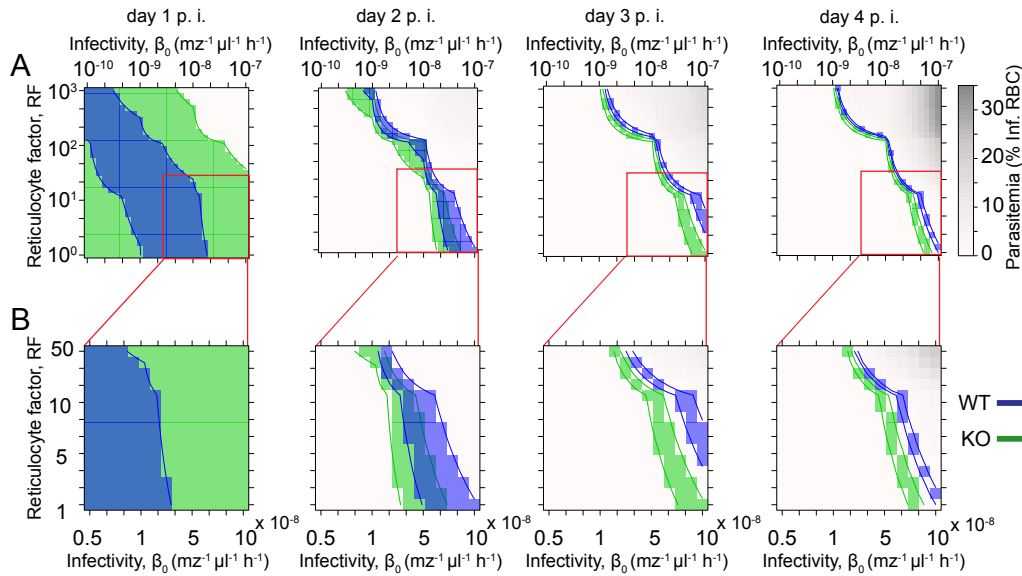
FIGURE 3.7 Distinguishing between the infectivity of WT and KO parasites as the infection progresses through the blood-stage.
(A) The panels the combinations of the infection rate β_0 and reticulocyte factor RF that fit the data for WT (blue) and KO (green) parasites explaining the parasitemia level observed. While infectivity characteristics for both parasite strains overlap during early days post infection, the difference becomes prominent with infection progression. (B) Zoom into a particular region of (A) to improve visual clarity.

fected mice showed signs of ECM, the analysis is restricted to early phase of the infection, thereby affecting the precise identification of infection parameters due to the following reasons: 1). parasite levels are too low and therefore prone to measurement noise and 2). this model predicts that the difference in the strains becomes more pronounced as the infection progresses 3.7. An analysis of long-term dynamics of the two parasite strains is not possible as the WT infected mice develop ECM on day 5 p.i.. Nevertheless, I explored the prediction of this model over a duration of 20 days for the KO strain. This examination made a case for changing infection dynamics after the initial phase of 4-5 days of blood-stage infection (Fig. A.1). To summarize, our analysis in-spite of all the restrictions in predicting a definite combination of the two parameters for WT as well as KO strains, conclusively suggests that deletion of the gene *PbmaLS_05* impairs the infection potential of the parasite thereby causing the infection to not culminate in

serious cerebral complication that is a precursor to ECM.

3.5 Conclusion

On the basis of the analysis via experimental data and mathematical modeling, it is clear that reduced RBC production is a hallmark of blood-stage Malaria, and therefore should be accounted for in the infection model. Additionally, it is inferred that the KO strain has a reduced average infectivity than WT, however it remains to be ascertained if the KO has a lower reticulocyte factor RF or a lower infection rate β_0. One way to decouple the two hypotheses is to observe the infection dynamics of the two strains in the presence of abundant reticulocytes. Such an experiment will shed more light on the target preference of the two strains. In the following chapter, with data from one such experiment that involves pre-treating the animals with Phenylhydrazine (PHZ) and a corresponding mathematical model accounting for the pre-treatment is employed to understand the differing infection dynamics of the two strains.

CHAPTER 4

Blood-stage infection in Phenylhydrazin (PHZ) treated mice

4.1 Introduction

It was concluded in the previous chapter that the deletion of *PbmaLS_05* leads to parasites that have impaired capability of infecting RBCs during the blood-stage of Malaria as they show a lower average infectivity as compared to the WT strain. In this chapter I take these findings ahead and determine whether the KO has the same infection rate as the WT, but an impaired capability of infecting reticulocytes or it has a lower infection rate, but a heightened preference to infect reticulocytes than what is seen in the WT infections. In this study, experimental data from animals that were treated with Phenylhydrazine (PHZ) to have abundant reticulocytes and infected with WT or KO iRBCs is used to model an infection model under perturbed RBC age distribution. PHZ is known to induce artificial anemia, also known as artificial reticulocytosis, thereby changing the age distribution of circulating red blood cells (RBCs).

Some sentences and most of the figures of this chapter are reproduced from [56], which were written together by Dr. Frederik Graw, Dr. Ann-Kristin Müller, Priyanka Fernandes and me. Many sentences have also been taken from the supplemental material of [56], which were completely written by me.

4.1.1 Phenylhydrazine (PHZ) and its usage in inducing anemia in mouse models

For many years, PHZ has been used for experimental induction of anemia in animal models to study hemolytic anemia or anemia caused by destruction or removal of the RBCs from the bloodstream [86]. PHZ causes peroxidation of RBC lipids inducing hemolysis, i.e. the lysis of RBC, which leads to increased levels of extracellular hemoglobin in the blood. Under homeostatic conditions, any hemoglobin produced by hemolysis is reacted upon by certain compounds and is scavenged by macrophages. However, during aggravated hemolysis, the process of scavenging fails to keep up with the increased hemoglobin levels, which in turn leads to a higher level of free heme [87, 88]. The exact molecular mechanisms by which PHZ induces destruction of RBC have not been fully elucidated, and a lot of different processes have been proposed including biochemical modifications, such as ATP decay and increased potassium permeability of cells [89]. It has been observed that lysis is usually confined to mature red blood cells [90]. Reticulocytes are not lysed although their hemoglobin level is affected [89]. Thus, a mathematical model describing the effects of PHZ treatment should consider age-dependent effects of the treatment.

4.1.2 PHZ induced anemia and the resulting erythropoiesis

Anemia, be it non-hemolytic (for e.g. induced by bleeding) or hemolytic (for e.g. induced due to a *Plasmodium* berghei infection) leads to enhanced erythropoiesis. In mice, the dominant site for erythropoiesis is the bone marrow. In addition, the spleen also acts as a minor erythropoietic organ. However, in situations that deviate from normal homeostatic conditions, such as anemia due to bleeding or hemolysis, the spleen becomes a major site of erythropoiesis in order to compensate for the excessive loss of RBCs as soon as possible [90, 91]. Moreau et al. [88] reported the presence of large numbers of erythroid BFU-E progenitors differentiated from spleen precursors in mice under erythropoietic stress. As stated before, treatment by PHZ causes hemolytic anemia and is characterized by the presence of higher levels of free heme in the blood. It has been observed that this anemia re-

sults in low hemoglobin levels (which is in positive correlation with the red blood cell concentration, as shown in Fig. 1 from [92]), reticulocytosis (as a result of the feedback) and splenic erythropoiesis [88]. Of importance here is that Moreau et al. [88] also found a significant lower erythropoietic activity in the bone marrow and a significant higher erythropoietic activity in the spleen during hemolytic anemia as compared to non-hemolytic anemia. Their observations point towards an additional source compartment for erythropoiesis besides the bone marrow when modelling hemolytic anemia dynamics during PHZ treatment.

4.2 Aim of this chapter

This chapter aims at using the same approach as Chapter 3, of using mathematical modelling in combination with experimental data to compare infection dynamics of WT and KO strain. However, the objective here is to modify the existing infection model to account for the existing anemic condition of the mice and any long term effects that are caused by the treatment to the RBC age distribution as well as characteristics of individual RBCs produced post treatment. This model is used to further distinguish between the KO and WT infection dynamics.

4.3 Mathematical Model

Treatment with Phenylhydrazine (PHZ) is used for experimental induction of anemia in animal models to study hemolytic anemia or anemia caused by destruction or removal of RBCs from the bloodstream [86]. Previous studies developed mathematical models to determine and quantify the effect of PHZ on the RBC age distribution and altered erythropoiesis [93]. However, these models were inadequate to describe the experimental data here, suggesting that they incompletely addressed the effects of PHZ. To this end, several different known hypotheses for the effect of PHZ on erythropoiesis were tested [86, 88, 93, 94] by fitting them to the data of the PHZ-control group (Fig. 2.2).

Here, the effect of PHZ is modeled as an extension to the basic model describing erythropoiesis (see Eqs. (3.1)- (3.3)). The additional model components can
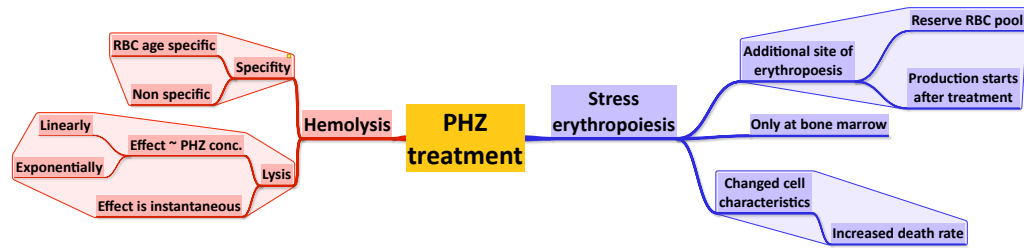
FIGURE 4.1 Schematic showing various hypotheses on the effect of PHZ treatment on erythropoiesis
Chart showing the possible effects of PHZ treatment on red blood cells dynamics categorized according to hemolysis (red) and stress-induced erythropoiesis (blue). The different boxes indicate the unknown effects as they are tested within the models.

be considered to fall into three different categories namely (also see (Fig 4.1)):

1) PHZ induced hemolysis
2) stress induced erythropoiesis
3) altered RBC characteristics

Models incorporating different combinations of the various hypotheses describing these effects (see Fig. 4.2) were constructed and tested in their ability to explain the observed dynamics. In the following, five different representative models are explained in detail.

Model A: This is the simplest of all models. The model assumes that the effect of treatment is instantaneous by immediately lysing a fraction, ρ_0, of RBCs (irrespective of their age) (see Fig 4.2 A). Erythropoiesis occurs according to the previously determined conditions as described in Tab. 3.1, i.e., assuming no stress-induced erythropoiesis.

Model B: As in model A, a direct lysis of a fraction, ρ_0, of RBC upon administration of treatment, but a smaller fraction of reticulocytes γ, as compared to that of normocytes is lysed [93] (Fig 4.2 B).

Model C: In addition to assumptions in model B, this model assumes that extreme hemolysis as a result of the treatment leads to stress-induced erythropoiesis that contributes to RBC production in addition to RBC production from the bone marrow. Thus, RBCs enter the blood stream from extra-medullary sites modeled with

a constant influx of N_P cells, after a time delay of T_P since the time of treatment (Fig. 4.2 C). A value of r close to 1 denotes that RBCs are produced in these organs and a value of r close to 0 denotes that there is a repository of RBCs in these organs ready to be circulated under stress.

Model D: In this model, the assumptions for hemolysis and stress erythropoiesis are as in model C. Besides, this model assumes that the life span of RBCs that are produced after treatment is reduced permanently by a factor η (Fig. 4.2 D) and that this change in RBC characteristic is constant over the 5-day period post treatment considered in our experiment.

Model E: Here, in addition to the previous model, it is assumed that the lifetime of RBCs is assumed to recover over time. Meaning, immediately after treatment, RBCs have a reduced lifetime which will increase linearly to the generally assumed lifespan of $\tau_{RBC} = 40$ days over time. The parameter η' denoting this increasing life time linearly dependent on the time t.

4.4 Results

4.4.1 Exploring the data from PHZ experiment to determine parasite dynamics under altered erythropoietic conditions

The experimental data (in Fig. 2.2) also includes data from the naïve control that were treated with 40 mg/kg on two consecutive days. In these mice, a substantial loss of red blood cell concentration to $\sim 1/3$ of the concentration under homeostatic conditions 2 days is observed after the last treatment with PHZ (2.5×10^6 cells/μl vs. 7.6×10^6 cells/μl, mean values; Figure 2.2). Likewise, corresponding to the decrease in total RBC concentration, there is an increase in the proportion of reticulocytes to upto 50 % of the total RBC concentration at $5-6$ days after the last treatment (see Fig. 2.2). On the other hand, for WT or KO infected, PHZ treated mice, substantial changes in RBC count and reticulocyte proportion are only visible on day 5 p.i.. The RBC count raising to 4.0 ± 0.32 and $3.6 \pm 0.15 \times 10^6$ cells/μl for WT and KO respectively, compared to $6.0 \pm 0.29 \times 10^6$ cells/μl in the naïve
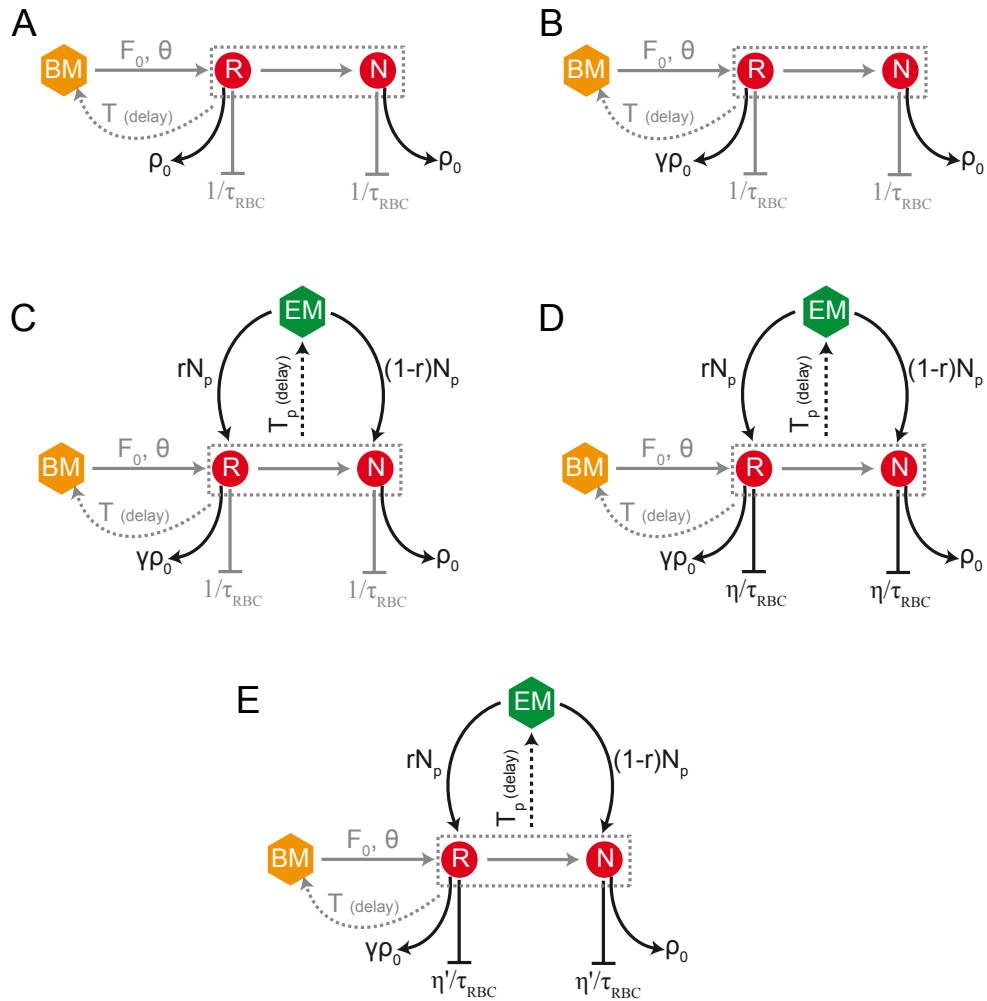
FIGURE 4.2 Sketches of different PHZ models considered

Sketch of the mathematical models including different effects of PHZ treatment on erythropoiesis. Models are shown with increasing complexity from model (**A**)-(**E**) distinguishing between reticulocytes R and normocytes N in the blood and the bone marrow (BM) and extra-medullary sites (EM). All models and the corresponding parameters are explained in detail ahead. The standard parameters are shown in Table 4.1.

control mice (see Fig. 4.4). The infected mice also show a smaller proportion of reticulocytes as compared to naïve mice. However, within the infected mice, the KO infected still have a ~ 3 fold higher proportion of reticulocytes than the

WT infected ($42.6 \pm 2.6\%$ (naïve) $4.8 \pm 1.2\%$ (WT), $15.6 \pm 1.0\%$ (KO); Figs. 4.4). Within the infected groups, it is noteworthy that even though both the groups possess similar parasitemia levels ($22.5 \pm 1.2\%$ vs. $21.0 \pm 2.0\%$), the proportion of infected reticulocytes is higher for the WT than the KO ($24.3 \pm 4.6\%$ (WT) vs. $16.3 \pm 0.8\%$ (KO); Figure 4.4). With these measured values, the average reticulocyte preference RP is calculated as the ratio of the proportion of infected reticulocytes to proportion of infected normocytes. Given these measurements, the average reticulocyte preference RP, calculated by the proportion of infected reticulocytes among reticulocytes divided by the proportion of infected normocytes in total normocytes, resulting into $RP_{WT} = 1.46$ and $RP_{KO} = 0.76$. In agreement with previous results in Fig. 3.4 **(C)**, these observations suggest that deletion of *PbmaLS_05* potentially hampers the parasite's ability to effectively infect reticulocytes.

4.4.2 Modelling the effects of PHZ on erythropoiesis and predicting infection dynamics

Even today, a complete understanding of how PHZ leads to hemolysis and its effects on the age distribution within the RBC population is still missing. Faster aging of RBCs, direct lysis of RBCs and many other hypotheses have been proposed. In fact, a number of these hypotheses are evaluated using mathematical modelling in [93]. The suggested best fit model in [93] failed to explain the experimental data here, mainly because of difference in experimental protocols between the two studies. As a result, I developed many different models and considered the best fitting model for further analysis. The various models were fitted to the naïve control data from Figure 2.2. The results of the comparison are noted in Table 4.2. The parameter estimates for the top three best models are tabulated in Table 4.1. The data exhibit an increasing influx of reticulocytes on one hand, whereas a decreasing net-loss in normocytes post second PHZ treatment on the other(Fig 4.4 **(B)**,**(C)**). This considerable increase in the production of reticulocytes cannot be accounted for solely by the anemia induced production from the bone marrow. While comparing the various models for PHZ treatment shown in Fig 4.2, it was found that the best models explaining the effect of PHZ treatment on erythropoiesis
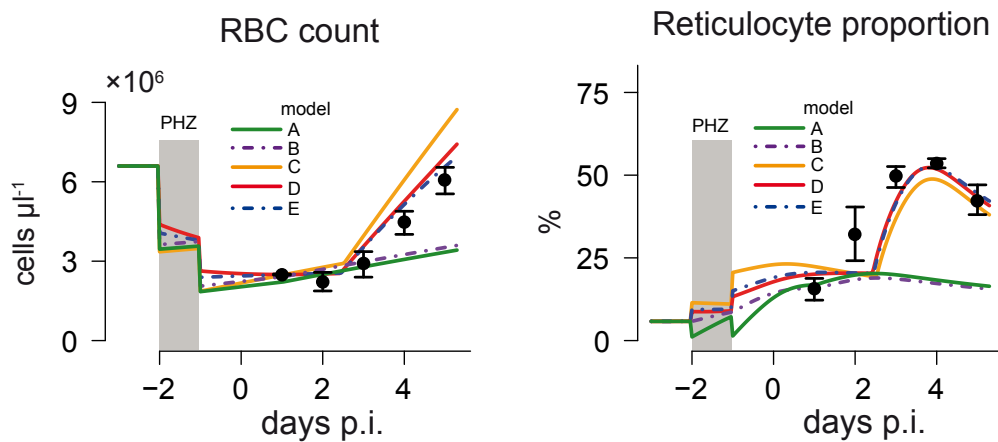
FIGURE 4.3 Output of the various models tested for the effect of treatment on erythro-poiesis

Dynamics of RBC count and corresponding reticulocyte proportion after treatment of C57/BL6 mice with two doses of 40 mg/kg of PHZ at day -2 and -1. The mean and the standard deviation over $n = 3$ mice are shown. Lines indicate the best fits of the models as shown in Figure . While model A and B are insufficient in simultaneously explaining the dynamics of RBC concentration and reticulocyte proportion after treatment, models C-E including stress-induced erythropoiesis by extra-medullary sites significantly improve the fits. Model D and E provide the best fits to the experimental data and are therefore considered in the subsequent analyses. See Table 4.2 for a detailed overview on model performance.

TABLE 4.1 Parameter estimates for models C-E

The values in brackets show the 95% confidence intervals based on profile likeli-

	Model	Parameter	Unit	Value
		ρ_0		$0.524\,(0.50, 0.54)$
		ρ		$0.007\,(0, 0.01)$
	C	T_p	h	$84.5\,(83.2, 85.6)$
		N_p	$\times 10^4$ cells μl^{-1} h^{-1}	$7.8\,(7.5, 8)$
		r		$0.97\,(0.92, 0.99)$
		ρ_0		$0.38\,(0.37, 0.39)$
		γ		$0.006\,(0, 0.04)$
hoods	D	T_p	h	$82.8\,(80.2, 84.1)$
		N_p	$\times 10^4$ cells μl^{-1} h^{-1}	$7.7\,(7.2, 8.1)$
		r		$0.92\,(0.90, 0.94)$
		η		$4.18\,(3.91, 4.46)$
		ρ_0		$0.35\,(0.37, 0.39)$
		γ		$0.006\,(0.002, 0.01)$
	E	T_p	h	$83.3\,(81.9, 86.1)$
		N_p	$\times 10^4$ cells μl^{-1} h^{-1}	$7.3\,(7.0, 7.9)$
		r		$0.94\,(0.89, 0.97)$

assume (i) instantaneous hemolysis with ~ 35 to 50% of the RBC being lysed due to PHZ administration, and (ii) stress-induced erythropoiesis with an additional production of reticulocytes from sources other than the bone marrow. This additional production starts ~ 4.5 days after the second PHZ-treatment has been given (Fig. 4.3). Besides changes to the erythropoietic system, the model also suggests that PHZ alters the characteristics of RBCs produced after the treatment. The treatment reduces the average lifetime of RBC, $\tau_{RBC} \sim 40$ days to $\tau_{RBC} \sim 8$ days (see Fig. 4.4 **(C)** and Table 4.1). The analysis also indicates that alongside a constant death rate (model D), a linearly decreasing death rate (model E) is also a possible explanation for the data (Tables 4.1 and 4.2, Figure 4.3. The infection model specified before (see Eq. ((3.4)- (3.9))) is extended to include PHZ treatment induced effects (from the model D) to establish if the estimated infection parameters for WT and KO previously are also applicable in the changed scenario. By combining the treatment model with the infection model, a mathematical framework that emulates the experimental protocol in Figure 2.2.

TABLE 4.2 Model performance in explaining the naïve control data

The specific parameters that are estimated for each model, as well as the AIC values indicating model performance are shown. The models with the lowest AIC are selected. The AIC is defined as the residual sum of squares divided by the residual degrees of freedom, which is the difference between the number of data points and the number of free parameters.

Model	Parameters to be estimated	AIC (RSS)
A	ρ_0	177.7 (10487)
B	ρ_0, γ	178.3 (10013)
C	$\rho_0, \gamma, T_p, r, N_p$	72.9 (244)
D	$\rho_0, \gamma, T_p, r, N_p, \eta$	19.9 (39)
E	$\rho_0, \gamma, T_p, r, N_p$	19.4 (41)

$$\frac{dx_1}{dt} = F(t) - \frac{1}{h}x_1(t) - \frac{1}{\tau_{RBC}}x_1(t) - \rho_1 I(t = T_p)x_1(t) \tag{4.1}$$
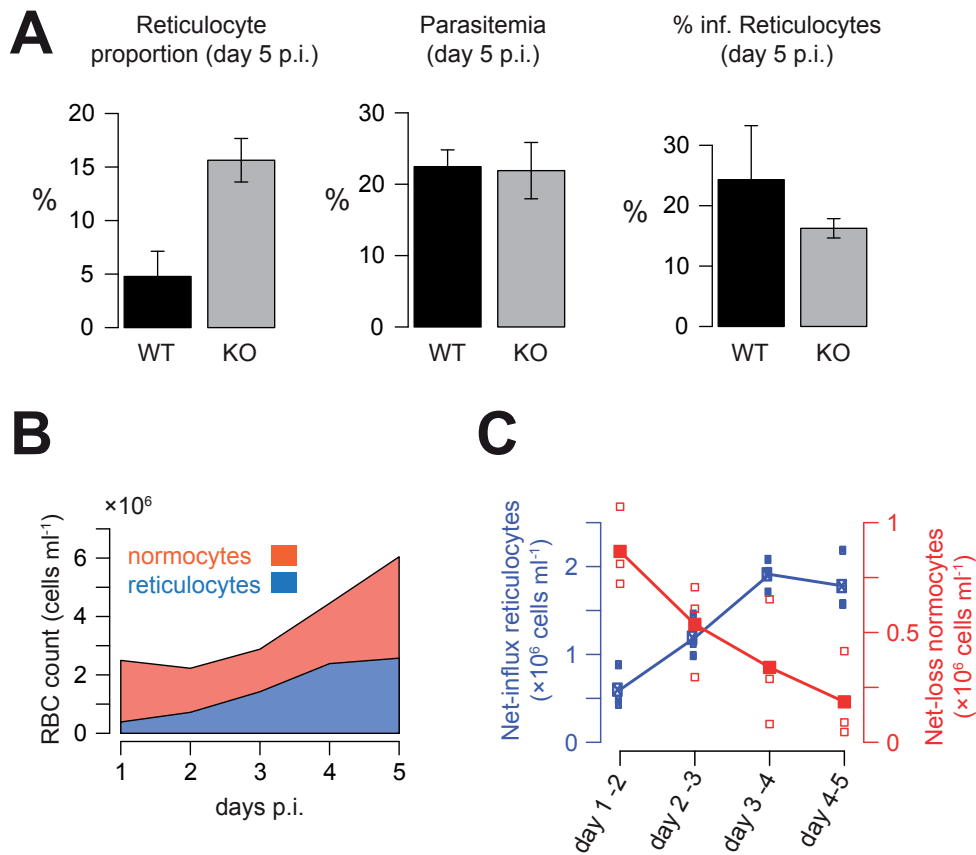
FIGURE 4.4 Conclusions from the PHZ treated and infected mice data
(A) Parasitemia (in % of RBC) above background was detected at day 5 post infection indicating equal levels between WT and KO-infected mice despite a roughly 3-fold higher reticulocyte proportion in KO- compared to WT-infected mice. The percentage of infected reticulocytes was determined as well. **(B)** The measured progression of normocytes and reticulocytes in PHZ-treated but uninfected animals (naïve) indicated an increasing net-influx of reticulocytes (blue line) and a decreasing net-loss of normocytes (red line) up to 5 days post PHZ treatment **(C)**.
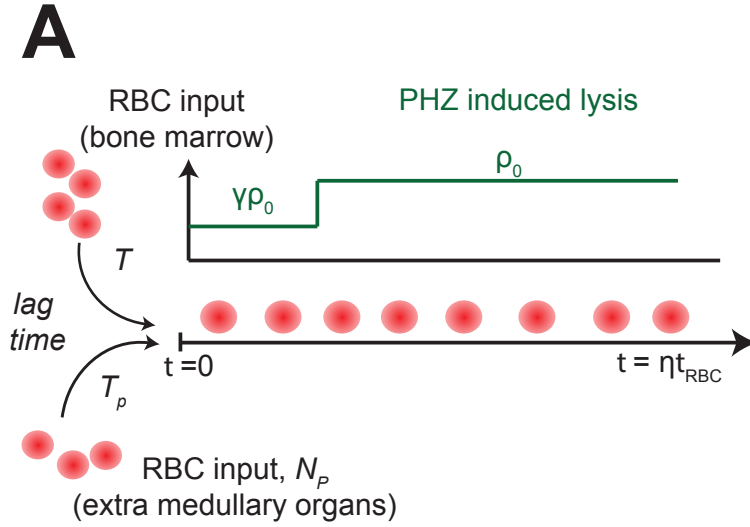
FIGURE 4.5 Sketch of the mathematical model describing the main effects of PHZ treatment on erythropoiesis

The model assumes that normocytes are lost to PHZ induced lysis (shown in green) at a rate of ρ_0, whereas reticulocytes are lost at a rate less than ρ_0 by a factor γ. Under such extreme loss of RBCs, in addition to RBCs produced in the bone marrow, there is an influx of RBCs from extra medullary organs.

$$\frac{dx_i}{dt} = \frac{1}{h}\Big(x_{i-1}(t) - x_i(t)\Big) - \frac{1}{\tau_{RBC}}x_i(t) - \rho_i I(t = T_p)x_i(t), \;\; i = 2,\ldots,n$$

(4.2)

$$\rho_i = \begin{cases} \rho_0\gamma & i \leq \tau_{Reti}/h \\ \rho_0 & i > \tau_{Reti}/h \end{cases}$$

(4.3)

$$F(t) = \begin{cases} F_0\frac{\theta^k}{\theta^k+(X(t-T))^k} & t \leq t_P + \tau_P \\ F_0\frac{\theta^k}{\theta^k+(X(t-T))^k} + N_P & t > t_P + \tau_P \end{cases}$$

(4.4)

This combined model seen in Eqs. (4.1)- (4.4) is further analyzed to establish if the estimated infection parameters for WT and KO previously are also applicable in the changed scenario. I simulated the pre-treatment of mice with PHZ and subsequent infection using different assumptions for parasite infectivity, β_0, and reticulocyte preference, RF. The predicted levels of parasitemia and reticulocyte proportion on day 5 post infection can be seen in Figure 4.6. On simulating for
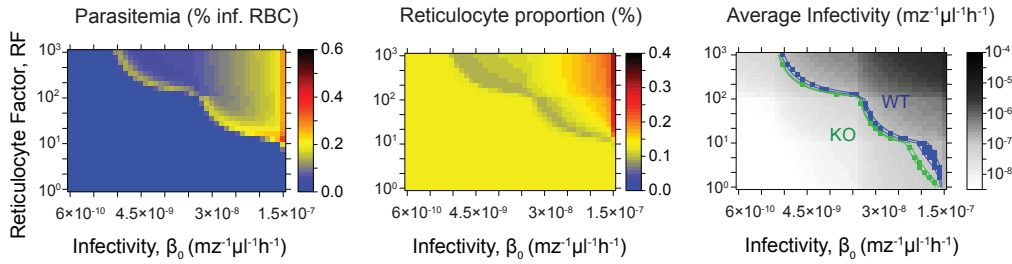
FIGURE 4.6 Model simulations for different combinations of RF and β_0
Predicted parasitemia and reticulocyte proportions after PHZ treatment on day 5
post infection for different combinations of reticulocyte factors, RF, and para-
site infectivity, β_0. The heat-map in grey shows the relevant combinations for
WT (blue) and KO (green) leading to the average infectivity as determined during
untreated infection in the previous chapter. While for the KO-group relevant pa-
rameter combinations lead to matching reticulocyte proportions ($\sim 13\%$) as in the
experimental data, combinations of RF and β_0 for the WT-group predict reticulo-
cyte proportions roughly twice as high as seen in the data.

the KO strain by using the previously determined parameter combinations (Table
3.2), predicted reticulocyte proportions are $\sim 13\%$, comparable to the observed,
but predict a parasitemia of $\sim 1\%$. In contrast, the pre-estimated combinations
of β_0 and RF for the WT strain predict a very high reticulocyte proportion, al-
most twice as high, as seen in the data and parasitemia that are only one-tenth of
the observed. Even directly estimating β_0 and RF based on the observed para-
sitemia and reticulocyte proportion under PHZ treatment, the model predicts that
both groups have nearly all reticulocytes infected ($80 \sim 100\%$), which also does
not agree with the data (Figure 2.2). These results indicate that there is a complex
interplay between PHZ treatment and infection, and modeling them independent
to each other may lead to wrong predictions. The PHZ treatment model, developed
by fitting to the naïve control data does not suffice to predict disease dynamics for
PHZ treated animals.

4.5 Discussion

Phenylhydrazine was for the first time used in experiments in the year 1888
as a drug to induce hemolytic anemia in animals [95]. Since then it has been

used regularly in various experiments to change RBC age distribution towards an increased proportion of reticulocytes to normocytes. The transient effect of this treatment, depending upon the dosage, provides an experimental setup to study the effect of other processes (like Malaria infection dynamics) on the perturbed RBC age distribution. In this Chapter, a two step approach was used to further elicit the differences in WT and KO infection dynamics. In the first step, a PHZ treatment model was developed by fitting the model to the naïve control PHZ treated data and in the second step, the infection parameter estimates from Chapter 3 are used to make predictions for WT and KO infection dynamics under the influence of PHZ. In the first step, various models (from A-E) were tested, and the model D with the least AIC was selected for the second step. In the next step, this model was used to simulate infection dynamics for the two strains based on their respective infection parameter estimates from the previous chapter. This combined model however failed to explain the observed data, suggesting that effect of PHZ is altered under the influence of Malaria infection.

On the basis of the analysis described in Chapter 3 that involved estimating infection parameters for the WT and KO strains in untreated mice, it was found that the KO strain exhibits a lower average infectivity than the PbANKA WT. This difference in the magnitude of successful infections can be explained by two hypotheses. Either the KO parasites have a greater RF but lower infectivity β_0 as shown in Fig. 3.4 **(C)**. This case would mean that the deletion of *PbmaLS_05* restricts the parasite's infectivity to reticulocytes [96]. In mice pre-treated with PHZ that leads to heightened reticulocyte production, such a reticulocyte restriction if shown by the KO strain, would mean that the KO infects more reticulocytes as compared to the WT, causing resulting reticulocyte proportion to be lower in mice infected by KO than those infected by WT. On the contrary, the observed data show 3-fold higher proportion of reticulocytes in KO- than WT-infected mice 5 days p.i. (Figure 4.4 **(A)**) As the levels of parasitemia and total RBC counts are comparable, this indicates enhanced reticulocyte survival during infection with the KO-parasite. Therefore, the analysis of the data from PHZ treated animals rather suggests that deletion of *PbmaLS_05* impairs the ability of the parasite to productively infect reticulocytes during the early infection phase. In the untreated case, the estimated reticulocyte factor RF for the WT is around ~ 1.4 times higher than

the one estimated for the KO when assuming similar infection rates (Figure 3.4). In addition to this, the calculated reticulocyte preference for KO-infected mice after treatment with PHZ is roughly half the size of the one determined for WT-infected mice. Reticulocytes are the preferential targets for most parasite strains [15, 16] and the KO strain's impaired ability to infect reticulocytes could explain the slower development of parasitemia in the KO-infected mice than the WT-infected mice. It turns out that several studies have implicated the need for parasites to infect reticulocytes as a requisite for spreading infection. Metabolomic analysis of the RBC has revealed that reticulocytes possess a higher content of carbon sources and essential nutrients that make them preferred targets for WT parasites during the early blood-stage [97]. Likewise, higher expression of CD47 on reticulocytes was demonstrated to prevent phagocytosis and subsequent clearance of infected cells by the host [98]. Therefore, it can be concluded that the major contributor to the slower multiplication rates of the *PbmaLS_05* (-) parasites is the parasite's inability to develop within reticulocytes. Beyond the blood-stage of infection, it is also found that the *PbmaLS_05* (-) infected mice do not develop experimental cerebral malaria but only severe anemia [13], which corroborates previously proposed correlation between severity of disease progression and cell preference [22, 99].

4.6 Conclusion

Comprehending changes to the erythropoietic system during Malaria infection and PHZ treatment are critical in deciphering the effect of deleting *maLS_05* on parasite infection and reticulocyte invasion. In the analysis that focused on untreated animals, it was found that there are disease induced changes to the erythropoietic system during the blood-stage. Likewise, through the analysis of data from treated animals infected with WT or KO strains, it was clear that a complex interaction of the treatment and ongoing infection, and considering them independent of each other is not a valid assumption while modeling. Nevertheless, the infection estimates from previous chapter and the experimental data from PHZ treated and infected animals substantiate the claim that absence of *maLS_05* indeed leads to a poorly developing parasite, mainly because of the inability of such a parasite to infect reticulocytes as efficiently as the WT. Given the suggested outcome of ab-

sence of *PbmaLS_05* on the productive infection of reticulocytes, the *PbmaLS_05* (-) mutant parasite strain can serve as a tool to study the role of target preference in disease progression and eventual onset or absence of cerebral Malaria. This finding can further be explored in searching the factors that influence activation of immune responses that might enable efficient parasite control.

CHAPTER 5

Malaria parasite development during pre-erythrocytic liver-stage

5.1 Introduction

Thus far I investigated how the malarial WT and KO strain compare in their target cell preferences and infection rates during the blood-stage infection when the mice were infected via the iRBC route. Despite concluding that the KO is a weaker strain than the WT when comparing peripheral parasitemia and ECM causing capability, it is also important to make comparisons between the two during the pre-pathalogical liver-stage. An analysis of these differences can lead to an explanation for why the mice infected via KO sporozoites failed to contract ECM even though they showed similar triggering of immune activation and immune migration to the brain as the WT mice infected via sporozoites.

5.1.1 A silent, nutrient demanding stage before the onset of disease symptoms

Plasmodium parasites cause malaria in vertebrate hosts. The Anopheles mosquito acts as a vector in transmitting this infectious disease. From the sali-
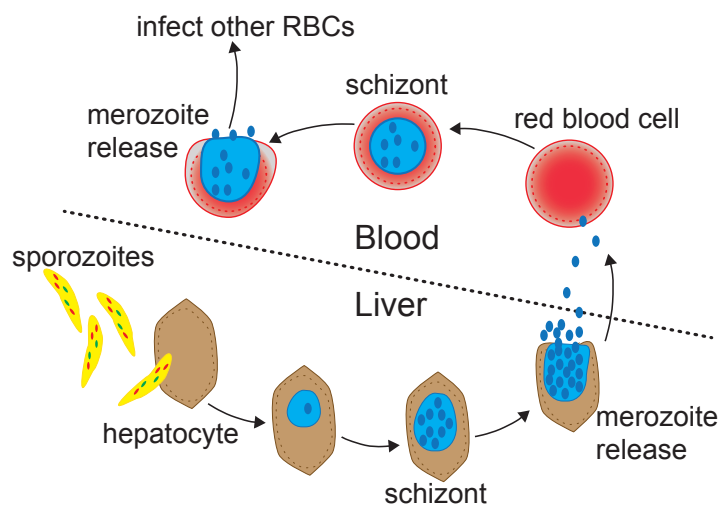
FIGURE 5.1 Part of *Plasmodium* life-cycle within host liver and blood

The *Plasmodium* sporozoites enter the host liver cells. Inside the host cell, each sporozoite undergoes division do form a schizont. The schizont matures further to burst and release free merozoites that leave the liver and enter circulating blood. Here the merozoites infect red blood cells, each of the infected red blood cells mature and burst to release free merozoites that infect other uninfected red blood cells.

vary glands of the mosquito, parasites in the form of sporozoites are released into the skin of the host. These sporozoites are motile and they traverse through blood to reach the liver. Once inside the liver, the sporozoites start targeting hepato-cytes. After a sporozoite settles down in a hepatocyte, a parasitophorus vacuole is formed inside the host cell. This vacuole houses the sporozoite, where the parasite develops further into the trophozoite stage or the feeding stage. The trophozoite then gives way to schizont stage, the stage of multiple divisions. In fact, this rate of division is one of the highest observed rate in eukaryotic cells [8]. This extreme activity is matched by a tremendous increase in nutritional uptake by the parasite, by scavenging nutrients and metabolites from the host cell cytoplasm, in addition to its own metabolism [23, 24]. Hepatocytes are highly active in protein turnover and carbohydrate storage. Therefore hepatocytes represent a favorable environ-ment for *Plasmodium* to thrive and replicate within the mammalian host [100]. During the terminal hours of the liver-stage, the infected hepatocytes burst to re-lease the next stage of the parasite in the form of merosomes that are vacuoles con-taining first generation merozoites [101]. Each schizont ends up producing tens of thousands of merozoites that are released into the peripheral blood stream [102], culminating the clinically dormant liver-stage.

5.1.2 Most promising target for vaccines

Under natural conditions, the number of productively infectious pre-erythrocytic parasites is so low that the liver-stage is a bridge-head of infection in the complex *Plasmodium* life-cycle [103, 104]. The strategy behind most po-tential vaccines is to cause an arrested development in the liver so as to provide a sufficient repertoire of antigens for the immune system to recognize but not caus-ing any successful blood -stage infection [105]. These vaccines aim at inducing protective immunity through mainly but not exclusively $CD8^+$ T cells that are important components of liver-stage immunity [106, 107].

5.1.3 Autophagy and its relevance to liver-stage malaria

Autophagy, in general can be described as a regulated machinery that delivers various components required for intra-cellular degradation (see Fig. 5.2). In re-
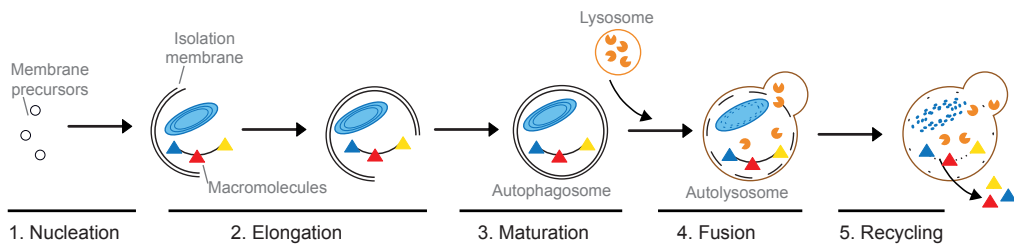
FIGURE 5.2 Mechanism of Autophagy
The figure has been adapted from [111]. The cytoplasmic material to be degraded is is delivered to the lysosomal compartment. The formation of an isolation membrane is initiated by specific proteins. This isolation membrane elongates to enclose cytoplasmic material including organelles and macromolecules. The membrane matures to form an autophagosome. The outer autophagosome membrane fuses with a lysosome, leading to the degradation of its contents. The degraded contents including free nutrients are released into cytoplasm.

ality, in liver 'basal' autophagy is fundamental in maintaining liver cell turnover. Other than this, autophagy can be triggered due to two reasons. On the basis of the type of reason triggering the autophagic pathway, autophagy can be selective or canonical. Selective autophagy is initiated to devour intra- cellular pathogens or specific damaged organelles, and is more targeted in nature. On the other hand, canonical autophagy is stimulated by a nutrient sensing mechanism. Under conditions of stress and starvation, nutritional dearth is compensated by activating canonical autophagy, that causes bulk self-digestions of parts of cytoplasm and cell organelles [24, 108].

Plasmodium schizonts thriving in the hepatocytes are targeted by selective autophagy. The parasite vacuole membrane is laced by autophagic receptors by the host, and is specifically targeted via the selective autophagy pathway [24]. It turns out that some *Plasmodium* strains have also developed a mechanism to avoid this by shedding off these receptors from the surface of their membrane [109]. The others, that do not, end up scavenging on the remnants of the autophagic process, and grow in size [26, 110]. Thus, not just nutrition but also the extent of selective autophagy initiated by the host and the parasite's defence against it becomes the deciding factor in the level of parasite development in the liver.
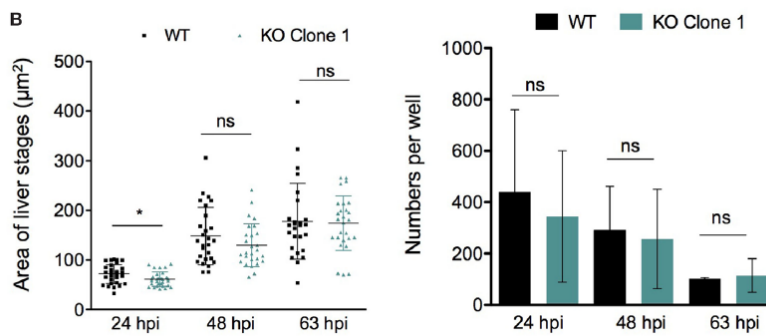
FIGURE 5.3 Experimental data for liver-stage development

HuH7 cells infected with 10^4 sporozoites of either WT or KO parasites were fixed, 24, 48, and 63h post-infection, respectively and stained with parasite-specific markers to visualize the parasite by fluorescence microscopy. Images of parasites inside the liver cells at different time points post-invasion were recorded and sizes of liver stages were measured. The data shown are pooled from two individual experiments for the sporozoite infection (n = 9 mice per group). The statistical significance was determined using the Mann–Whitney U-test. Figure has been reproduced and modified with permission from Priyanka Fernandes [13].

5.1.4 Aim of this chapter

While observing the development of the WT and the KO schizonts, it was evident that the difference between their growth is statistically insignificant. However, on careful consideration (see Fig. 5.3), the KO schizonts, look less developed than the WT schizonts. The fact that one schizont produces merozoites in the order of 10^4 suggests that observed small differences in the liver-stage could potentially release significantly different population sizes of merozoites to set off the blood-stage of infection. Thus, for the sake of completeness and towards achieving the final aim of characterizing the infection pattern of KO, it is imperative, that comparisons between the two during the liver stage should be drawn. As the data from WT and KO infected mice limit such comparisons, this chapter is speculative, and aims at finding ways to overcome this limitation by proposing some hypotheses and evaluating their plausibility:

1) Deletion of *Pb*maLS_05 gene may result in a parasite that is less efficient in utilizing available nutrients.

2) Deletion of *Pb*maLS_05 gene may result in a parasite that is less efficient in escaping selective autophagy.

Using simple mathematical models to simulate the replication and growth of liver parasites and the role of nutritional abundance, I do an analysis to establish how probable the above two hypotheses are.

To design and parameterize the model, data from experiments that investigated the influence of canonical autophagy on parasite establishment, growth and development during the liver-stage of *P. berghei*ANKA in mice [26] has been used. Prado et al. [26] found that autophagy in the form of selective autophagy is one of the mechanisms that benefits the host in parasite clearance. On the contrary, starvation-induced canonical autophagy in infected mice leads to better establishment and growth of the parasite [26]. Thereby implying that nutrition availability is of paramount importance for successful infections during this stage of parasite life-cycle that is characterized by extremely fast nuclear replication rates. Here, the data from these experiments is analysed with an objective to understand how status of host nutrition and parasite nutrition uptake can lead to varying number of infectious merozoites that become the carriers of infection for the blood-stage after released from the liver. A proof-of-concept study is conducted to ascertain if starvation positively impacts parasite development during the liver-stage by developing a mathematical model that best explains the data from [26]. Such a fitted model will help in understanding how autophagy in general, may it be starvation-induced canonical autophagy or infection-induced selective autophagy influences parasite growth in the liver-stage. The results of this study are extrapolated to hypothesize a possible reason for the reduced parasitemia exhibited by KO strain lacking the *Pb*maLS_05 gene during the blood-stage of infection. This study aims at designing future experiments so as to investigate that parasite lacking *Pb*maLS_-05 either induces a low selective autophagic response in the host or has a reduced nutrition uptake capability thereby leading to growth-arrested parasites.

5.2 Mathematical models of parasite development and dynamics of nutrition

5.2.1 Modeling parasite development during liver-stage

In this section, I present a simple ODE model to describe the events taking place after sporozoites have successfully reached and infected hepatocytes. The sporozoites settle into target hepatocytes as early as in minutes and to latest, within 2 h after reaching the liver [102]. Rest of the free sporozoites have been cleared. The liver-stage infection *in vivo* is asynchronous, and all the different intra-hepatic life forms have been observed to exist throughout the duration of liver-stage. However, to keep it simple, the model assumes that all potential infections have already been established, and it will take atleast 48 h for any parasite inside the hepatocyte to mature and burst the hepatocyte to release free merozoites. Thus, during the time frame of interest, no new infections occur and the infected cells are only lost either to host cells clearing the parasite. The parasites are cleared either by the mechanism of selective autophagy or by the hepatocytes being recycled through autophagy at the basal rate. Equation (5.1) illustrates the exponential decrease in infected cell population I with a rate δ.

$$\frac{dI}{dt} = -\delta I \tag{5.1}$$

$$\frac{dS}{dt} = \begin{cases} 0 & ; t \leq \tau_\gamma \\ \gamma S & ; t > \tau_\gamma \end{cases} \tag{5.2}$$

The extent of parasite multiplication during schizont stage is measured by the increase in size of the parasitophorus vacuole. During the schizont stage, the size of the parasitophorus vacuole increases rapidly in-order to house the parasite that is undergoing division at a very fast rate. Equation (5.2) denotes the increasing size S of the parasite vacuole at the rate of γ. I assume that after entering the host cell, the parasite enters the trophozoite stage or the feeding/ rest stage and begins
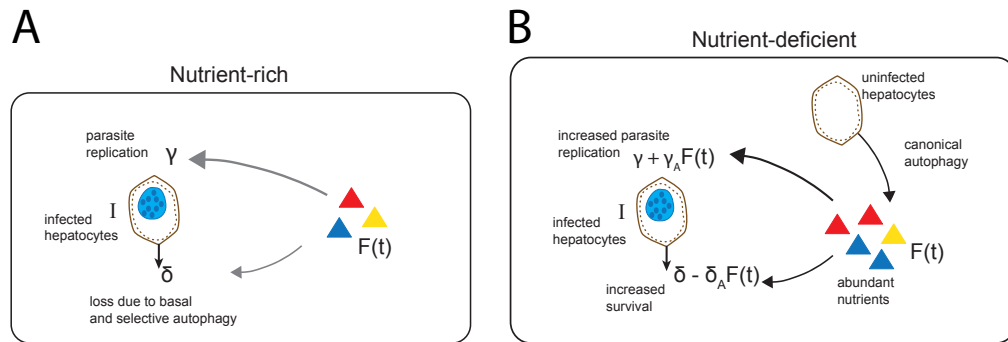
FIGURE 5.4 Parasite development and nutritional staus of the host
Interaction of parasite development and host nutritional status under **(A)**. nutrient-rich (or steady state) environment **(B)**. nutrient-deficient (or starvation) environment.

replicating only after a delay of τ_γ. A sketch of such a basic model is presented in Fig.5.4, **(A)**.

5.2.2 Modeling starvation-induced liver autophagy and the changing nutrition levels

Nutrient deprivation triggers liver autophagy. This canonical autophagy is responsible for metabolic compensation; a term for recycling sugars, fatty acids and amino acids that are products of autophagic breakdown of cytoplasmic components [108]. It was found that mice deficient of *Atg5* could not live through severe neo-natal starvation, and died within 24 h after birth [112]. Therefore, liver autophagy is an important survival machinery in maintaining energy homeostasis [112].

In their quest to know the mechanism of autophagy-dependent release of glucogenic amino acids for glucose production, Ezaki et al conducted experiments on starved naive and starved, *Atg7* deficient mice. They observed that the beginning of canonical autophagy in mouse-liver coincided with the drop in blood insulin levels, starvation-induced autophagic proteolysis occurred in the liver and that the released amino acids are converted to glucose to maintain blood glucose levels [108]. Here, I model the fluctuations in free amino acid levels in the en-

vironment surrounding a hepatocyte using the free-amino acids measurements in liver tissue as presented in [108]. It is evident from these data that the level of insulin in blood drops at $18 \sim 24$ h, which is sensed by the liver. The concentrations of the 9 amino-acids measured in the liver tissue reach maximum after 24 hours of starvation. After this peak, the concentrations start declining, and reach normal levels after 36 hours of starvation. Ezaki et al also observe that the concentrations come back to the normal within a time duration as short as 20 mins after refeeding the animals [108].

$$N(t) = \begin{cases} N_{ss} & ; t \leq \tau_1 \\[2ex] \left(\dfrac{N_{max} - N_{ss}}{\tau_2 - \tau_1}\right)(t - \tau_1) + N_{SS} & ; \tau_1 < t \leq \tau_2 \\[2ex] -\left(\dfrac{N_{max} - N_{ss}}{\tau_2 - \tau_3}\right)(t - \tau_3) + N_{SS} & ; \tau_2 < t \leq \tau_3 \\[2ex] N_{ss} & ; \tau_3 < t < \infty \end{cases} \tag{5.3}$$

I interpolated this data and formulated a mathematical representation $N(t)$ for perturbations in free amino acids concentration as a piecewise function of the duration of starvation (see Eq. (5.3)). N_{SS} stands for amino acid concentration at steady state and N_{max} for the maximum amino acid concentration attained during starvation. The parameter τ_1 is the time at which the nutrient concentration begins to rise above the steady state, τ_2 is the time at which the nutrient concentration is at its peak, τ_3 is the time taken for the concentrations to go back to steady state in spite of continued starvation.

5.2.3 Modelling the effect of starvation on parasite development

The models described in Eq. (5.1), Eq. (5.2) and the effects of starvation $N(t)$ on nutrition (Eq. (5.3)) are combined to mathematically depict the interplay between parasite development in liver and starvation-induced autophagy. Under

the assumption that incidence of canonical autophagy, which leads to excessive availability of free nutrition in the liver tissue, benefits the nutrient demanding shizont stage replication, eventually causing more parasites surviving this stage. In Eqs. (5.4) and (5.5), $F(t)$ is nothing but the function $N(t)$ parametrized to emulate specific starvation durations as per the experimental protocol in [26] (see Chapter 2 Subsection 2.2.2). The loss rate δ in Eq. (5.1) is compensated by the rate $\delta_A F(t)$ in Eq. (5.4).

$$\frac{dI}{dt} = -(\delta - \delta_A F(t))I \tag{5.4}$$

Next, I hypothesize that parasite replication is accelerated and the surviving parasites thrive because of newly available autophagy released free nutrients. The rate of replication γ in Eq. (5.2) is increased by a factor $\gamma_A F(t)$ in Eq. (5.5), whereas the delay τ_γ is the time duration after which the parasite starts growing inside the hepatocyte. A comparison of the changed circumstances under starvation can be seen in Figs. 5.4 A and 5.4 B.

$$\frac{dS}{dt} = \begin{cases} 0 & ; t \leq \tau_\gamma \\ (\gamma + \gamma_A F(t)) & ; t > \tau_\gamma \end{cases} \tag{5.5}$$

5.3 Results

To determine the effect of host nutritional status on parasite survival, in the first attempt I used the combined model in Eq. (5.4), with nutrition fluctuations modeled on the lines of Eq. (5.3). A better approach to fit the data would be to first establish the baseline rate of loss of infected cells and in the second step, extend the baseline model to include effects due to starvation. This approach could not be taken here, precisely because of the lack of appropriate data. Liver- stage malaria parasite is notorious for its very low parasitemia in the liver [48, 113], thereby impeding an analysis *in vivo*. The data available around absolute numbers of infections established in the liver are through *in vitro* experiments [100] and [26]. A drawback of using cell lines (like Hepa1-6 used in [100]) for *in vitro* measurements is that these cells may have lost some characteristics of the cells
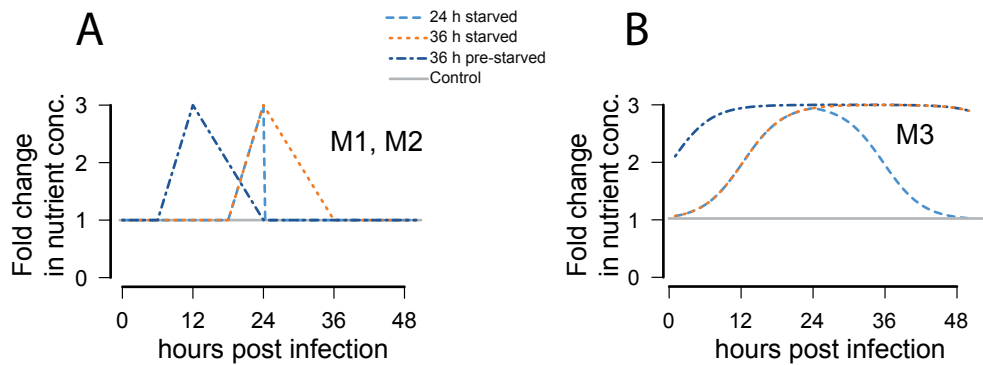
FIGURE 5.5 Fold change in nutrient concentration with respect to duration of starvation **(A)**. Fluctuations in nutrient concentration modelled on the lines of data from [108]. **(B)**. Fluctuations in nutrient concentration modelled as a smooth S-curve.

they were derived from and therefore may not be representative of the infection dynamics occuring *in vivo* [48]. Moreover, sporozoite infectivity is also affected, and therefore the percentage of parasitized cells obtained in *in vitro* infections is relatively low. In summary, using data from an *in vitro* experiment to predict data from *in vivo* experiments would lead to a gross error.

5.3.1 Abrupt changes in free nutrition do not fit the observed parasite growths under different levels of starvation

The model was fitted to the observed differences in parasites that are alive at 40 hpi between various starvation conditions *in vivo*. The data is described in Chapter 2, Subsection 2.2.2 and Fig. 2.4. Once the sporozoites successfully enter the hepatocytes and start maturing inside them, the total number of infected hepatocytes only decreases with time. The number of infected hepatocytes reaches its maximum within 2 hours of the sporozoites reaching the liver. Assuming the maximum number of infections as 1, the model tracks the decline in the infected cell population upto 40 hours post infection.

$$F(t) = \begin{cases} N(t) & ; t \leq \tau_S \\ -\left(\dfrac{N(\tau_S) - N_{ss}}{\tau_S - \tau_R}\right)(t - \tau_R) + N_{SS} & ; \tau_S < t \leq \tau_R \\ N_{ss} & ; \tau_R < t < \infty \end{cases} \qquad (5.6)$$

Under starvation, the decline in the population of infected cells is slowed by a factor of $F(t)\delta_A$. As it is known from [114] and [115] that the maximum increase in the release of free nutrients via autophagy under starvation is two to three fold of the normal rate. Therefore, assuming the basal release of free nutrients to be at 1 under nutrient - rich conditions, the function $F(t)$ is parametrised such that $F(t) \sim (1,3)$ (see Fig.5.5 **(A)**).

$$0 < \delta < 1 \qquad (5.7)$$

$$0 \leq \delta_A \leq \max(F(t))\delta \qquad (5.8)$$

A model denoted as M1 comprises of Eq. (5.4) and nutrition fluctutations modeled using Eq. (5.3) to predict the changing parasite numbers over time I during the liver-stage and Eq. (5.5) with nutrition fluctutations modeled using Eq. (5.3) to predict the changing parasite size over time S during the liver-stage. The model M1 is fitted to the data from [26] with the objective of estimating five parameters. Two of these parameters, δ and δ_A are obtained by fitting the model to the data in Chapter 2, Fig. 2.4 A. As stated earlier, it is expected that the parasite number only decreases with time, in both nutrient-rich or nutrient-scarce situations. Therefore it is only logical to constrain the counter parameter δ_A as in Eq. (5.8).

The resulting estimates are reported in Table 5.1 (see Model M1). The estimated value of δ is very high leaving as little as 0.002% of parasites alive at 40 hpi (Fig.5.6 A, Model M1). Moreover, the model underestimates the proportion of alive parasites in 24 h of starved hosts compared to that in control hosts and predicts no difference between 36 h starved and 36 h pre-starved hosts, at 40 hpi.

On fitting the model M1 to predict the parasite size data in Chapter 2, Fig. 2.4 B to estimate the remaining three parameters, namely γ , γ_A and τ_γ, it was observed that the model M1 fails in predicting the difference in ratios of parasite sizes at 40 hpi in starved animals to control animals (see Fig. 5.7 C).

In the 36 h pre-starved group, at the time of infection, the mice have been starving for a duration of 12 h. A prolonged 12 h starvation may weaken the host, thereby affecting its immune response. Hence, there is a high chance of more successful infections taking place in this group of mice than the other starved groups that began their starvation period only after the intravenous sporozoite infections. Assuming a 1.2-fold higher initial number of infected hepatocytes for the pre-starved group, model M2 is introduced. This model is fitted to the data and the five parameters (same as model M1) are estimated again. Using model M2 though improves the prediction of the parasite number in the pre-starved group (see (5.6) B, model M2), it does not improve the prediction of parasite number in 24 h starved group (see (5.7) B, model M2). In addition to this, both the model M1 and M2 predict a lower parasite size for the pre-starved group than 1). predictions of the 36 h starved group as well as 2) observed parasite number for 36 h pre-starved group (see Fig. (5.7) C). Thus, in general, both the models M1 and M2 (as a modified M1) fail to capture most of the characteristics of the data (see Fig. (5.6) D, model M1 and M2).

5.3.2 Gradual and persistent changes in free nutrition fit the observed parasite growths

In the models M1 and M2, the fluctuations in concentration of amino acids started late (around 18 h), reached a peak quickly (within 6 h; i.e. at 24 h of starvation), dropped to the normal concentration in a short span (within 12 h; i.e. at 36 h of starvation) and refeeding immediately brought down the concentration levels to normal (within 20 mins). The evidence for such dramatic changes in amino acids concentrations were observed by Ezaki *et al.* (in [108]) at the tissue level. One may argue that the nutritional status in the liver tissue or surroundings of a hepatocyte may be different than the status quo inside the hepatocyte. The cells may start experiencing dearth in nutrition earlier than their surroundings. Addi-
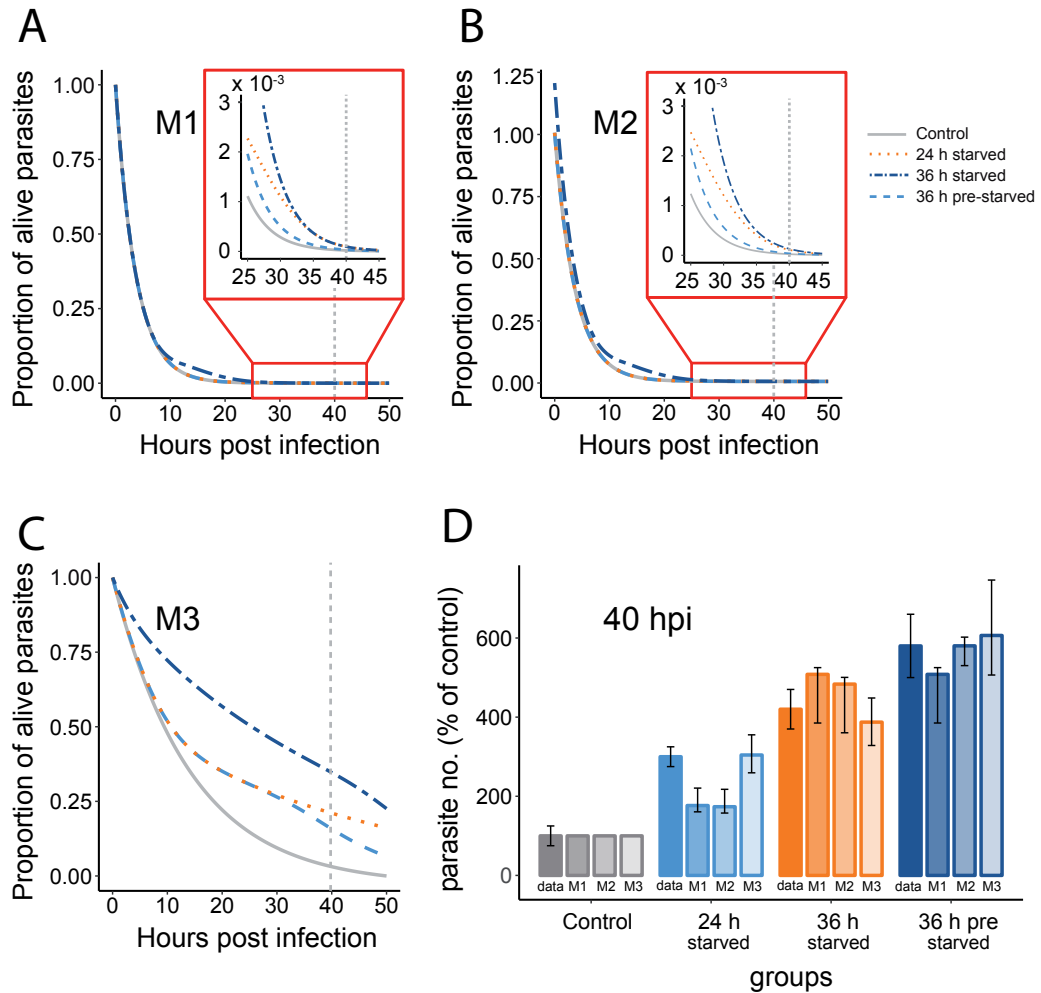
FIGURE 5.6 Comparison of number of parasites predicted by various liver-stage models Model estimates of parasite numbers for Control, 24h starved, 36h starved, and 36h pre-starved for (**A**) Model M1, that assumes abrupt changes in free nutrition as proposed in [108], (**B**) Model M2, same as M1, except assuming more initial numbers of parasites in the pre-starved case, (**C**) Model M3, with nutrient concentrations following an S-curve. (**D**) Comparison of all model outputs with error bars showing 95 % confidence bounds based on profile likelihoods alongwith the data showing parasite numbers at 40 hpi, the parasite numbers at 40 hpi for the control group are considered to be 100%.

TABLE 5.1 Parameter estimates for different models

Parameter estimates with 95% confidence intervals (based on profile likelihoods)

for model M1 and M2

Model	Parameter	Unit	Value
M1	δ	h^{-1}	$2.7[1.8, 4.0] \times 10^{-1}$
	δ_A	h^{-1}	$1.8[1.5, 2.0] \times 10^{-1}$
	γ	h^{-1}	$1.0[0.7, 4.0] \times 10^{-3}$
	γ_A	h^{-1}	$3.0[0.9, 8.0] \times 10^{-2}$
	τ_γ	h	$17.5[15.2, 18.5]$
M2	δ	h^{-1}	$2.8[1.8, 4] \times 10^{-1}$
	δ_A	h^{-1}	$1.7[1.5, 2.0] \times 10^{-1}$
	γ	h^{-1}	$1.0[0.7, 4.0] \times 10^{-3}$
	γ_A	h^{-1}	$3.0[0.9, 8.0] \times 10^{-2}$
	τ_γ	h	$17.5[15.2, 18.5]$

tionally, there may be a lag between the concentrations varying at the tissue level and those varying at the cell level if one accounts for the time taken for nutrition transport into an individual cell from the extracellular space. This lead to replacing of the piecewise function $N(t)$ described in Eq. (5.3) by a logistic function $\tilde{N}(t)$ (see Eq. (5.9)). Here a third model M3 is introduced, which comprises of the exponential loss in alive parasites (see Eq. (5.4)), the dynamics of parasite size (see Eq. (5.5)) and function $\tilde{N}(t)$ from Eq. (5.9). In Eq. (5.9), $\tilde{N}_{ss}$ stands for the amino acid concentration at steady-state or nutrient-rich situation, $\tilde{N}_{max}$ for the maximum amino acid concentration attainable and τ_S is the starvation time duration. k and τ_0 are parameters of a standard logistic function. For the time during which animals are starved (i.e. $t \leq \tau_S$), $\tilde{N}(t)$ is a logistic curve, whereas for time after refeeding (i.e. $\tau_S < t < \infty$), $\tilde{N}(t)$ is an inverted logistic curve. The model assumes that the increase and decline of the nutrient concentration are symmetrical

about $t = \tau_S$ (see Fig.5.5 B).

$$\tilde{N}(t) = \begin{cases} \tilde{N}_{ss} & ; \forall t \text{ under nutrient rich conditions} \\[2ex] \dfrac{\tilde{N}_{max} - \tilde{N}_{ss}}{1 + e^{-k(t-\tau_0)}} + \tilde{N}_{ss} & ; t \leq \tau_S \\[2ex] \dfrac{\tilde{N}_{max} - \tilde{N}_{ss}}{1 + e^{-k(2\tau_S-t-\tau_0)}} + \tilde{N}_{ss} & ; \tau_S < t < \infty \end{cases} \tag{5.9}$$

This model was then fitted to the data as the previous models, the estimates of various parameters are listed in the Table 5.2. With this model, there is a sizable population 6 % of parasites surviving upto 40 hpi (see Fig.5.6 C, Model M3). Not only that, the premise of gradual and sustained transitions of nutrient concentrations results in difference in the parasites surviving under 36 h starvation and 36 h pre-starvation (see Fig.5.6 D, Model M3). With an AICC = 0.33 (vs AICC = 20 for model M2), model M3 performs better than M2 in predicting the parasite numbers and parasite size under various starvation conditions.

TABLE 5.2 Parameter estimates for model M3

Parameter estimates with 95% confidence intervals (based on profile likelihoods)

Model	Parameter	Unit	Value
	δ	h^{-1}	$7[1, 10] \times 10^{-2}$
	δ_A	h^{-1}	$2[1.9, 2.8] \times 10^{-2}$
	γ	h^{-1}	$1.1[0.3, 3.8] \times 10^{-1}$
M3	γ_A	h^{-1}	$3[1, 8] \times 10^{-3}$
	τ_γ	h	$17.5[15.2, 19]$
	k	$-$	$0.3[0.1, 0.5]$
	τ_0	h	$12.3[10, 18]$

5.4 Discussion

In this chapter, I aimed at finding a qualitative relationship between parasite development and nutritional status of the host. The model M1 estimated a very
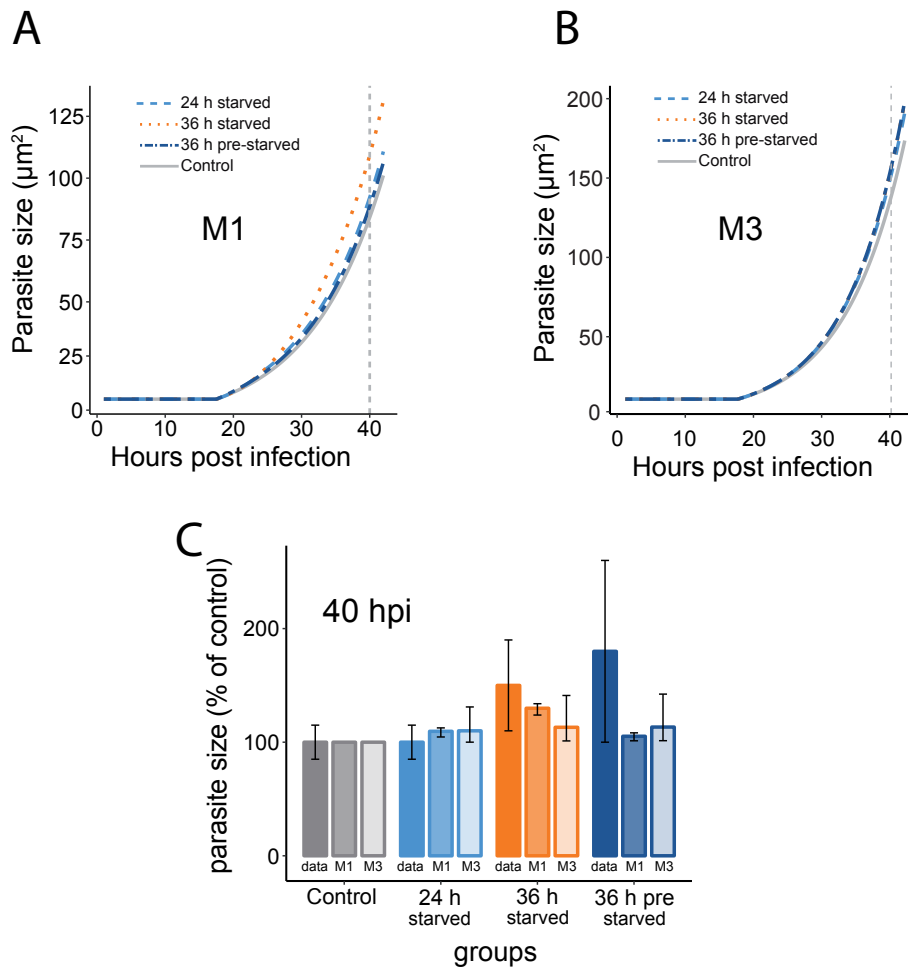
FIGURE 5.7 Comparison of size of parasites predicted by various liver-stage models Model estimates of parasite size for Control, 24h starved, 36h starved, and 36h pre-starved for **(A)**. Model M1, that assumes abrupt changes in free nutrition as proposed in [108], **(B)**. Model M3, with nutrient concentrations following an S-curve. **(C)**. Comparison of all model estimates with data showing parasite size at 40 hpi, with error bars showing 95 % confidence bounds (based on profile likelihoods) on the model output. The parasite size at 40 hpi for the control group are considered to be 100%.

low number of parasites left at 40 hpi, and predicted no difference in the parasite numbers at 40 hpi between 36 h starvation and 36 h pre-starvation groups (see Fig. 5.6 A and D). The second model M2 was then introduced to check if higher initial numbers of parasites in the pre-starved case, could improve the model fits. Though this change in the model lead to a better prediction of the pre-starved case, the parasite numbers were still underestimated for the 24 h starved group (see Fig. 5.6 B and D). Even in estimating the parasite size, both the models M1 and M2 (which had identical equations for the change in parasite size with time) performed poorly (see Fig.5.7 A and C). This time, the 36 h pre-starved group was estimated to have parasite size smaller than that of 36 h starved group which contradicts the observations made in [26] (see Chapter 2, Subsection 2.2.2, Fig 2.4). The model M3, with a logistic relationship between the starvation time and concentration of free nutrition lead to better fits for the parasite growth that included the measured alive parasite numbers and size of the parasite.

The liver-stage of *Plasmodium* lasts for ~ 52 h in rodents [113]. During the late phase of this stage, the infected hepatocytes burst to release merozoites contained in the merosomes. The average parasite fitness at the end of the liver-stage is a pre-cursor to the extent of blood-stage infection. The liver-egressed merozoites pass the lung and infect RBCs. Here a new term, average parasite fitness $P(t)$ is defined which is the average number of merozoites relative to the control released at time t from the liver to carry on the blood-stage infection. As discussed earlier, the size is directly proportional to the number of divisions undergone inside the parasitophorus vacuole to produce merozoites. Therefore $P(t)$ is calculated as a product of the number of alive parasites and the mean size of a parasite at a given time. Using the model M3 to predict I (see Eq. (5.4)) and S (see Eq. (5.5)) over time, the average parasite fitness P is calculated over time. From the predictions, it is clear that most number of merozoites will be released from the liver during the 36 h pre-starved case, followed by the 36 h starved mice, and then by the 24 h starved mice. This clearly indicates that a starved host is beneficial for the liver-stage parasite. Even though the gain in parasite size is only ~ 1.2-fold (see Fig 5.7) in the most extreme starvation case (36 h pre-starved), due to the dual effect of gaining in parasite numbers (~ 5.8-fold, see Fig 5.6) and parasite size (~ 1.2), the resultant fold increase in the population size of egressed merozoites is quite large
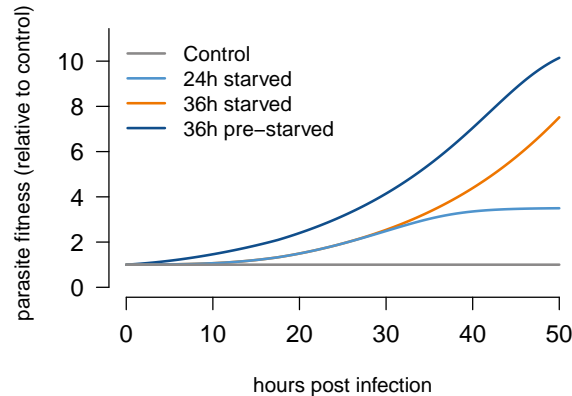
FIGURE 5.8 Parasite fitness $P(t)$ as predicted for the three starvation groups relative to control.
The fitness of the parasite increase with the extent of starvation of the host. For a host that is 36h starved, with 12h pre-infection and 24h post-infection, the product of total parasite parasite number and mean size of the parasite is approximately 10 times than for the parasites that infect a normally fed mouse.

(~ 10 see Fig. 5.8). Assuming that under controlled conditions $\sim 10^3$ merozoites are released per infected hepatocyte that bursts, at the culmination of liver-stage, $\sim 10^4$ merozoites will be released in a host that was 36 h pre-starved . In addition it is also evident from the analysis that under nutrient-rich environment (from the point of view of the parasite), the liver-stage *Plasmodium* certainly prefers to keep more parasite infected hepatocytes alive, rather than higher multiplication inside each infected hepatocyte. Even though extreme starvation of the host is beneficial for the parasite, there exists a trade-off. Starving host would lead to better thriving parasites, but an extremely starved host may succumb to starvation, leading to a defeated parasite.

Intracellular pathogens like *Plasmodium* depend completely on the host machinery for nutrients. For these pathogens, nutrients act as source of energy, regulators of various functions including metabolism and growth [116]. Mancio et al observed that *Plasmodium* blood-stage parasites adjust their multiplication rate corresponding to host dietary calorie changes [116]. It was found that peripheral parasitemia was significantly lower in calorie restricted hosts than supplemented

hosts in the erythrocytic stage. In addition, the experimenters were also able to change severe disease systems in calorie restricted hosts, as such animals did not develop experimental cerebral malaria in contrast to their supplemented counterparts [116]. These results are contrary to what has been observed during the liver-stage in [26, 27, 100], where nutrition restriction or starvation of the hosts leads to better thriving parasites. The liver and blood stages of Malaria are good examples of the two kinds of relationship that exist between host nutritional environment and parasite fitness [117]. In the liver-stage, the host environment is negatively correlated with parasite environment [26, 27, 100], whereas in the blood-stage, there exist a positive correlation between the two factors [116].

Here, by developing an adequate mathematical model that predicts the data measured by [26], it has been established that parasite growth during the liver-stage absolutely depends on the balancing act of autophagy, that on one hand selectively eliminates the parasite and on the other hand enhances growth of the parasites by releasing excess nutrients in the process of cellular degradation. In [26], starvation was used as a tool to highlight the role of autophagy in the liver in nurturing healthier parasites that eventually lead to increased parasite load at the end of the liver-stage. During starvation-induced canonical autophagy, liver acts as a source of nutrition for various organs. Thus, in case of liver-stage malarial infection, the usual host-parasite relationship of starved host leading to underdeveloped parasite is reversed, and *Plasmodium* ends up developing even better while infecting a starved host. These experimental observations and a qualitative proof of the hypothesis that autophagy promotes parasite growth in the liver does not only highlight the role of autophagy but also emphasize that abundance of nutrition for the parasite gives impetus to parasite growth. Therefore, site of infection, host nutritional status and the current stage of parasite life-cycle are important factors governing the interplay of host nutrition and parasite survival and growth. In summary, studies analyzing both the stages, liver-stage ([26], [100] and [27]), blood-stage ([116]) directly imply that nutrition availability in the environment and the parasite's capability of taking up these nutrients are important factors in parasite establishment in the host, the resulting parasitemia and severity of disease in Malaria.

Fernandes *et al.* in [13] observed that the gene *Pb*maLS_05 (that was deleted

to produce the KO strain) localizes to the apicoplast during liver and blood sch-
izont stages. A cell organell, apicoplast is a unique biological feature of *Plas-
modium* and other apicomplexan parasites [118]. The functions of the apicoplast
range from well characterized fatty acid synthesis, isoprenoid precursor synthesis
and housekeeping to so far poorly characterized import and export of metabolites,
production of energy and reducing power and the growth and division of the or-
ganelle [119]. The apicomplexan parasites have a complex life-cycle that spans
more than one host and more than one organ inside the host. The apicoplast capac-
ities are essential only to parts of parasite life cycle, and differ amongst the parasite
species. For example, apicoplast fatty acid biosynthesis is essential to *Toxoplasma*
parasite (another apicomplexan) living in mice. However, in the case of *Plasmod-
ium* in mice, apicoplast fatty acid biosynthesis is redundant in the blood-stage, but
crucial in the liver-stage [120].

In this chapter, a proof-of-concept study to check the positive correlation be-
tween host starvation and parasite fitness during the liver-stage was done that high-
lighted the importance of nutrition availability and nutrition uptake capability of
the parasite during liver-stage in disease progression. This qualitative understand-
ing along-with the so far discovered functions of the apicoplast and the observa-
tions made by [13], the following two hypotheses can be put forward.

1) *PbmaLS_05* may have a role to play in the exchange of metabolites across
   the PVM and host cell cytoplasm. The reason for KO under-developing
   in the late liver stage, could be its inability in capturing and/or utilizing as
   many nutrients as the WT, and therefore leading to less number of mero-
   zoites being released from the liver to the blood at culmination of the liver-
   stage and commencement of the blood-stage. A study found that an enzyme
   Acetyl-CoA carboxylase (ACC), expressed in the apicoplast, is required for
   host biotin metabolism during liver-stage development and has no function
   during the blood-stage [121]. This points at the role of apicoplast in syn-
   thesizing nutrients during the liver-stage and a probable direct link between
   host nutritional status and parasite growth. Thus, in our case, *PbmaLS_05*
   could be implicated as not a necessary but a beneficial participant in parasite
   nutrition uptake and utilization.

2) The gene *PbmaLS_05* may have a role to play in the stimulation of selective

autophagy. The KO strain may be better at hiding from the initial response of the host-liver, the so-called selective autophagy. As a result of which, less parasites may be eliminated in the liver-stage than in the case of WT infection. However the parasites that survive, may be underdeveloped owing to nutrient constraint that could have been elevated, had the parasite induced selective autophagy that would have been instrumental in producing nutrients as a by product. In this scenario too, the underdeveloped KO schizonts would end up producing less number of merozoites as compared to the WT, thereby leading to a disadvantage for the parasite at the start of the blood-stage.

The future experiments could focus on analyzing the potential role of *PbmaLS*_05 from this perspective.

5.5 **Future work**

In a bid to clearly establish if deletion of *Pb*maLS_05 diminishes the parasite's nutrition uptake and/or utilization ability, further investigation is required and in this section I suggest an experimental protocol on the lines of [26] and [13] for this. Two groups of C57BL/6 mice divided into a control group, or groups fasted for 24 h or 36 h or 36 h pre- straved (12 h prior to infection and 18 hpi) to be infected with 2×10^5 WT or KO sporozoites. For all mice, livers are to be harvested at 40 hpi for histology analyses to record the total number of parasites alive and average size of the parasite inside the hepatocytes. The mice starved for various duration would ensure a magnification of the difference between WT and KO parasite development (if any). As a precaution, it should be ensured that the mice in the starvation groups are 'starve-synced' meaning that care must be taken that the mice have a similar nutritional status before start of the experiment as explained in [48]. Such an experiment will disentangle the difference in WT and KO parasites during the liver-stage of infection. If it is concluded from this experiment that there is no significant difference in the WT and KO strains during their life-cycle in developing from sporozoites to merozoites, our main speculation that the two strains differ only during the blood-stage of infection will be cemented even

more. On the other hand, if it is concluded, that the KO differ significantly during the liver-stage, further investigation would be needed to find if the KO strain triggers a weaker selective-autophagic response in the host as compared to the WT. After quantifying the difference in the parasite load during the liver-stage for both the strains and the blood-stage infection for the two strains with different initial number of free merozoites that have egressed the liver ready to infect RBCs in circulation should be looked at. Another interesting aspect to investigate will be to ensure if *Plasmodium* also manipulates to induce host cell autophagy to enhance its capture of host nutrients as the other apicocomplexan parasite *Toxoplasma gondii* [122], [123]. Based on these experiments and more information on *Plasmodium* parasite's intake inside the hepatocyte, the model presented here should be enhanced to represent a more real picture of the relation between host nutrition, parasite development and the resultant egress of parasite material to the blood-stage.

CHAPTER 6

Decoding Experimental Cerebral Maralia (ECM) pathogenesis by comparing WT and KO infections

6.1 Introduction

Cerebral Malaria (CM) is one of the leading causes of severe Malaria and thereby Malaria-associated deaths. In the year 2016, out of the recorded 216 million cases of malaria, 445,000 cases culminated in death [1], $\sim 13\%$ of these deaths were due to CM [30]. At present, when Plasmodium has started to develop anti-malarial drug resistance [32] and the low efficacy of the RTS,S vaccine, development of drugs that attack specific pathophysiological events is most important. Imbalance of pro- and anti-inflammatory [124], microvascular obstruction by parasitized RBCs (pRBCs) [125], immune activation of endothelial cells and their dysregulation [126] and breakage of blood-brain barrier [127] have been reported to be involved in the pathophysiology of CM. However, the processes that cause these changes and how these changes are coupled to give rise to cerebral symptoms during Malaria are still unidentified to a large extent. Understanding these process

could become the basis for adjuvant therapies and finding of new biomarkers for diagnostic of disease progression [33].

The jury is still out on the primary cause of CM. There are two prominent schools of thought about ascertaining the main reason behind coma and CM [128]:

1) School of sequestration: The level of pRBC sequestration and vascular congestion correlates with disease severity; pRBCs with impaired cytoadherence causes protection against CM [129]; and adjuvant therapies based on cytokine activation are not effective [130].

2) School of cytokines: *Plasmodium vivax* does not cause pRBC sequestration, however it causes endothelial activation and CM [131]; Pro-inflammatory TNF correlates with disease severity and is the main cytokine involved in CM [132].

The research on CM so far is not conclusive in finding the primary factor that leads to the development of CM, one of the above two hypotheses may be true or it may also be a combination of the two.

6.2 Aim of the chapter

In this chapter, I focus on differentiating the severity of disease development between the WT and KO strains. An experiment was carried out to measure features that are considered to be signatures of immune activation in the brain and the spleen of mice (see subsection 2.2.3). Here, by considering individual mouse behaviour and using model-based machine learning technique, I find a subset of salient features from the measured features that are sufficient to distinguish ECM mice from the non-ECM mice, irrespective of the route of infection (via intravenous injection of sporozoites or injection of iRBCs). From this analysis I thereby conclude the processes that may underlay ECM development.

6.3 Method

6.3.1 Data pre-processing

The data recorded in the experiment described in Subsection 2.2.3 form the features, predictors or covariates; hereby referred to as features for the learning algorithm. The feature matrix is represented a X in which each column represents a measured variable (m = 16) and each row represents the measurements from a particular mouse (n = 60). A dependant variable named "disease", denoted by a vector Y, is added to this dataset. The entries of Y, also known as the class variable, are filled with a class '1' if the mouse was observed to have developed ECM and with a class '0' if the mouse did not develop any cerebral symptoms.

$$X = \begin{bmatrix} x_{11} & x_{12} & \dots & x_{1m} \\ \vdots & \vdots & \vdots & \vdots \\ x_{n1} & x_{n1} & \dots & x_{nm} \end{bmatrix}$$

$$Y = \begin{bmatrix} y_1 \\ y_2 \\ \vdots \\ y_n \end{bmatrix}$$

6.3.2 Feature selection using correlation analysis

On the basis of the hypothesis [133] that a good feature subset is one that contains features highly correlated with the class yet uncorrelated with each other, a correlation analysis is done on the feature set. In the first step, Pearson correlation coefficient (PCC) is calculated for each of the feature paired with the dependant variable "disease" to find which features are highly correlated to the dependant or class variable. Only features that have $|\text{PCC}| \geq 0.4$ are considered in the next step of feature selection. In the second step, a feature set is chosen such that it contains features that are uncorrelated to each other. As the feature N_B^{IFN} has the

TABLE 6.1 All the features in the dataset and their meaning.

Feature name	Description
N_B^{CD4}	Number of CD4$^+$ T cells isolated from the brain
N_S^{CD4}	Number of CD4$^+$ T cells isolated from the spleen
N_B^{CD8}	Number of CD8$^+$ T cells isolated from the brain
N_S^{CD8}	Number of CD8$^+$ T cells isolated from the spleen
N_B^{LYM}	Number of lymphocytes isolated from the brain
N_S^{LYM}	Number of lymphocytes isolated from the spleen
N_B^{IFN}	Number of Pb1-specific IFN-γ^+ CD8$^+$ T cells in brain
N_S^{IFN}	Number of Pb1-specific IFN-γ^+ CD8$^+$ T cells in spleen
P_B^{CD4}	Proportion (%) of CD4$^+$ T in lymphocytes isolated from the brain
P_S^{CD4}	Proportion (%) of CD4$^+$ T in lymphocytes isolated from the spleen
P_B^{CD8}	Proportion (%) of CD8$^+$ T in lymphocytes isolated from the brain
P_S^{CD8}	Proportion (%) of CD8$^+$ T in lymphocytes isolated from the spleen
P_B^{LYM}	Proportion (%) of lymphocytes in WBCs isolated from the brain
P_S^{LYM}	Proportion (%) of lymphocytes in WBCs isolated from the spleen
P_B^{IFN}	Proportion (%) of Pb1-specific IFN-γ^+ CD8$^+$ T cells in brain
P_S^{IFN}	Proportion (%) of Pb1-specific IFN-γ^+ CD8$^+$ T cells in spleen

highest PCC in Table 6.2, we assume that this feature is most likely to be a relevant feature in predicting the output class variable. Keeping this in the feature set, other features are added one by one to the final set ensuring that they have $|PCC| \leq 0.7$. Following this criterion, we do not add the features P_B^{IFN} (PCC = 0.8 with N_B^{IFN}), P_S^{IFN} (PCC = 0.72 with N_B^{IFN}), P_B^{CD8} (PCC = 0.71 with N_B^{IFN}) to the final analysis because of their strong correlation with the feature N_B^{IFN}. Many studies have implicated CD8$^+$ T cells more commonly than CD4$^+$ T cells in the pathogenesis of ECM [33,134–137]. Therefore, out of the other strongly correlated pair

TABLE 6.2 Pearson correlation coefficient between individual features and the class variable.

The value 1 denotes total positive linear correlation, 0 is no linear correlation, and −1 stands for total negative linear correlation.

Feature name	PCC with class variable
N_B^{CD4}	0.50
N_S^{CD4}	−0.09
N_B^{CD8}	0.52
N_S^{CD8}	−0.19
N_B^{LYM}	0.16
N_S^{LYM}	0.05
N_B^{IFN}	0.61
N_S^{IFN}	0.19
P_B^{CD4}	0.33
P_S^{CD4}	−0.40
P_B^{CD8}	0.49
P_S^{CD8}	−0.56
P_B^{LYM}	−0.15
P_S^{LYM}	−0.32
P_B^{IFN}	0.41
P_S^{IFN}	0.48

of P_S^{CD8} and P_S^{CD4} (PCC $= 0.88$), only one feature namely P_S^{CD8} is added to the final feature set. As a result, by selecting a feature subset that contains features that are relevant to the dependant variable and also non-redundant [133, 138], size of the feature space of 16 features (as measured in the experiment) is reduced to only 5. Any observation that has a missing data-point or data-points is also dropped from
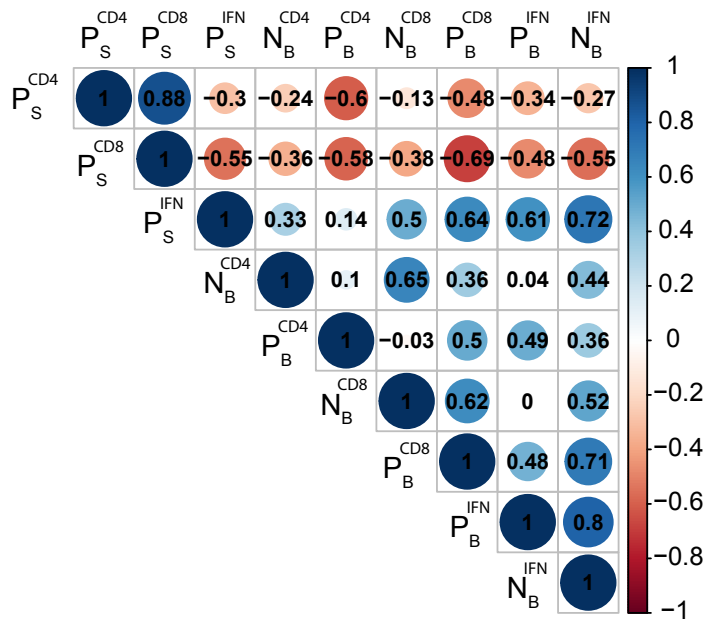
FIGURE 6.1 Pearson correlations coefficients within pairs of features
Spheres colored in shades of red denote negative correlation, spheres colored in shades of blue denote negative correlation and their sizes denote the magnitude of correlation.

the dataset. Thus we are left with 47 observations of 5 features each. To begin with, all features are standardized to have zero mean and unit standard deviation. In doing so, it is ensured that all features are treated equally in the learning process irrespective of their absolute range.

6.3.3 Model selection using cross validation and regularization

The search for optimal regularization parameter and model selection is described in the following steps:

- **Step 1:** The data is randomly partitioned into a training set (80%) and a testing set (20%).
- **Step 2:** A 5-fold cross validation is applied on the training dataset that yields the best model and the best value for λ on the basis of produces the minimum squared error (MSE).
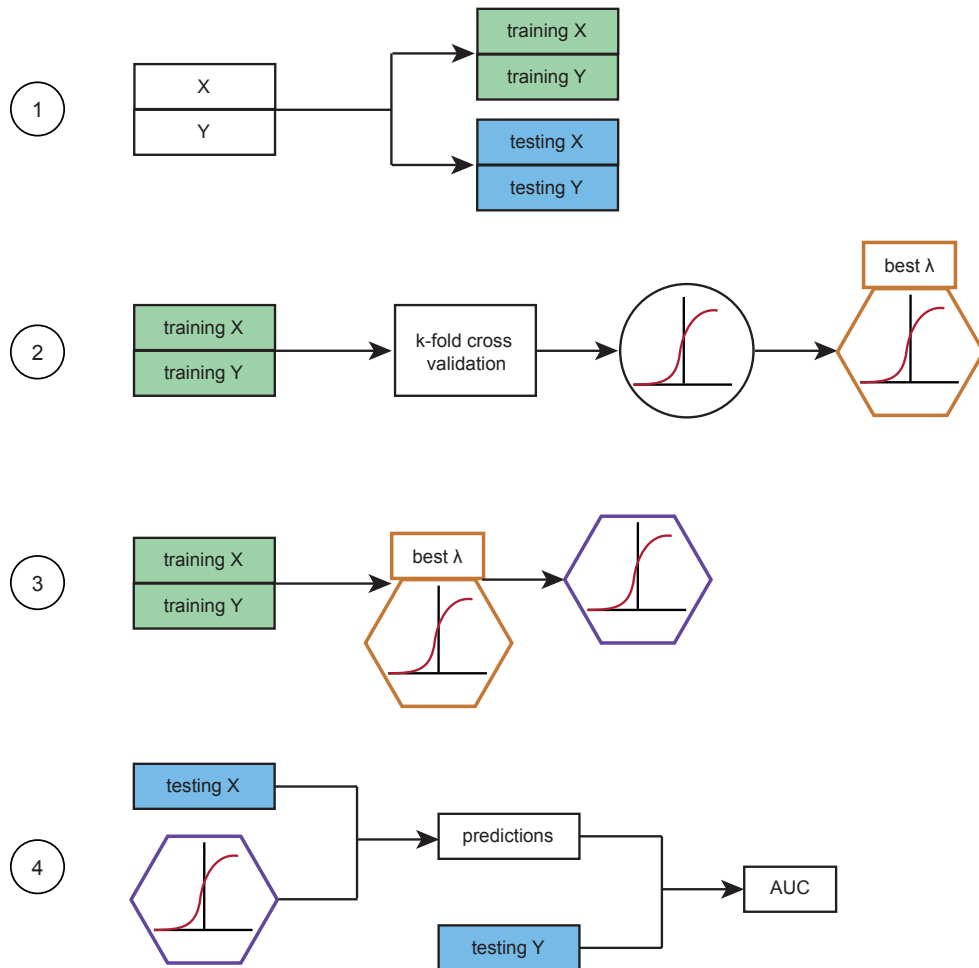
FIGURE 6.2 Schematic showing the 4 steps of learning from the dataset and validating the learned model

In the first step, data is split into a training set and a testing set. In the second step, the best model and the optimum value for hyper-parameter λ is selected using a k-fold cross validation. This model is then parameterized using the full training set. The trained model is then validated by evaluating model performance on the testing set using AUC as the criterion. This schematic is a derivative of a figure by Sebastian Raschka licensed under Creative Commons Attribution 4.0 International License.

- **Step 3:** Taking the best value for λ (from Step 2), the complete training dataset is used to generate the final model.
- **Step 4:** The final model is then validated against the testing dataset that was set aside in the first step and various performance metrics are calculated. See Fig. 6.2

6.4 Results

With the objective of finding the most relevant features of the dataset that are sufficient to classify the mice into the ones that develop ECM and the ones that do not via logistic regression and machine learning, the steps explained in section 6.3.3 were implemented. The steps were repeated 5000 times so that learning takes place on various combinations of training and testing data-sets, the best model as an output of each run was logged. Out of these 5000 best models, the model that appeared most frequently in the log as the best in that run was considered as the final best model and comparisons were made to two of the next frequently appearing models to assure that the learning was indeed unbiased and that it lead to a global best model.

TABLE 6.3 Models and the features selected most frequently

Features in the models A (selected most frequently), B (selected second most frequently) and C (selected third most frequently) in 5000 runs.

Model	Feature 1	Feature 2	Feature 3	Feature 4
A	N_B^{IFN}	P_S^{CD8}	N_B^{CD8}	-
B	N_B^{IFN}	P_S^{CD8}	N_B^{CD8}	N_B^{CD4}
C	N_B^{IFN}	P_S^{CD8}	N_B^{CD4}	-

The three most frequently selected models are listed in Table6.3. The features N_B^{IFN} and P_S^{CD8} emerge as relevant features in all the three models. Evidently, the ROC and AUC of these models also exhibit that these models as classifiers are capable in distinguishing the ECM mice from the non-ECM mice (see Fig. 6.3). The model C shows a lower AUC than the models A and B, whereas the ROC curves
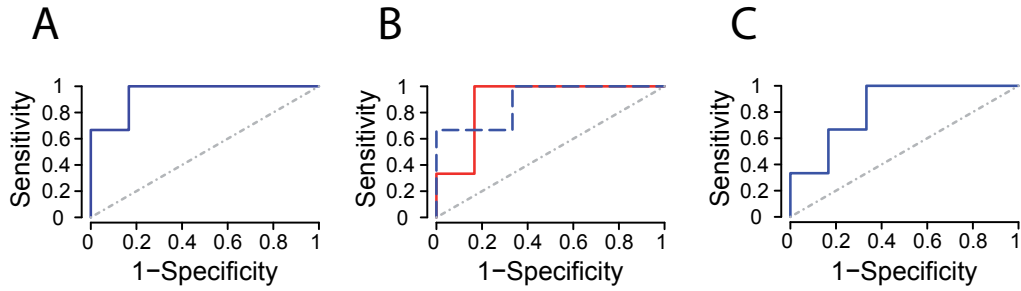
FIGURE 6.3 Best receiver operator characteristics (ROC) of the various models **(A)**. model A (AUC = 0.94), **(B)**. model B (AUC = 0.89) and **(C)**. model C (AUC = 0.83).

TABLE 6.4 Features and their frequency of being selected as relevant features

Features and their frequency of being selected as relevant features across all the 5000 models for various training data and testing data combinations.

Selected feature	frequency of appearing as relevant feature
N_B^{IFN}	99.6 %
P_S^{CD8}	96.1 %
N_B^{CD8}	72.4 %
N_B^{CD4}	70.1 %
Rest of the features	< 20 %

of model A and model B are quite comparable (see Fig. 6.3). However, model A, being the parsimonious of the two models, is selected as the best performing model. The coefficients of features estimated by fitting a logistic regression model with a regularization parameter $\lambda = 0.13$ to the entire dataset are shown in Table 6.5.

The probability of developing ECM given the three features (see Table 6.5) selected by model A is plotted against the model output (z, as seen in Eq. (2.2)) for the data from all the six groups of mice (two uninfected control groups sporozoite or iRBC injected, two KO infected groups sporozoite or iRBC injected, and two WT infected groups sporozoite or iRBC injected injected) calculated using the
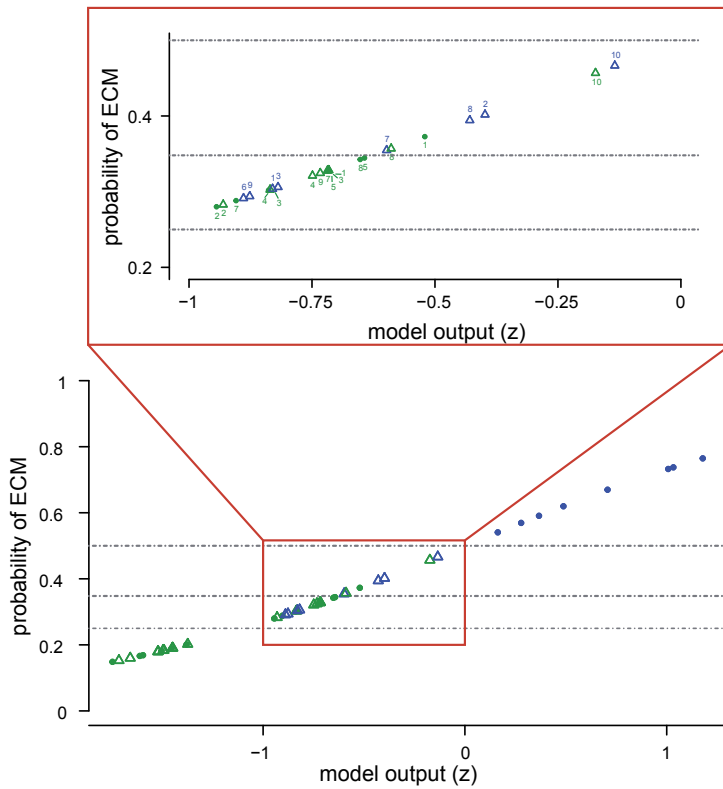
FIGURE 6.4 Output of the classifier

Triangles denote data from mice that were infected via sporozoites, circles denote data from mice that were infected via iRBCs. Data from mice that were observed to have developed ECM are coloured in green, and the ones that didn't are in blue. The three horizontal lines are the three decision thresholds. Inset shows a zoomed version of the classifier output for data that yielded model output $-1 < z < 0$. The numbers on top or bottom represent mouse IDs for WT or KO respectively.

TABLE 6.5 Features selected and output of the fitted lasso regularalized logistic regression model.

Selected feature	coefficient
N_B^{IFN}	1.09
N_B^{CD8}	0.53
P_S^{CD8}	-1.35
Intercept	-1.04

estimated coefficients in Table 6.5 in Fig. 6.4. An ideal classifier output would have shown a definite separation between the two groups being classified (here, it would have meant the green and blue data-points in Fig. 6.4 being separated on the curve with no overlaps). Instead, the plot shows three obviously distinct regions in the classifier output. The region $z \leq -1$ is populated by the model output for data from both the control groups, all of which are rightly classified as non-infected by the classifier. The region on the other extreme, $z \geq 0$ contains model output for mice that were infected by WT iRBCs and are correctly classified as ECM developing. However the region $-1 < z < 0$ that is occupied by mice infected by WT sporozoites or KO sporozoites or KO iRBCs shows a lot of misclassification. The decision threshold (τ) or the criterion to convert the probability of ECM which is the outcome of logistic regression into actual class namely ECM or non-ECM depends highly on the data used for learning (see Eq: (6.1)).

$$\hat{y}_i = \begin{cases} 1 \text{ (ECM)}; & \text{for } p(y_i = 1 | x_i) \geq \tau \\ 0 \text{ (non-ECM)}; & \text{for } p(y_i = 1 | x_i) < \tau \end{cases} \tag{6.1}$$

TABLE 6.6 Decision threshold and its impact on performance of the classifier

Decision threshold (τ)	Accuracy (ACC)	Sensitivity (SEN)	Specificity ($SPEC$)
0.5	83 %	50 %	100 %
0.25	70 %	100 %	45 %
0.35	85 %	75 %	90 %

TABLE 6.7 Table showing confusion matrix for model A with $\tau = 0.35$

		Predicted		
		ECM	No ECM	Total
Actual	ECM	12	4	16
	No ECM	3	28	31
	Total	15	32	47

In this case, the data is imbalanced, meaning that there are more cases of one class (non-ECM mice) than that of the other class (ECM mice). When the class sizes are not equal, the derived classifier favors the larger class [61]. This can be seen in Fig. 6.4, if τ is set to 0.5, all of the members of the non-ECM class, the larger of the two classes, are rightly classified. As discussed earlier the choice of opting a better sensitivity over specificity or vice-versa or opting for acceptable levels of both is governed the objective of the classifier in that particular real-life application. Here the aim is to develop a classifier that is adequately sensitive in detecting the "1" or "positive" class as well as adequately specific in detecting the "0" or "negative" class [61]. A number of decision thresholds (τ) were tested with the global best model and the classifier performance terms of accuracy, sensitivity and specificity were compared for each threshold. A value of $\tau = 0.35$ lead to the best performing classifier (see Table 6.6 and 6.7)

6.5 Discussion

In this chapter, I take a machine learning approach to determine the processes that may contribute to cerebral inflammation, a severe outcome of some of the Malarial infections. In the experiment described in Subsection 2.2.3, a number of indicators of immune activation and immune migration to the brain were measured. Here, I used the measured data to find a subset of these indicators that are adequate in predicting if a mouse from the experiment developed ECM or not. A classifier based on logistic regression was trained on the data and of all the 16 measured indicators of immune activity in the spleen and brain 3 variables; namely 1) the number of $CD8^+$ T cells isolated from the brain, 2) the proportion of $CD8^+$ T

cells in lymphocytes isolated from the spleen and 3) the number of Pb1-specific IFN-γ^+ CD8$^+$ T cells in the brain emerge as the most significant characteristics that can distinguish a mouse with ECM from a mouse without ECM.

The liver-stage followed by the blood-stage of *Plasmodium* infection cause two separate (one by each stage) innate immune responses to counter parasite replication and subsequent spread of the disease. The parasites are sequestered in blood vessels leading to a reduced blood flow thereby restricting the delivery of oxygen and nutrients to the brain and other organs. In addition to this, the accumulated parasitized RBCs lead to endothelial activation thereby increasing the binding ability of the endothelial cells. The activated endothelium becomes a site of further accumulation of leukocytes and RBCs. Upon reaching there, the leukocytes themselves secrete cytokines and chemokines that promote even more recruitment of inflammatory cells. Such an onslaught of inflammatory cells leads to a permeable endothelial wall and the blood-brain barrier is disrupted. The pro-inflammatory cells now have access to the brain and start the same feedforward loop of more recruitment and inflammation in the brain. A detailed understanding of the exact molecular processes underlying development of ECM is still lacking as to which of the leukocytes play a pivotal role and which chemokines or cytokines are directly involved in causing the neuropathology [33].

It has been observed that dendritic cell (DC) primed CD8$^+$ T cells in the spleen peak around 4 day post infection in mice infected with *Plasmodium berghei* ANKA and show a decrease in their proportion probably because of migration to the brain around 7 day post infection, the day when the onset of cerebral inflammation takes place [139]. This coincides with our conclusion that a change in the proportion of CD8$^+$ T cells around the day when mice infected with WT strain showed acute ECM symptoms is an important indicator (P_S^{CD8} appears as a significant feature in models A,B and C) of ECM development. The proportion of CD8$^+$ T cells is drastically reduced in the mice infected via WT iRBCs as compared to the control uninfected mice and the mice infected via KO iRBCs. However, this proportion is comparable between the mice infected with KO sporozoites or WT sporozoites, even though both the groups show a reduced proportion as compared to the control mice. CD8$^+$ T cells have been implicated in many studies in cerebral immunopathalogy [33, 135–137]. After reaching the brain, cytotoxic CD8$^+$ T cells

are exposed to parasite antigens cross-presented by the activated endothelial cells, thereby contributing to heightened inflammation and further disruption of blood-brain barrier. The number of $CD8^+$ T cells isolated from the brain therefore is another significant feature of our classifier. Not just the best model (model A in Table 6.3), but also the second in rank of all the models (model B in Table 6.3) implicates the presence of $CD8^+$ T cells in the brain. In the model C, the feature N_B^{CD8} is replaced by N_B^{CD4} which is an artefact of random partitioning of data into test and train sets and some combinations of data points in the learning or train set can lead to an inference that N_B^{CD4} is also an important factor in ECM. Given the fact that N_B^{CD8} and N_B^{CD4} are correlated in the data, the algorithm sometimes chooses one over the other or both as in the case of model C. The last and the most significant feature in all the three classifiers A, B, and C is the number of $CD8^+$ T cells isolated from brain that respond to Pb1 stimulation. There is ample evidence in various studies [140–142] that not just the availability of $CD8^+$ T cells but the existence of Malaria specific $CD8^+$ IFN-γ^+ T cells contributes to ECM outcome. In fact Shaw et al in [143] found that there were comparable numbers of $CD8^+$ T cells sequestered in the brains of mice infected with ECM causing strain and non ECM causing strain. They recorded that these two groups however differed in the secondary activation of $CD8^+$ T cells in brain to parasite specific antigen stimulus. The interaction of the infiltrating $CD8^+$ T cells with specific antigens is distinct in ECM as compared to non ECM infection. Thus it is only logical that N_B^{IFN} emerges as a feature of prime significance in our proposed classifier.

Although the classifier proposed here performs with a 100% accuracy in classifying the mice in two control groups, KO-iRBC infected into non-ECM class and WT -iRBC into ECM class, a sizeable proportion of KO-sporozoite infected and WT-sporozoite infected groups remain misclassified. This shortcoming of the classifier can be attributed to 1). noise in the data or 2). to another ECM contributing factor that has been overlooked in the experiment. It is quite unlikely that the measurements are noisy given the fact that mice with IDs 1,3,6 and 9 in the WT-sporozite infected, mice with IDs 8 and 10 in the KO-sporozoite and mouse with ID 1 in the KO-iRBC infected behave differently to the majority of their group members but still have a behaviour common to other outlying members of their own group. Assuming that there is indeed a contributing factor that the classifier

fails to consider, I searched for conclusions drawn in other experimental studies to justify this assumption.

As discussed before, it is the secondary activation of CD8$^+$ T cells (that infiltrated the brain following priming in the spleen) that is a major cause of inflammation in the brain. The secondary activation is in response to the cross- presentation of antigens by iRBCs sequestered in the brain. Therefore, apart from the pro-inflammatory CD8$^+$ T cells causing damage in the brain, the accessibility of parasite material to these cells must also be the driving force behind the extent of damage [142, 143]. It is known that peripheral parasitemia is closely correlated to the magnitude of iRBCs sequestered in the brain vessels [58, 144]. Similarly, parasite strains causing ECM cause a heightened level of parasitezed RBCs in brains of mice as compared to the non-ECM causing strains [144]. Hence, even though WT or KO sporozoite infected mice show comparable levels of CD8$^+$ T cell infiltration and the isolated CD8$^+$ T cells show similar response to Pb1 stimulus, the KO sporozoite infected mice have in fact lower peripheral parasitemia levels, that correspond to lower parasite material sequestered in the brain leading to a diminished stimulus to the CD8$^+$ T cells in brain. This explains the less severe disease outcome in KO sporozoite infected mice and serious cerebral implications in WT sporozoite infected mice. In summary our analysis backs the claim that it is not one of the two hypotheses of ECM immunopathogenesis namely vascular occlusion and inflammation [128], but an intricate combination of both the hypotheses, the peak peripheral parasitemia, the obstruction of the vascular system by parasitized RBCs, change in the CD8$^+$ T cell proportion in the spleen, migration of primed CD8$^+$ T cells to the brain, the degree of CD8$^+$ IFN-γ^+ T cell response to the antigen Pb1, is responsible as a whole for cerebral inflammation during *Plasmodium berghei* ANKA infection in mice.

6.6 Conclusion

This study proposes an ECM pathogenesis hypothesis on a macro level. The proposed hypothesis is based on finding certain characteristics of immune activation and immune migration to the brain that are specific to the parasite strain (ECM or non-ECM causing). It also brings to home the point that route of infection is

not the deciding factor for disease outcome, meaning WT infection leads to ECM and KO infection does not irrespective of the route of infection. However, the triggered immune response and the consequent inflammation in the brain is specific to route of infection. The data showed the highest immune responses being triggered during WT infection when the liver-stage was bypassed, and the least during KO infection via iRBCs, the latter one being the most unnatural route. The responses were comparable when both liver-stage and blood-stage were executed for WT and KO infections, which also lead to a less accurate classifier for these two groups. These comparable groups can still be classified into ECM and non ECM classes, if the feature space is extended to include one of the indicators of parasitemia be it peripheral parasitemia or the extent of iRBC infiltration in the brain. To sum it all up, our work is another proof to the idea that it is the combined effect of parasite sequestration in the brain and the level of pro-inflammatory cells in the brain that contributes to ECM development.

CHAPTER 7

General discussion

The overall objective of this thesis was to understand within-host infection dynamics of Malaria and finding factors that decide the fate of disease severity. Mechanistic within-host models that describe progression of infection at various stages of the parasite life-cycle were developed. Through these models, the infection parameters of *Pb*ANKA (WT) and *PbmaLS_05*(-) (KO) strains were distinguished leading to conclusions about the potential role of *PbmaLS_05* in cerebral Malaria.

While modeling the blood-stage infection dynamics of Malaria, it was discovered that Malaria induced change in erythropoiesis is a characteristic of early infection, even before substantial loss of RBCs to parasite invasion has occurred. This altered erythropoietic dynamics is a major contributor to reduction in reticulocyte population. This finding is corroborated by other studies [19, 78, 145], that report disease induced suppression of RBC production, although in [19] it is observed only during the later phase of infection. The blood-stage infection dynamics model revealed that lower parasitemia observed during KO infection is attributed to its lower average infectivity than the WT strain. In addition to this, it was found that similar to other more infectious *Plasmodium* strains [12,15,16,19], the *Pb*ANKA (WT) strain infects the reticulocytes with a higher rate of infection than it infects the normocytes. On further analysis that was based on testing various hypotheses using the model and including the data from the PHZ experiment, I concluded that the KO strain displays little or no preference for infecting reticulocytes as compared to the normocytes. Thus, *PbmaLS_05* potentially plays a role in infecting reticulocytes and its deletion results in reduced parasitemia, which

eventually causes only severe anemia and not experimental cerebral Malaria.

In addition to rate of infection and reticulocyte preference, it was also explored if other characteristics of Malaria blood-stage infection, like reduced merozoite production or altered maturation times for infected RBCs could explain the reduced parasitemia in KO infected mice. This indicated that a maturation time that is approximately twice as long than the WT-iRBC could be a possible reason for the observed KO infection dynamics. This supports the conclusion that deletion of *PbmaLS_05* particularly leads to impaired parasite development and less successful infections in reticulocytes during the initial blood-stage phase.

With the combination of experimental data and within-host model, only a comparative study between the infection dynamics of the two strains was possible. The next step can be to determine absolute values of their infection rates and reticulocyte preferences. A similar blood-stage infection experiment that records changes in the blood plasma concentration and proportion of infected reticulocytes, in addition to total RBC proportion, proportion of reticulocytes and proportion of infected reticulocytes, will enhance the analysis further. Similarly, more complex models that can test various hypotheses like changing reticulocyte preference over time and preference for a particular age of RBCs, not restricting to classifying RBCs into reticulocytes and normocytes can be developed and used to further characterize *PbmaLS_05*.

The investigation of early blood-stage Malaria infection dynamics established that knocking out the *PbmaLS_05* renders the KO strain weaker in productive infection and severe disease progression in comparison to the WT strain. This lead to the next natural question, how would such a weakness manifest itself during the liver stage. It was observed that the KO sporozoites when used to infect mice showed a slight developmental delay while maturing and multiplying in the liver [13]. Many studies have reported that *Plasmodium* development inside the host liver is coupled with the availability of nutrition to the parasite [24, 27, 102] and nutritional status of the host [25, 26]. *PbmaLS_05* is known to localize to the apicoplast [13], the organelle that contributes towards metabolite synthesis [118]. Thus, a proof-of-concept study that quantified the impact of host nutritional status on the development of *Plasmodium* during Malaria infection was done. This analysis was further used to develop an experimental protocol that could be used

to:

1) Magnify the developmental delay (if any) in the KO sporozoites, by observing WT and KO infection dynamics in pre-starved hosts.

2) Characterize the role of *PbmaLS_05* gene more precisely during the pre-erythrocytic liver-stage.

A detailed understanding of how extent of peripheral parasitemia and the triggered immune responses during the progression of Malaria through various within-host stages is still not available [33]. A comparison of immune activation and immune response data from the KO (non-ECM causing) or WT (ECM causing) infected mice resulted in selecting major contributors to cerebral Malaria. The classifier based method revealed that the number of $CD8^+$ T cells in the brain was the most significant indicator for the development of cerebral Malaria in mice. Studies have highlighted that $CD8^+$ T cells found in the brain during the infection are indeed responsible for cerebral immunopathology [139]. Additionally, *Pb*ANKA WT infection is known to cause a peak in the proportion of $CD8^+$ T cells in leukocytes in the spleen, followed by a drastic reduction in the proportion around the day when infected mice show ECM symptoms [33, 135–137]. Likewise, the comparative analysis done here, also suggests the proportion of $CD8^+$ T cells in the spleen as the next important player in causing cerebral Malaria. Along with these two, it was found here that not just the availability of $CD8^+$ T cells in the brain but also the presence of Malaria specific $CD8^+$ IFN-γ^+ T cells produces cerebral symptoms [140–142]. Notably, the limitation of this method in distinguishing some mice from the other displayed that the measured signatures of immune response and immune activation were not sufficient in predicting the disease outcome for a given mouse. However, this missing link can be guessed with a very high probability from the analysis. The $CD8^+$ T cells, that infiltrated the brain after priming in the spleen, undergo secondary activation in the presence of antigens cross-presented by iRBCs sequestered in the brain [58, 142–144]. Thus, assuming that the number of iRBCs sequestered in the brain are proportional to peripheral parasitemia, the extent of parasitemia in the blood must definitely be a major indicator of ECM.

All of these four factors perfectly justify why *Pb*ANKA WT infected mice, via

sporozoites or iRBCs developed ECM, whereas the *Pb*maLS_05 (-) KO infected mice via sporozoites or iRBCs did not develop ECM, in-spite of the KO-sporozoite infected mice showing comparable levels of immune response to that of the WT. Thus, bringing home the point that *Pb*maLS_05 may not have an important role to play in triggered immune response during the liver-stage of Malaria. However, its absence may lead to a small developmental delay during the liver-stage, which must be further investigated. Besides this, it is evident from the analysis that during the blood-stage *Pb*maLS_05 contributes in reticulocyte invasion/infection, and knocking it out makes the parasite non-specific to the age of its target red blood cell. I propose that the *Pb*maLS_05 (-) mutant parasite strain can serve as a tool to study how the preference of parasites to infect particular RBC influences both disease progression and the development of experimental cerebral Malaria. This will ultimately aid in discovering the factors that influence the activation of immune responses and that might contribute to efficient parasite control.

Appendices

CHAPTER A

Additional Material to Chapter 3
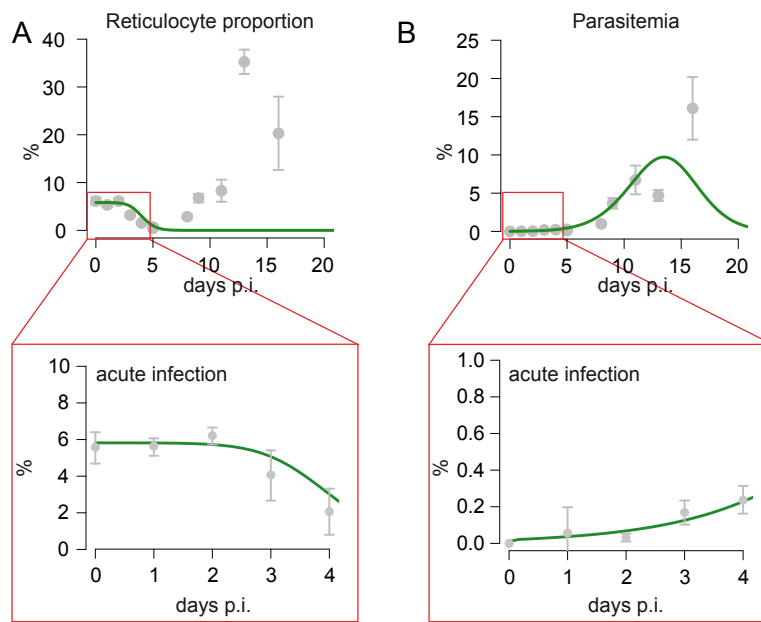
FIGURE A.1 Long-term dynamics of the KO-parasite strain followed for 20days post infection when mice develop anemia

The data for the reticulocyte proportion (A) and the parasitemia (B) is shown in grey. The green line indicates the prediction of the mathematical model for the KO infection parameters when fitted to the acute infection dynamics (day 0-4 p.i., lower panels). The model is incapable in explaining the observed increase in reticulocyte proportion and parasitemia at later days of infection. This indicates a potential change in the assumed processes regulating erythropoiesis during the later phase of blood-stage infection.

CHAPTER B

Additional Material to Chapter 5
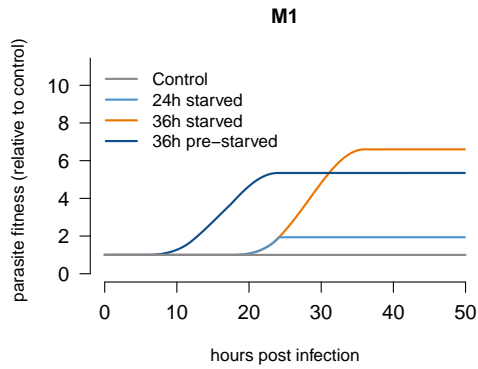
FIGURE B.1 Parasite fitness $P(t)$ as predicted for the three starvation groups relative to control, with the mathematical model M1 for liver-stage development.
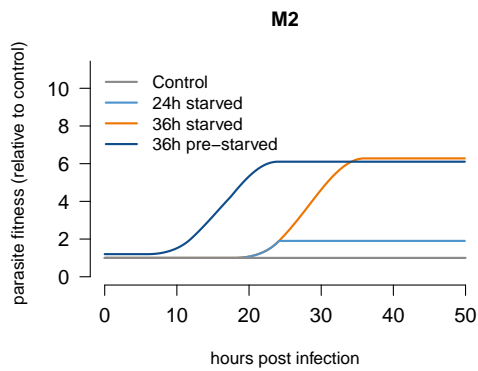
FIGURE B.2 Parasite fitness $P(t)$ as predicted for the three starvation groups relative to control, with the mathematical model M2 for liver-stage development.

CHAPTER C

Additional Material to Chapter 6
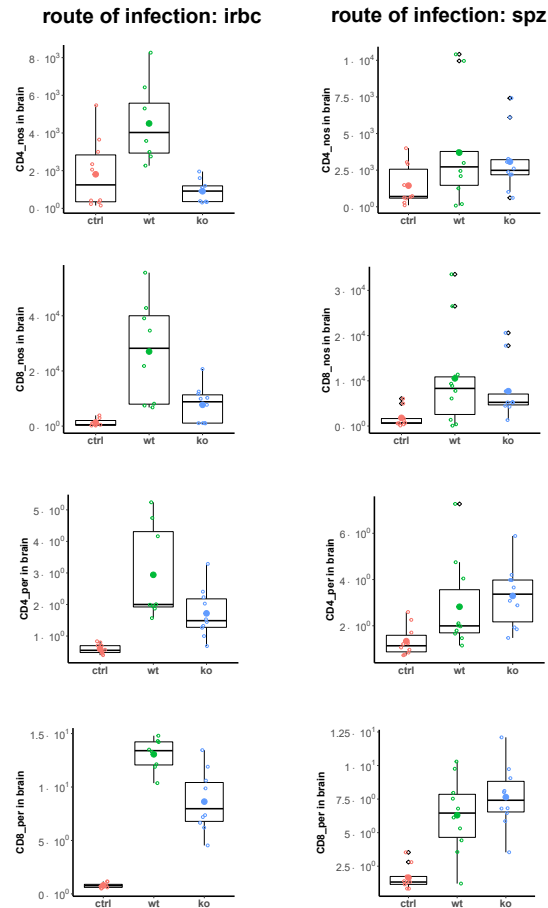
FIGURE C.1 Immune status data I

The left panel shows data from mice infected with iRBC injections, and the right panel shows data from mice infected with sporozoites. The colors indicate the three groups, namely red: control, blue: KO and green: WT. The boxplot corresponds to the first and third quartiles and the median. It is evident that there is no single factor that is decisive indicator of ECM in mice. A detailed analysis revealed that it is a linear combination of CD8$^+$ T cells found in the brain, the proportion of CD8$^+$ T cells in the spleen and the presence of Malaria specific CD8$^+$ IFN-γ^+ T, that are major indicators of ECM.
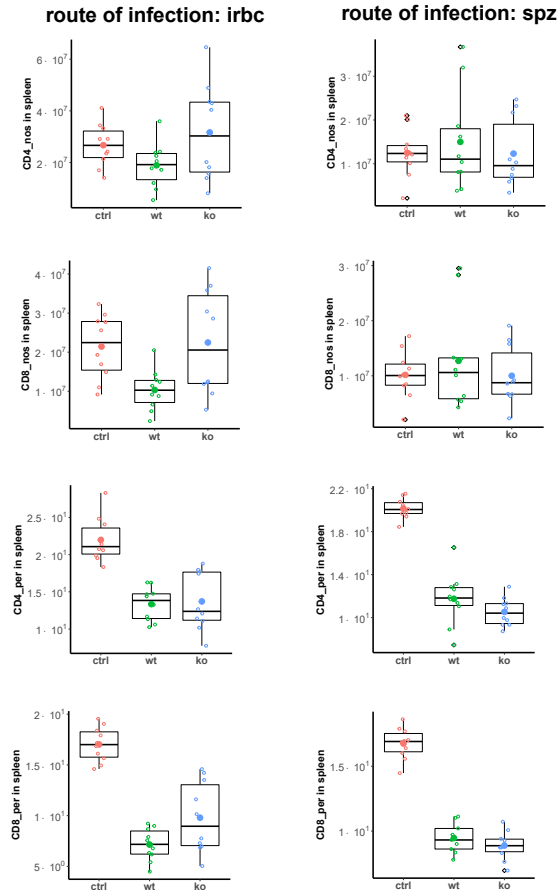
FIGURE C.2 Immune status data II

The left panel shows data from mice infected with iRBC injections, and the right panel shows data from mice infected with sporozoites. The colors indicate the three groups, namely red: control, blue: KO and green: WT. The boxplot corresponds to the first and third quartiles and the median. It is evident that there is no single factor that is decisive indicator of ECM in mice. A detailed analysis revealed that it is a linear combination of CD8$^+$ T cells found in the brain, the proportion of CD8$^+$ T cells in the spleen and the presence of Malaria specific CD8$^+$ IFN-γ^+ T, that are major indicators of ECM.
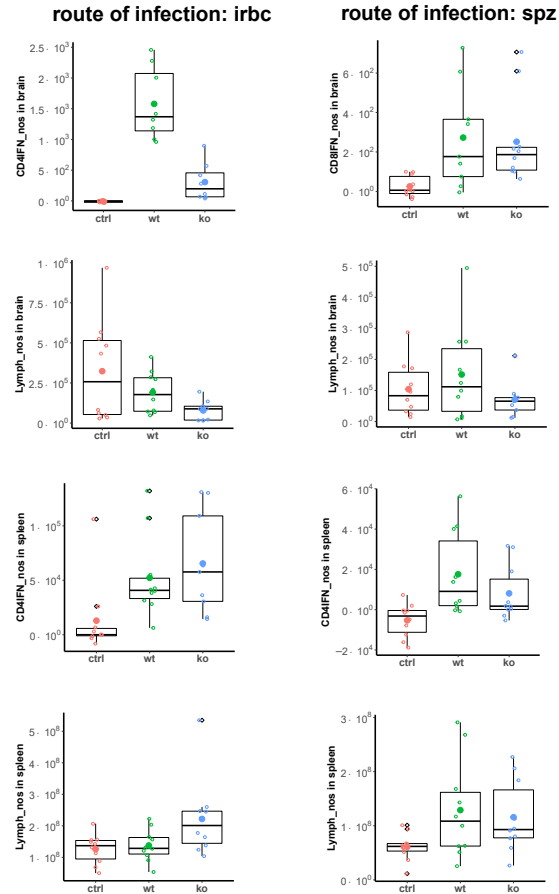
FIGURE C.3 Immune status data III

The left panel shows data from mice infected with iRBC injections, and the right panel shows data from mice infected with sporozoites. The colors indicate the three groups, namely red: control, blue: KO and green: WT. The boxplot corresponds to the first and third quartiles and the median. It is evident that there is no single factor that is decisive indicator of ECM in mice. A detailed analysis revealed that it is a linear combination of $CD8^+$ T cells found in the brain, the proportion of $CD8^+$ T cells in the spleen and the presence of Malaria specific $CD8^+$ IFN-γ^+ T, that are major indicators of ECM.

Bibliography

[1] W. H. Organization, "World malaria report 2017," World Health Organization, Geneva, Tech. Rep., 2017.

[2] R. Idro, K. Marsh, C. C. John, and C. R. Newton, "Cerebral malaria: mechanisms of brain injury and strategies for improved neurocognitive outcome," *Pediatric research*, vol. 68, no. 4, p. 267, 2010.

[3] A. Olotu, G. Fegan, J. Wambua, G. Nyangweso, A. Leach, M. Lievens, D. C. Kaslow, P. Njuguna, K. Marsh, and P. Bejon, "Seven-year efficacy of rts, s/as01 malaria vaccine among young african children," *New England Journal of Medicine*, vol. 374, no. 26, pp. 2519–2529, 2016.

[4] T. Annoura, I. H. Ploemen, B. C. van Schaijk, M. Sajid, M. W. Vos, G.-J. van Gemert, S. Chevalley-Maurel, B. M. Franke-Fayard, C. C. Hermsen, A. Gego *et al.*, "Assessing the adequacy of attenuation of genetically modified malaria parasite vaccine candidates," *Vaccine*, vol. 30, no. 16, pp. 2662–2670, 2012.

[5] R. E. Sinden, "Developing transmission-blocking strategies for malaria control," *PLoS pathogens*, vol. 13, no. 7, p. e1006336, 2017.

[6] E. Tjitra, N. M. Anstey, P. Sugiarto, N. Warikar, E. Kenangalem, M. Karyana, D. A. Lampah, and R. N. Price, "Multidrug-resistant plasmodium vivax associated with severe and fatal malaria: a prospective study in papua, indonesia," *PLoS medicine*, vol. 5, no. 6, p. e128, 2008.

[7] C. Metcalf, G. Long, N. Mideo, J. Forester, O. Bjørnstad, and A. Graham, "Revealing mechanisms underlying variation in malaria virulence: effective propagation and host control of uninfected red blood cell supply," *Journal of The Royal Society Interface*, p. rsif20120340, 2012.

[8] I. Coppens, "Metamorphoses of malaria: the role of autophagy in parasite differentiation," *Essays in biochemistry*, vol. 51, pp. 127–136, 2011.

[9] G. Siciliano and P. Alano, "Enlightening the malaria parasite life cycle: bioluminescent plasmodium in fundamental and applied research," *Frontiers in microbiology*, vol. 6, p. 391, 2015.

[10] A. G. Craig, G. E. Grau, C. Janse, J. W. Kazura, D. Milner, J. W. Barnwell, G. Turner, J. Langhorne *et al.*, "The role of animal models for research on severe malaria," *PLoS pathogens*, vol. 8, no. 2, p. e1002401, 2012.

[11] M. Niikura, S.-I. Inoue, T. Fukutomi, J. Yamagishi, H. Asahi, and F. Kobayashi, "Comparative genomics and proteomic analyses between lethal and nonlethal strains of plasmodium berghei," *Experimental parasitology*, vol. 185, pp. 1–9, 2018.

[12] R. Antia, A. Yates, and J. C. de Roode, "The dynamics of acute malaria infections. i. effect of the parasite's red blood cell preference," *Proc Biol Sci*, vol. 275, no. 1641, pp. 1449–58, 2008.

[13] P. Fernandes, S. Howland, K. Heiss, A. Hoffmann, M. A. Hernandez-Castaneda, K. Vochyanova, R. Frank, P. Wiedemann, M. Bendszus, L. Rénia *et al.*, "A plasmodium cross-stage antigen contributes to the development of experimental cerebral malaria," *Frontiers in Immunology*, vol. 9, p. 1875, 2018.

[14] D. Cromer, J. Stark, and M. P. Davenport, "Low red cell production may protect against severe anemia during a malaria infection—insights from modeling," *Journal of theoretical biology*, vol. 257, no. 4, pp. 533–542, 2009.

[15] B. Mons, "Preferential invasion of malarial merozoites into young red blood cells," *Blood Cells*, vol. 16, no. 2-3, pp. 299–312, 1990. [Online]. Available: http://europepmc.org/abstract/MED/2257316

[16] B. Mons, J. J. Croon, W. van der Star, and H. J. van der Kaay, "Erythrocytic schizogony and invasion of plasmodium vivax in vitro," *Int J Parasitol*, vol. 18, no. 3, pp. 307–11, 1988. [Online]. Available: http://www.ncbi.nlm.nih.gov/pubmed/3294199

[17] R. J. Wilson, G. Pasvol, and D. J. Weatherall, "Invasion and growth of plasmodium falciparum in different types of human erythrocyte," *Bull World Health Organ*, vol. 55, no. 2-3, pp. 179–86, 1977. [Online]. Available: http://www.ncbi.nlm.nih.gov/pubmed/338178

[18] I. Singer, R. Hadfield, and M. Lakonen, "The influence of age on the intensity of infection with plasmodium berghei in the rat," *J Infect Dis*, vol. 97, no. 1, pp. 15–21, 1955.

[19] D. Cromer, K. J. Evans, L. Schofield, and M. P. Davenport, "Preferential invasion of reticulocytes during late-stage plasmodium berghei infection accounts for reduced circulating reticulocyte levels," *Int J Parasitol*, vol. 36, no. 13, pp. 1389–97, 2006. [Online]. Available: http://www.ncbi.nlm.nih.gov/pubmed/16979643

[20] F. E. McKenzie, G. M. Jeffery, and W. E. Collins, "Plasmodium vivax blood-stage dynamics," *Journal of Parasitology*, vol. 88, no. 3, pp. 521–535, 2002.

[21] D. H. Kerlin and M. L. Gatton, "Preferential invasion by plasmodium merozoites and the self-regulation of parasite burden," *PLoS One*, vol. 8, no. 2, p. e57434, 2013.

[22] P. G. McQueen and F. E. McKenzie, "Age-structured red blood cell susceptibility and the dynamics of malaria infections," *Proc Natl Acad Sci U S A*, vol. 101, no. 24, pp. 9161–6, 2004.

[23] B. Jayabalasingham, R. Menard, and D. A. Fidock, "Recent insights into fatty acid acquisition and metabolism in malarial parasites," *F1000 biology reports*, vol. 2, 2010.

[24] C. Agop-Nersesian, L. Niklaus, R. Wacker, and V. Theo Heussler, "Host cell cytosolic immune response during plasmodium liver stage development," *FEMS microbiology reviews*, vol. 42, no. 3, pp. 324–334, 2018.

[25] M.-N. Lombard, R. Bazin, G. Durand, F. Beaugé, D. Baccam, F. Milgen, and I. Landau, "Rodent plasmodium development in livers of genetically obese zucker rats (fa/fa)," *European Journal of Protistology*, vol. 34, no. 1, pp. 78–81, 1998.

[26] M. Prado, N. Eickel, M. D. Niz, A. Heitmann, C. Agop-Nersesian, R. Wacker, J. Schmuckli-Maurer, R. Caldelari, C. J. Janse, S. M. Khan, J. May, C. G. Meyer, and V. T. Heussler, "Long-term live imaging reveals cytosolic immune responses of host hepatocytes against plasmodium infection and parasite escape mechanisms," *Autophagy*, vol. 11, no. 9, pp. 1561–1579, 2015, pMID: 26208778. [Online]. Available: https://doi.org/10.1080/15548627.2015.1067361

[27] C. Thieleke-Matos, M. Lopes da Silva, L. Cabrita-Santos, M. D. Portal, I. P. Rodrigues, V. Zuzarte-Luis, J. S. Ramalho, C. E. Futter, M. M. Mota, D. C. Barral *et al.*, "Host cell autophagy contributes to plasmodium liver development," *Cellular microbiology*, vol. 18, no. 3, pp. 437–450, 2016.

[28] M. J. Shears, C. Y. Botté, and G. I. McFadden, "Fatty acid metabolism in the plasmodium apicoplast: Drugs, doubts and knockouts," *Molecular and biochemical parasitology*, vol. 199, no. 1-2, pp. 34–50, 2015.

[29] C. Bisanz, O. Bastien, D. Grando, J. Jouhet, E. Maréchal, and M.-F. Cesbron-Delauw, "Toxoplasma gondii acyl-lipid metabolism: de novo synthesis from apicoplast-generated fatty acids versus scavenging of host cell precursors," *Biochemical Journal*, vol. 394, no. 1, pp. 197–205, 2006.

[30] S. Mundhra, U. Parmar, and D. Shukla, "A prospective study to identify the co-relation of a disease severity of complicated malaria & clinical outcome," *Paripex-Ind J Res,* vol. 12, no. 4, p. 7, 2016.

[31] A. Dondorp, F. Nosten, K. Stepniewska, N. Day, and N. White, "Artesunate versus quinine for treatment of severe falciparum malaria: a randomised trial." *Lancet (London, England),* vol. 366, no. 9487, pp. 717–725, 2005.

[32] L. Cui, S. Mharakurwa, D. Ndiaye, P. K. Rathod, and P. J. Rosenthal, "Antimalarial drug resistance: literature review and activities and findings of the icemr network," *The American journal of tropical medicine and hygiene,* vol. 93, no. 3_Suppl, pp. 57–68, 2015.

[33] J. Dunst, F. Kamena, and K. Matuschewski, "Cytokines and chemokines in cerebral malaria pathogenesis," *Frontiers in cellular and infection microbiology,* vol. 7, p. 324, 2017.

[34] N. J. White, G. D. Turner, I. M. Medana, A. M. Dondorp, and N. P. Day, "The murine cerebral malaria phenomenon," *Trends in parasitology,* vol. 26, no. 1, pp. 11–15, 2010.

[35] F. E. McKenzie, "Why model malaria?" *Parasitology Today,* vol. 16, no. 12, pp. 511–516, 2000.

[36] R. Ross, "Some a priori pathometric equations," *British medical journal,* vol. 1, no. 2830, p. 546, 1915.

[37] A. M. Dondorp, S. Yeung, L. White, C. Nguon, N. P. Day, D. Socheat, and L. Von Seidlein, "Artemisinin resistance: current status and scenarios for containment," *Nature Reviews Microbiology,* vol. 8, no. 4, p. 272, 2010.

[38] N. J. White, "Antimalarial drug resistance," *The Journal of clinical investigation,* vol. 113, no. 8, pp. 1084–1092, 2004.

[39] M. L. Gatton and Q. Cheng, "Modeling the development of acquired clinical immunity to plasmodium falciparum malaria," *Infection and immunity,* vol. 72, no. 11, pp. 6538–6545, 2004.

[40] K. Dietz, G. RADDATZ, and L. Molineaux, "Mathematical model of the first wave of plasmodium falciparum asexual parasitemia in non-immune and vaccinated individuals," *The American journal of tropical medicine and hygiene*, vol. 75, no. 2_suppl, pp. 46–55, 2006.

[41] R. Anderson, R. May, and S. Gupta, "Non-linear phenomena in host—parasite interactions," *Parasitology*, vol. 99, no. S1, pp. S59–S79, 1989.

[42] D. S. Khoury, D. Cromer, S. E. Best, K. R. James, P. S. Kim, C. R. Engwerda, A. Haque, and M. P. Davenport, "Effect of mature blood-stage plasmodium parasite sequestration on pathogen biomass in mathematical and in vivo models of malaria," *Infection and immunity*, vol. 82, no. 1, pp. 212–220, 2014.

[43] C. Dogovski, S. C. Xie, G. Burgio, J. Bridgford, S. Mok, J. M. McCaw, K. Chotivanich, S. Kenny, N. Gnädig, J. Straimer *et al.*, "Targeting the cell stress response of plasmodium falciparum to overcome artemisinin resistance," *PLoS biology*, vol. 13, no. 4, p. e1002132, 2015.

[44] C. Chiyaka, W. Garira, and S. Dube, "Modelling immune response and drug therapy in human malaria infection," *Computational and Mathematical Methods in Medicine*, vol. 9, no. 2, pp. 143–163, 2008.

[45] M. A. Selemani, L. S. Luboobi, and Y. Nkansah-Gyekye, "The in-human host and in-mosquito dynamics of malaria parasites with immune responses," *New Trends in Mathematical Sciences*, vol. 5, no. 3, pp. 182–207, 2017.

[46] T. O. Orwa, R. W. Mbogo, and L. S. Luboobi, "Mathematical model for hepatocytic-erythrocytic dynamics of malaria," *International Journal of Mathematics and Mathematical Sciences*, vol. 2018, 2018.

[47] Z. Tabo, L. S. Luboobi, and J. Ssebuliba, "Mathematical modelling of the in-host dynamics of malaria and the effects of treatment," *Journal of Mathematics and computer science-JMCS*, vol. 17, no. 1, pp. 1–21, 2017.

[48] M. Prudêncio, M. M. Mota, and A. M. Mendes, "A toolbox to study liver stage malaria," *Trends in parasitology*, vol. 27, no. 12, pp. 565–574, 2011.

[49] T. Davis, S. Krishna, S. Looareesuwan, W. Supanaranond, S. Pukrittayakamee, K. Attatamsoonthorn, and N. J. White, "Erythrocyte sequestration and anemia in severe falciparum malaria. analysis of acute changes in venous hematocrit using a simple mathematical model." *The Journal of clinical investigation*, vol. 86, no. 3, pp. 793–800, 1990.

[50] E. Alpaydin, *Introduction to machine learning*. MIT press, 2009.

[51] M. Poostchi, K. Silamut, R. Maude, S. Jaeger, and G. Thoma, "Image analysis and machine learning for detecting malaria," *Translational Research*, 2018.

[52] S. Mavandadi, S. Dimitrov, S. Feng, F. Yu, U. Sikora, O. Yaglidere, S. Padmanabhan, K. Nielsen, and A. Ozcan, "Distributed medical image analysis and diagnosis through crowd-sourced games: a malaria case study," *PloS one*, vol. 7, no. 5, p. e37245, 2012.

[53] G. Díaz, F. A. González, and E. Romero, "A semi-automatic method for quantification and classification of erythrocytes infected with malaria parasites in microscopic images," *Journal of Biomedical Informatics*, vol. 42, no. 2, pp. 296–307, 2009.

[54] Y. KalantarMotamedi, R. T. Eastman, R. Guha, and A. Bender, "A systematic and prospectively validated approach for identifying synergistic drug combinations against malaria," *Malaria journal*, vol. 17, no. 1, p. 160, 2018.

[55] J. Y. Mary, A. J. Valleron, H. Croizat, and E. Frindel, "Mathematical analysis of bone marrow erythropoiesis: application to c3h mouse data," *Blood Cells*, vol. 6, no. 2, pp. 241–62, 1980.

[56] N. Thakre, P. Fernandes, A.-K. Mueller, and F. Graw, "Examining the reticulocyte preference of two plasmodium berghei strains during blood-stage malaria infection," *Frontiers in Microbiology*, vol. 9, p. 166,

2018. [Online]. Available: https://www.frontiersin.org/article/10.3389/fmicb.2018.00166

[57] B. Franke-Fayard, C. J. Janse, M. Cunha-Rodrigues, J. Ramesar, P. Büscher, I. Que, C. Löwik, P. J. Voshol, M. A. Den Boer, S. G. Van Duinen *et al.*, "Murine malaria parasite sequestration: Cd36 is the major receptor, but cerebral pathology is unlinked to sequestration," *Proceedings of the National Academy of Sciences*, vol. 102, no. 32, pp. 11 468–11 473, 2005.

[58] H. S. W., P. C. Meng, G. S. Yee, C. Carla, M. Benoit, S. Nilabh, G. Florent, G. G. M., and R. Laurent, "Brain microvessel cross-presentation is a hallmark of experimental cerebral malaria," *EMBO Molecular Medicine*, vol. 5, no. 7, pp. 984–999, 2013. [Online]. Available: https://onlinelibrary.wiley.com/doi/abs/10.1002/emmm.201202273

[59] R Core Team, *R: A Language and Environment for Statistical Computing*, R Foundation for Statistical Computing, Vienna, Austria, 2013. [Online]. Available: http://www.R-project.org/

[60] K. Soetaert, T. Petzoldt, and R. W. Setzer, "Solving differential equations in r: Package desolve," *Journal of Statistical Software*, vol. 33, no. 9, pp. 1–25, 2010. [Online]. Available: http://www.jstatsoft.org/v33/i09

[61] J. J. Chen, C. Tsai, H. Moon, H. Ahn, J. J. Young, and C.-h. Chen, "The use of decision threshold adjustment in classification for cancer prediction," 2006.

[62] T. Fawcett, "An introduction to roc analysis," *Pattern recognition letters*, vol. 27, no. 8, pp. 861–874, 2006.

[63] C. Gao, H. Sun, T. Wang, M. Tang, N. I. Bohnen, M. L. Müller, T. Herman, N. Giladi, A. Kalinin, C. Spino *et al.*, "Model-based and model-free machine learning techniques for diagnostic prediction and classification of clinical outcomes in parkinson?s disease," *Scientific reports*, vol. 8, no. 1, p. 7129, 2018.

[64] S. Portugal, H. Drakesmith, and M. M. Mota, "Superinfection in malaria: Plasmodium shows its iron will," *EMBO Rep*, vol. 12, no. 12, pp. 1233–42, 2011. [Online]. Available: http://www.ncbi.nlm.nih.gov/pubmed/22081142

[65] J. S. Richards and J. G. Beeson, "The future for blood-stage vaccines against malaria," *Immunology and cell biology*, vol. 87, no. 5, pp. 377–390, 2009.

[66] A. M. Dondorp, B. J. Angus, K. Chotivanich, K. Silamut, R. Ruangveer-ayuth, M. R. Hardeman, P. A. Kager, J. Vreeken, and N. J. White, "Red blood cell deformability as a predictor of anemia in severe falciparum malaria," *Am J Trop Med Hyg*, vol. 60, no. 5, pp. 733–7, 1999. [Online]. Available: http://www.ncbi.nlm.nih.gov/pubmed/10344643

[67] J. G. Beeson, D. R. Drew, M. J. Boyle, G. Feng, F. J. Fowkes, and J. S. Richards, "Merozoite surface proteins in red blood cell invasion, immunity and vaccines against malaria," *FEMS Microbiol Rev*, vol. 40, no. 3, pp. 343–72, 2016. [Online]. Available: http://www.ncbi.nlm.nih.gov/pubmed/26833236

[68] M. C. Mackey, *Mathematical models of hematopoietic cell replication and control*. New York, NY: Prentice-Hall, 1997, pp. 149–178.

[69] R. M. Bannerman, *Hematology*, 2nd ed., ser. The Mouse in Biomedical Research, Normative Biology, Husbandry, and Models. London, UK: Academic Press, 1983, vol. 3.

[70] A. Ganzoni, R. S. Hillman, and C. A. Finch, "Maturation of the macroreticulocyte," *Br J Haematol*, vol. 16, no. 1, pp. 119–35, 1969. [Online]. Available: http://www.ncbi.nlm.nih.gov/pubmed/5795203

[71] G. Gronowicz, H. Swift, and T. L. Steck, "Maturation of the reticulocyte in vitro," *J Cell Sci*, vol. 71, pp. 177–97, 1984. [Online]. Available: http://www.ncbi.nlm.nih.gov/pubmed/6097593

[72] P. Wiczling and W. Krzyzanski, "Flow cytometric assessment of homeostatic aging of reticulocytes in rats," *Exp Hematol*, vol. 36, no. 2, pp.

119–27, 2008. [Online]. Available: http://www.ncbi.nlm.nih.gov/pubmed/18206724

[73] P. Garnham, *Malaria Parasites and other Haemosporidia*. London, U.K.: Blackwell Scientific Publishers, 1966.

[74] F. Cox, *Major animal models in malaria research: rodents*, ser. Malaria: Principles and Practice of Malariology. Churchill Livingstone, New York, 1988, vol. 2.

[75] J. C. De Roode, "Within-host competition and the evolution of malaria parasites," Thesis, University of Edinburgh, 2004.

[76] H. B. Reilly, H. Wang, J. A. Steuter, A. M. Marx, and M. T. Ferdig, "Quantitative dissection of clone-specific growth rates in cultured malaria parasites," *Int J Parasitol*, vol. 37, no. 14, pp. 1599–607, 2007. [Online]. Available: http://www.ncbi.nlm.nih.gov/pubmed/17585919

[77] J. L. Villeval, A. Lew, and D. Metcalf, "Changes in hemopoietic and regulator levels in mice during fatal or nonfatal malarial infections. i. erythropoietic populations," *Exp Parasitol*, vol. 71, no. 4, pp. 364–374, 1990. [Online]. Available: http://www.sciencedirect.com/science/article/pii/001448949090062H

[78] A. C. Sexton, R. T. Good, D. S. Hansen, M. C. D'Ombrain, L. Buckingham, K. Simpson, and L. Schofield, "Transcriptional profiling reveals suppressed erythropoiesis, up-regulated glycolysis, and interferon-associated responses in murine malaria," *J Infect Dis*, vol. 189, no. 7, pp. 1245–56, 2004.

[79] N. Thawani, M. Tam, M. J. Bellemare, D. S. Bohle, M. Olivier, J. B. de Souza, and M. M. Stevenson, "Plasmodium products contribute to severe malarial anemia by inhibiting erythropoietin-induced proliferation of erythroid precursors," *J Infect Dis*, vol. 209, no. 1, pp. 140–9, 2014. [Online]. Available: http://www.ncbi.nlm.nih.gov/pubmed/23922378

[80] D. S. Khoury, D. Cromer, J. Akter, I. Sebina, T. Elliott, B. S. Thomas, M. S. Soon, K. R. James, S. E. Best, A. Haque *et al.*, "Host-mediated impairment of parasite maturation during blood-stage plasmodium infection," *Proceedings of the National Academy of Sciences*, vol. 114, no. 29, pp. 7701–7706, 2017.

[81] N. Mideo, V. C. Barclay, B. H. Chan, N. J. Savill, A. F. Read, and T. Day, "Understanding and predicting strain-specific patterns of pathogenesis in the rodent malaria plasmodium chabaudi," *Am Nat*, vol. 172, no. 5, pp. 214–38, 2008. [Online]. Available: http://www.journals.uchicago.edu/doi/abs/10.1086/591684

[82] Y. Li, S. Ruan, and D. Xiao, "The within-host dynamics of malaria infection with immune response," *Math Biosci Eng*, vol. 8, no. 4, pp. 999–1018, 2011.

[83] D. Cromer, K. J. Evans, L. Schofield, and M. P. Davenport, "Preferential invasion of reticulocytes during late-stage plasmodium berghei infection accounts for reduced circulating reticulocyte levels," *Int J Parasitol*, vol. 36, no. 13, pp. 1389–97, 2006. [Online]. Available: http://www.ncbi.nlm.nih.gov/pubmed/16979643

[84] L. L. Fonseca and E. O. Voit, "Comparison of mathematical frameworks for modeling erythropoiesis in the context of malaria infection," *Mathematical biosciences*, vol. 270, pp. 224–236, 2015.

[85] A. Raue, C. Kreutz, T. Maiwald, J. Bachmann, M. Schilling, U. Klingmuller, and J. Timmer, "Structural and practical identifiability analysis of partially observed dynamical models by exploiting the profile likelihood," *Bioinformatics*, vol. 25, no. 15, pp. 1923–9, 2009. [Online]. Available: http://www.ncbi.nlm.nih.gov/pubmed/19505944

[86] J. Berger, "Phenylhydrazine haematotoxicity," *J Appl Biomed*, vol. 5, no. 3, pp. 125–30, 2007.

[87] M. J. Nielsen, H. J. Møller, and S. K. Moestrup, "Hemoglobin and heme scavenger receptors," *Antioxidants & redox signaling*, vol. 12, no. 2, pp. 261–273, 2010.

[88] R. Moreau, D. T. Malu, M. Dumais, E. Dalko, V. Gaudreault, H. Roméro, C. Martineau, O. Kevorkova, J. S. Dardon, E. L. Dodd *et al.*, "Alterations in bone and erythropoiesis in hemolytic anemia: comparative study in bled, phenylhydrazine-treated and plasmodium-infected mice," *PLoS One*, vol. 7, no. 9, p. e46101, 2012.

[89] K. Brown and L. Hills, "Recent developments in vaccination against malaria: The possible role of isoantigens in protective immunity to malaria," *Bulletin of the World Health Organization*, vol. 57, no. Suppl, p. 135, 1979.

[90] J. L. Spivak, D. Toretti, and H. W. Dickerman, "Effect of phenylhydrazine-induced hemolytic anemia on nuclear rna polymerase activity of the mouse spleen," *Blood*, vol. 42, no. 2, pp. 257–266, 1973.

[91] C. H. Kim, "Homeostatic and pathogenic extramedullary hematopoiesis," *Journal of blood medicine*, vol. 1, p. 13, 2010.

[92] P. H. Long, "Experimental anemia produced by phenyl-hydrazine derivatives," *The Journal of clinical investigation*, vol. 2, no. 4, pp. 329–342, 1926.

[93] N. J. Savill, W. Chadwick, and S. E. Reece, "Quantitative analysis of mechanisms that govern red blood cell age structure and dynamics during anaemia," *PLoS computational biology*, vol. 5, no. 6, p. e1000416, 2009.

[94] S. K. Jain and P. Hochstein, "Membrane alterations in phenylhydrazine-induced reticulocytes," *Archives of biochemistry and biophysics*, vol. 201, no. 2, pp. 683–687, 1980.

[95] J. Dreschfeld, "Pyrodin: a new antipyretic," *Br Med J ii*, vol. 881, 1888.

[96] C. S. Hopp, B. L. Bennett, S. Mishra, C. Lehmann, K. K. Hanson, J. W. Lin, K. Rousseau, F. A. Carvalho, W. A. van der Linden, N. C. Santos, M. Bogyo, S. M. Khan, V. Heussler, and P. Sinnis, "Deletion of the rodent malaria ortholog for falcipain-1 highlights differences between hepatic and

blood stage merozoites," *PLoS Pathog*, vol. 13, no. 9, p. e1006586, 2017. [Online]. Available: http://www.ncbi.nlm.nih.gov/pubmed/28922424

[97] A. Srivastava, D. J. Creek, K. J. Evans, D. De Souza, L. Schofield, S. Muller, M. P. Barrett, M. J. McConville, and A. P. Waters, "Host reticulocytes provide metabolic reservoirs that can be exploited by malaria parasites," *PLoS Pathog*, vol. 11, no. 6, p. e1004882, 2015. [Online]. Available: http://www.ncbi.nlm.nih.gov/pubmed/26042734

[98] R. Banerjee, S. Khandelwal, Y. Kozakai, B. Sahu, and S. Kumar, "Cd47 regulates the phagocytic clearance and replication of the plasmodium yoelii malaria parasite," *Proc Natl Acad Sci U S A*, vol. 112, no. 10, pp. 3062–7, 2015. [Online]. Available: http://www.ncbi.nlm.nih.gov/pubmed/25713361

[99] J. Iyer, A. C. Gruner, L. Renia, G. Snounou, and P. R. Preiser, "Invasion of host cells by malaria parasites: a tale of two protein families," *Mol Microbiol*, vol. 65, no. 2, pp. 231–49, 2007. [Online]. Available: http://www.ncbi.nlm.nih.gov/pubmed/17630968

[100] M. Lopes da Silva, C. Thieleke-Matos, L. Cabrita-Santos, J. S. Ramalho, S. T. Wavre-Shapton, C. E. Futter, D. C. Barral, and M. C. Seabra, "The host endocytic pathway is essential for plasmodium berghei late liver stage development," *Traffic*, vol. 13, no. 10, pp. 1351–1363, 2012.

[101] A. Sturm, R. Amino, C. Van de Sand, T. Regen, S. Retzlaff, A. Rennenberg, A. Krueger, J.-M. Pollok, R. Menard, and V. T. Heussler, "Manipulation of host hepatocytes by the malaria parasite for delivery into liver sinusoids," *science*, vol. 313, no. 5791, pp. 1287–1290, 2006.

[102] M. Prudêncio, A. Rodriguez, and M. M. Mota, "The silent path to thousands of merozoites: the plasmodium liver stage," *Nature Reviews Microbiology*, vol. 4, no. 11, p. 849, 2006.

[103] A. M. Vaughan and S. H. Kappe, "Malaria vaccine development: persistent challenges," *Current Opinion in Immunology*, vol. 24, no. 3,

pp. 324 – 331, 2012, lymphocyte activation and effector functions / Vaccines. [Online]. Available: http://www.sciencedirect.com/science/article/pii/S0952791512000556

[104] J. L. Miller, S. Murray, A. M. Vaughan, A. Harupa, B. Sack, M. Baldwin, I. N. Crispe, and S. H. I. Kappe, "Quantitative bioluminescent imaging of pre-erythrocytic malaria parasite infection using luciferase-expressing plasmodium yoelii," *PLOS ONE*, vol. 8, no. 4, pp. 1–9, 04 2013. [Online]. Available: https://doi.org/10.1371/journal.pone.0060820

[105] R. J. Longley, A. V. Hill, and A. J. Spencer, "Malaria vaccines: identifying plasmodium falciparum liver-stage targets," *Frontiers in microbiology*, vol. 6, p. 965, 2015.

[106] B. Wizel, R. A. Houghten, K. C. Parker, J. E. Coligan, P. Church, D. M. Gordon, W. R. Ballou, and S. L. Hoffman, "Irradiated sporozoite vaccine induces hla-b8-restricted cytotoxic t lymphocyte responses against two overlapping epitopes of the plasmodium falciparum sporozoite surface protein 2." *Journal of Experimental Medicine*, vol. 182, no. 5, pp. 1435–1445, 1995.

[107] M. Tsuji, "A retrospective evaluation of the role of t cells in the development of malaria vaccine," *Experimental parasitology*, vol. 126, no. 3, pp. 421–425, 2010.

[108] J. Ezaki, N. Matsumoto, M. Takeda-Ezaki, M. Komatsu, K. Takahashi, Y. Hiraoka, H. Taka, T. Fujimura, K. Takehana, M. Yoshida *et al.*, "Liver autophagy contributes to the maintenance of blood glucose and amino acid levels," *Autophagy*, vol. 7, no. 7, pp. 727–736, 2011.

[109] C. Agop-Nersesian, M. De Niz, L. Niklaus, M. Prado, N. Eickel, and V. T. Heussler, "Shedding of host autophagic proteins from the parasitophorous vacuolar membrane of plasmodium berghei," *Scientific Reports*, vol. 7, no. 1, p. 2191, 2017.

[110] M. Hösel, A. Huber, S. Bohlen, J. Lucifora, G. Ronzitti, F. Puzzo, F. Bois-gerault, U. T. Hacker, W. J. Kwanten, N. Klöting *et al.*, "Autophagy determines efficiency of liver-directed gene therapy with adeno-associated viral vectors," *Hepatology*, vol. 66, no. 1, pp. 252–265, 2017.

[111] G. Zaffagnini and S. Martens, "Mechanisms of selective autophagy," *Journal of Molecular Biology*, vol. 428, no. 9, Part A, pp. 1714 – 1724, 2016, molecular Mechanisms of Autophagy, Part A. [Online]. Available: http://www.sciencedirect.com/science/article/pii/S0022283616001091

[112] A. Kuma, M. Hatano, M. Matsui, A. Yamamoto, H. Nakaya, T. Yoshimori, Y. Ohsumi, T. Tokuhisa, and N. Mizushima, "The role of autophagy during the early neonatal starvation period," *Nature*, vol. 432, no. 7020, p. 1032, 2004.

[113] A. M. Vaughan, A. S. Aly, and S. H. Kappe, "Malaria parasite pre-erythrocytic stage infection: gliding and hiding," *Cell host & microbe*, vol. 4, no. 3, pp. 209–218, 2008.

[114] C. M. Schworer, K. Shiffer, and G. Mortimore, "Quantitative relationship between autophagy and proteolysis during graded amino acid deprivation in perfused rat liver." *Journal of Biological Chemistry*, vol. 256, no. 14, pp. 7652–7658, 1981.

[115] G. E. Mortimore, N. J. Hutson, and C. A. Surmacz, "Quantitative correlation between proteolysis and macro-and microautophagy in mouse hepatocytes during starvation and refeeding," *Proceedings of the National Academy of Sciences*, vol. 80, no. 8, pp. 2179–2183, 1983.

[116] L. Mancio-Silva, K. Slavic, M. T. G. Ruivo, A. R. Grosso, K. K. Modrzynska, I. M. Vera, J. Sales-Dias, A. R. Gomes, C. R. MacPherson, P. Crozet *et al.*, "Nutrient sensing modulates malaria parasite virulence," *Nature*, vol. 547, no. 7662, p. 213, 2017.

[117] M. Tseng and J. H. Myers, "The relationship between parasite fitness and host condition in an insect - virus system," *PLOS ONE*, vol. 8, no. 4, pp.

1–9, 09 2014. [Online]. Available: https://doi.org/10.1371/journal.pone.
0106401

[118] L. Lim and G. I. McFadden, "The evolution, metabolism and functions of
the apicoplast," *Philosophical Transactions of the Royal Society B: Biological Sciences*, vol. 365, no. 1541, pp. 749–763, 2010.

[119] C. D. Goodman and G. I. McFadden, "Targeting apicoplasts in malaria
parasites," *Expert Opinion on Therapeutic Targets*, vol. 17, no. 2, pp.
167–177, 2013. [Online]. Available: https://doi.org/10.1517/14728222.
2013.739158

[120] G. I. McFadden, "Apicoplast," *Current Biology*, vol. 24, no. 7, pp. R262
– R263, 2014. [Online]. Available: http://www.sciencedirect.com/science/
article/pii/S0960982214000256

[121] T. A. Dellibovi-Ragheb, H. Jhun, C. D. Goodman, M. S. Walters, D. R.
Ragheb, K. A. Matthews, K. Rajaram, S. Mishra, G. I. McFadden, P. Sinnis
et al., "Host biotin is required for liver stage development in malaria parasites," *Proceedings of the National Academy of Sciences*, vol. 115, no. 11,
pp. E2604–E2613, 2018.

[122] Y. Wang, L. M. Weiss, and A. Orlofsky, "Host cell autophagy is induced by
toxoplasma gondii and contributes to parasite growth," *Journal of Biological Chemistry*, vol. 284, no. 3, pp. 1694–1701, 2009.

[123] J. Laliberte and V. B. Carruthers, "Host cell manipulation by the human
pathogen toxoplasma gondii," *Cellular and molecular life sciences*, vol. 65,
no. 12, pp. 1900–1915, 2008.

[124] I. Clark and K. Rockett, "The cytokine theory of human cerebral malaria,"
Parasitology Today, vol. 10, no. 10, pp. 410–412, 1994.

[125] A. Berendt, G. Tumer, and C. Newbold, "Cerebral malaria: the sequestration hypothesis," *Parasitology Today*, vol. 10, no. 10, pp. 412–414, 1994.

[126] W. S. Crocodile, M. C. Alan, T. Terrie, G. G. Emile, M. M. Edward, and C. A. Gordon, "Vascular endothelial cells cultured from patients with cerebral or uncomplicated malaria exhibit differential reactivity to tnf," *Cellular Microbiology*, vol. 13, no. 2, pp. 198–209, 2010.

[127] N. A. Beare, S. P. Harding, T. E. Taylor, S. Lewallen, and M. E. Molyneux, "Perfusion abnormalities in children with cerebral malaria and malarial retinopathy," *The Journal of infectious diseases*, vol. 199, no. 2, pp. 263–271, 2009.

[128] J. Storm and A. G. Craig, "Pathogenesis of cerebral malaria—inflammation and cytoadherence," *Frontiers in Cellular and Infection Microbiology*, vol. 4, p. 100, 2014. [Online]. Available: https://www.frontiersin.org/article/10.3389/fcimb.2014.00100

[129] R. M. Fairhurst, C. D. Bess, and M. A. Krause, "Abnormal pfemp1/knob display on plasmodium falciparum-infected erythrocytes containing hemoglobin variants: fresh insights into malaria pathogenesis and protection," *Microbes and infection*, vol. 14, no. 10, pp. 851–862, 2012.

[130] N. J. White, G. D. Turner, N. P. Day, and A. M. Dondorp, "Lethal malaria: Marchiafava and bignami were right," *The Journal of infectious diseases*, vol. 208, no. 2, pp. 192–198, 2013.

[131] T. W. Yeo, D. A. Lampah, E. Tjitra, K. Piera, R. Gitawati, E. Kenangalem, R. N. Price, and N. M. Anstey, "Greater endothelial activation, weibel-palade body release and host inflammatory response to plasmodium vivax, compared with plasmodium falciparum: a prospective study in papua, indonesia," *The Journal of infectious diseases*, vol. 202, no. 1, pp. 109–112, 2010.

[132] G. E. Grau, T. E. Taylor, M. E. Molyneux, J. J. Wirima, P. Vassalli, M. Hommel, and P.-H. Lambert, "Tumor necrosis factor and disease severity in children with falciparum malaria," *New England journal of medicine*, vol. 320, no. 24, pp. 1586–1591, 1989.

[133] M. A. Hall, "Correlation-based feature selection for machine learning," Ph.D. dissertation, University of Waikato Hamilton, 1999.

[134] A. Villegas-Mendez, R. Greig, T. N. Shaw, J. B. de Souza, E. G. Findlay, J. S. Stumhofer, J. C. Hafalla, D. G. Blount, C. A. Hunter, E. M. Riley *et al.*, "Ifn-γ–producing cd4+ t cells promote experimental cerebral malaria by modulating cd8+ t cell accumulation within the brain," *The Journal of Immunology*, p. 1200688, 2012.

[135] J. Nitcheu, O. Bonduelle, C. Combadiere, M. Tefit, D. Seilhean, D. Mazier, and B. Combadiere, "Perforin-dependent brain-infiltrating cytotoxic cd8+ t lymphocytes mediate experimental cerebral malaria pathogenesis," *The Journal of Immunology*, vol. 170, no. 4, pp. 2221–2228, 2003.

[136] D. M. Yanez, D. D. Manning, A. J. Cooley, W. P. Weidanz, and H. Van Der Heyde, "Participation of lymphocyte subpopulations in the pathogenesis of experimental murine cerebral malaria." *The Journal of Immunology*, vol. 157, no. 4, pp. 1620–1624, 1996.

[137] E. Belnoue, M. Kayibanda, A. M. Vigario, J.-C. Deschemin, N. van Rooijen, M. Viguier, G. Snounou, and L. Rénia, "On the pathogenic role of brain-sequestered $\alpha\beta$ cd8+ t cells in experimental cerebral malaria," *The Journal of Immunology*, vol. 169, no. 11, pp. 6369–6375, 2002.

[138] L. Yu and H. Liu, "Feature selection for high-dimensional data: A fast correlation-based filter solution," in *Proceedings of the 20th international conference on machine learning (ICML-03)*, 2003, pp. 856–863.

[139] L. Piva, P. Tetlak, C. Claser, K. Karjalainen, L. Renia, and C. Ruedl, "Cutting edge: Clec9a+ dendritic cells mediate the development of experimental cerebral malaria," *The Journal of Immunology*, vol. 189, no. 3, pp. 1128–1132, 2012.

[140] G. S. Campanella, A. M. Tager, J. K. El Khoury, S. Y. Thomas, T. A. Abrazinski, L. A. Manice, R. A. Colvin, and A. D. Luster, "Chemokine

receptor cxcr3 and its ligands cxcl9 and cxcl10 are required for the development of murine cerebral malaria," *Proceedings of the National Academy of Sciences*, vol. 105, no. 12, pp. 4814–4819, 2008.

[141] J. Miu, A. J. Mitchell, M. Müller, S. L. Carter, P. M. Manders, J. A. McQuillan, B. M. Saunders, H. J. Ball, B. Lu, I. L. Campbell *et al.*, "Chemokine gene expression during fatal murine cerebral malaria and protection due to cxcr3 deficiency," *The Journal of Immunology*, vol. 180, no. 2, pp. 1217–1230, 2008.

[142] S. W. Howland, C. Claser, C. M. Poh, S. Y. Gun, and L. Rénia, "Pathogenic cd8+ t cells in experimental cerebral malaria," in *Seminars in immunopathology*, vol. 37, no. 3.   Springer, 2015, pp. 221–231.

[143] T. N. Shaw, P. J. Stewart-Hutchinson, P. Strangward, D. B. Dandamudi, J. A. Coles, A. Villegas-Mendez, J. Gallego-Delgado, N. van Rooijen, E. Zindy, A. Rodriguez *et al.*, "Perivascular arrest of cd8+ t cells is a signature of experimental cerebral malaria," *PLoS pathogens*, vol. 11, no. 11, p. e1005210, 2015.

[144] F. G. Baptista, A. Pamplona, A. C. Pena, M. M. Mota, S. Pied, and A. M. Vigário, "Accumulation of plasmodium berghei-infected red blood cells in the brain is crucial for the development of cerebral malaria in mice," *Infection and immunity*, vol. 78, no. 9, pp. 4033–4039, 2010.

[145] K. H. Chang, M. Tam, and M. M. Stevenson, "Modulation of the course and outcome of blood-stage malaria by erythropoietin-induced reticulocytosis," *J Infect Dis*, vol. 189, no. 4, pp. 735–43, 2004. [Online]. Available: http://www.ncbi.nlm.nih.gov/pubmed/14767829